Development and Application of Methods to Measure Temperatures of Flowing Particles in Suspension

Kimberley C.Y. Kueh

Thesis submitted for the degree of Doctor of Philosophy

School of Mechanical Engineering

Faculty of Engineering, Computer & Mathematical Sciences

The University of Adelaide, South Australia

August 2019

Table of Contents

Abstract

This thesis reports on the development and application of a new method for the measurement of particles transported within a moving fluid and subjected to high fluxes of radiant heating. The comprehensive understanding of heat transfer in particle-laden flows is important as it is a key factor in enabling optimisation of various industrial and scientific applications such as combustion, mineral processing plants, and pharmaceutical manufacturing, as well as aid in the development of new technologies based on the two-phase flow. However, one of the major factors that limits the furtherance of understanding of the field is the difficulty in measuring temperatures of moving, micron-sized particles.

Previously, most publications on heat transfer in particle-laden flows focus on gas temperature measurements, where the temperatures of particles are inferred through fundamental heat transfer equations. However, this technique is not applicable in systems where a large disparity exist between the gas and particle temperatures, and does not take into account inter-particle relationships which could have a significant effect on the overall heat transfer where the inter-particle spacing is sufficiently low. In order to distinguish between the particle and gas phase temperatures, a radiative heat source capable of delivering continuous heat fluxes of up to 36.6MW/m^2 in the form of a Solid-State Solar Thermal Simulator (SSSTS) was used throughout this dissertation. This is because the SSSTS operates at a wavelength of 910nm, which is only absorbed by the particle phase and not the gas phase. Importantly, the operation of the SSSTS at this wavelength does not interfere with the excitation signal (355nm) used in the LIP technique. However, the performance of the SSSTS is not well understood due to the system being the first of its kind. Chapter 4 of this dissertation addresses this by characterising in detail the SSSSTS.

The next part of this dissertation describes the development and application of single-shot, non-intrusive particle temperature measurement techniques based on laser-induced phosphorescence (LIP), a thermometry that makes use of the phosphorescent emission properties of thermophosphors (TPs) governed by the temperature-dependent Boltzmann distribution. Here, ZnO:Zn TPs were selected to be used as they have the highest temperature sensitivity below 625°C. The TPs were suspended in unsteady flow in an optically-accessible fluidised bed and subjected to high radiative heat fluxes of up to 21.1 MW/m^2. Two types of thermometry are reported – with Chapter 5 describing the development of an in-situ, area-averaged, temporally-resolved particle temperature measurement technique by analysing the

change in phosphorescent emission spectra of the selected TP with respect to wavelength, collected using a fibre-optic cable connected to a spectrometer; and Chapter 6 detailing a single-shot, planar particle temperature measurement. For the planar thermometry, the phosphorescent emissions of the TPs were collected using a single ICCD camera fitted with an image splitter and two interference filters specifically selected. Each measurement derives from two 15mm × 10.8mm images collected simultaneously to avoid errors associated with time-delays and/or angular distortions. The resultant spatial resolution for each image was 51pixels/mm, with an average of 30 particles recorded within the imaging region. It was demonstrated that the particle temperatures measured with the LIP technique was found to be approximately 44°C higher on average than the gas temperatures measured with a thermocouple in the same system. A strong dependence of heat flux, as well as particle attenuation (mass loading) on particle temperature was also reported. Additionally, a maximum particle temperature rise of 350°C was recorded with a heat flux of 21.1 MW/m^2, where the maximum particle residence time in the heating region is 0.05s.

The next section of this thesis details the study of application of the developed thermometry technique in a laminar particle-laden jet flow issued from a 12.8mm pipe downwards into a wind tunnel and the particles radiatively heated by the SSSTS. The measured data were analysed by comparison with the results from a simple first-order analytical model that considers the radiative heating, convective cooling, radiative heat loss and heat gain of a single particle. It was found that heat flux, particle concentration and to a lesser extent, particle diameter all affect particle temperatures. At low heat fluxes, $\dot{Q}_{rad} \leq 6.1$ MW/m^2, particle concentrations and temperatures were found to be higher in jet edge, consistent with previous investigations. At heat fluxes above that, where $\dot{Q}_{rad} > 6.1$ MW/m^2, thermophoresis was observed, as evidenced by the migration of the smaller particles to the jet edge where the local temperature is lower. The effect of buoyancy was also observed at $\dot{Q}_{rad} \geq 20.6$ MW/m^2, as evidenced by two distinct regions of high particle temperatures upstream from the heating region (one at the jet axis, and one at the jet edge). These results were presented in Chapter 7 of the present dissertation.

Declaration

I certify that this work contains no material which has been accepted for the award of any other degree or diploma in my name, in any university or other tertiary institution and, to the best of my knowledge and belief, contains no material previously published or written by another person, except where due reference has been made in the text. In addition, I certify that no part of this work will, in the future, be used in a submission in my name, for any other degree or diploma in any university or other tertiary institution without the prior approval of the University of Adelaide and where applicable, any partner institution responsible for the joint-award of this degree.

I acknowledge that copyright of published works contained within this thesis resides with the copyright holder(s) of those works.

I also give permission for the digital version of my thesis to be made available on the web, via the University's digital research repository, the Library Search and also through web search engines, unless permission has been granted by the University to restrict access for a period of time.

I acknowledge the support I have received for my research through the provision of an Australian Government Research Training Program Scholarship.

Kimberley C.Y. Kueh
30 / 01 / 2020

Acknowledgements

All work in current dissertation was carried out at the University of Adelaide's School of Mechanical Engineering. Throughout this journey, much help have been received from various parties and to each of them, I am sincerely grateful.

First and foremost, I would like to thank God for His blessings and sustainment, without which none of this is possible.

Next, I would like to express my utmost gratitude to my principal supervisor, Professor Graham "Gus" Nathan, for providing me the opportunity of working on this immensely interesting project – it has been a great learning experience and I am glad to be part of the "two-phase team" he started. His motivation and willingness to share his extensive knowledge in many different fields, from two-phase flows to heat and mass transfers, have been critical in this dissertation. I would also like to thank my co-supervisor, A/Professor Zeyad Alwahabi, for his guidance, both at work and in life. His expertise in laser diagnostics and experimental works were crucial in this dissertation. He is always willing to help, be a sounding board for my ideas and provide advice. Another person I am extremely grateful for in this journey is my other co-supervisor, Dr. Timothy Lau, for helping me with post-processing and validation of my analyses. His thoroughness in cross-checking data gives confidence to the results obtained.

The support I received throughout my candidature from the mechanical workshop at the University of Adelaide cannot be understated. In particular, I would like to thank Jeffrey Hiorns and Jason Peak for the mammoth effort put in to build the experimental setups and safety features required by the scope of this thesis.

I would also like to acknowledge the Australian Research Council (ARC) and Professor Nathan for providing me with financial support through the Australian Postgraduate Award, Discovery grant 150102230 and Linkage Grant LE130100127.

To my friends, lifegroup, and colleagues from S324a – thanks for being there throughout this journey, keeping my spirits up and motivation high. To my family – Vincent, Emily, Eugene, Bibiana, Peanut, and Jin for your love, support and continuous prayers. You believed in me when I did not and for that I am grateful.

Chapter 1:

Introduction

1. Introduction

Particle-laden flows are two-phase fluid flows that typically consist of a solid phase in the form of small particles and a carrier fluid phase. These flows are integral parts of many common processes such as combustion, mineral processing and manufacturing (Aldén et al., 2011, Kohse-Höinghaus et al., 2005), where process efficiencies, particularly heat transfer efficiencies, heavily depend on the interaction between the two phases (Will et al., 2017, Arcen et al., 2012, Biyikli, 2015). However, the heat transfer in these non iso-thermal particle-laden flows remains poorly understood because of its complexity, which arises from the coupled and non-linear mechanisms of particle-fluid interactions, inter-particle collisions, radiation attenuation, particle clustering, and self-generating turbulence due to high disparity in temperature of the two-phases (Frankel et al., 2016, Rahmani et al., 2018, Collier et al., 2004, Liu et al., 2006, Zhengbiao et al., 2014, Pesic et al., 2014, Elghobashi, 1994). As such, proper understanding of particle-laden flow systems is necessary, not only to aid in the improvement of existing process efficiencies, but also to support development of new technologies such as those in concentrated solar thermal (CST) systems (Ordonez et al., 2014, Grena, 2009).

Heat transfer in turbulent particle-laden flows are known to be a complex field of study, where the complexity increases with increasing particle volumetric fraction, ϕ. For very low ϕ ($\leq 10^{-6}$), the flow is known to be in a one-way coupling regime, where particles have negligible effects on the flow (Elghobashi, 2006). As ϕ increases ($10^{-6} \leq \phi \leq 10^{-3}$), the flow approaches the two-way coupling regime, where the particles starts to play an active role in influencing the flow (Elghobashi, 2006). As the volumetric loading continues to increase ($\phi \geq 10^{-3}$), inter-particle and fluid-particle interactions both play important roles in defining the flow field. This interaction is termed as four-way coupling (Elghobashi, 2006). Many practical applications of particle-laden flows operate within the second and third regime. An instance of this is large-scale falling particle receivers in CST systems, where volume loadings are within the $10^{-4} \leq \phi \leq 10^{-1}$ range (Ordonez et al., 2014, Kim et al., 2019). As such, it is important to properly understand these interactions in a heated flow field and conditions in which they occur in this regime.

A complicating phenomenon that occurs in two and four-way coupled particle-laden flows is thermophoresis, a phenomenon where small particles tend to migrate in the direction of lower temperatures (Talbot et al., 1980, Tsai et al., 2004, Montassier et al., 1991, Han and Mungal, 2000). Studies by Tsai et al. (2004) have showed this phenomenon affects particles of 0.4μm

at temperature differences as low as 68°C. Previously, thermophoresis was observed either by measurement of the velocity of a charged particle as it moves from rest under the influence of gravity, thermal, and electrostatic forces, or by measurement of the motion of particles within a narrow channel that generates thermal gradient (Talbot et al., 1980). However, these measurements did not include spatially resolved particle temperature measurements. Therefore, there is a need for direct particle temperature measurement within a particle-laden jet with high temperature gradients.

Another phenomenon that has been observed, but remains poorly-understood, is self-generated turbulence in particle-laden flows when subjected to strong irradiance (Rahmani et al., 2018, Frankel et al., 2016, Zamansky et al., 2014, Coelho, 2007). It was found that under these conditions, the strong thermal gradients between the solid-gas phases generate non-uniformity in the local particle distributions (Zamansky et al., 2014), although this becomes less prominent in polydispersed flows as polydispersed particles more effectively transfer heat to surrounding gas compared to monodispersed particles due different sized particles having different preferential concentration at various regions of the flow (Rahmani et al., 2018). The non-uniformity of the flow is further complicated by buoyancy generated from hot gas at the boundary layer of the heated particles. The direct numerical simulations (DNS) by Frankel et al. (2016) showed that buoyancy is observed in 40μm diameter particles heated with a irradiative heat flux of 2MW/m^2 in a two-way coupling region ($\phi = 10^{-5}$), where the expected temperature of the particle phase compared to the fluid, T_p/T_o was 2.2. Combined, all these complexities have caused heat transfer in non-isothermal particle-laden flows to remain poorly understood. In particular, the effect of radiative heating on the physical mechanisms of such flows have not been experimentally explored.

One of the main challenges in characterising such flows is that accurate, spatially and temporally resolved experimental temperature measurement of unsteady micro-particles in dense volumetric loading is difficult. In the past, the study of heat transfer in particle-laden flows has been limited to computational modelling, performing experimental validations focused on gas temperature measurements and subsequently inferring particle temperatures through fundamental heat transfer equations, or performing measurements with low spatial resolution. However, these techniques do not accurately represent real systems as they do not take into account inter-particle relationships, which could have a significant effect on the overall heat transfer. This is especially true where the inter-particle spacing is sufficiently low. Additionally, experimental studies performed under thermal equilibrium conditions have a

limited scope of application as they cannot be used in systems in which a large disparity in the two phases are expected, such as that in concentrated solar particle receivers. As such, it is necessary to develop reliable and accurate thermometric techniques with high spatial and temporal resolution, capable of allowing the comprehensive study of heat transfer in such complex flows.

To comprehensively analyse the heat and mass transfer processes within a particle-laden flow in the four-way coupling regime, several critical parameters are needed. In particular, detailed measurements of both the particle and gas-phases are required, such that conditions with temperature disparity between the two phases can be investigated. This, in turn, requires a reliable, non-intrusive technique to conduct spatially and temporally resolved measurements of particle temperatures. Laser diagnostic measurement techniques make use of sophisticated instruments to provide continuous, in-situ, high-speed measurements and advanced strategies for quantitative calibration to achieve the aforementioned requirements (Abram et al., 2013, Fond et al., 2012, Kohse-Höinghaus et al., 2005). They are non-intrusive and are able to simultaneously measure multiple fluctuating quantities such as temperature, volume loading, and particle diameters (Fond et al., 2012). Another important criterion for the selection of a suitable temperature measurement technique to provide data in multiple dimensions. One of the most suitable laser diagnostic technique to achieve this is the Laser-induced phosphorescence (LIP) technique. This uses the temperature-dependent properties of special particles known as thermophosphors (TPs), where the phosphorescent emission spectra shifts as the temperature of the particles change (Brübach et al., 2007). Thus far, LIP has only been used to measure surface and gas temperatures, where TPs were either coated onto various materials, or is seeded in preheated jets, where the TPs were assumed to be representative of fluid temperatures. However, LIP is a relatively new temperature measurement technique and there is a lack of detailed knowledge about the accuracy of experimental methods in conditions of relevance to suspended, non-isothermal flows. Therefore, further development is required to refine the current LIP technique such that it can be accurately and reliably used to measure temperatures of particles in these flows.

In addition to an accurate particle temperature measurement technique, systematic study of heat transfer in particle-laden flows requires a well-controlled heat source that is capable of achieving high enough heating rates of the particle relative to the flow for the two phases to have a significant temperature differential. Given the complexity of the flow field, the heat source should also be well-characterised to reduce the number of ambiguous parameters in the study. Previously, investigations involving heat transfer in particle-laden flows have used preheated jet flows, combustion, and radiative heat sources in the form of xenon-arc or deuterium lamps to increase flow temperatures. However, these heat sources either do not align with practical applications where the flow is non-isothermal as in the case of preheated jet, or they have a tendency to have "hot spots" where some parts of the heating region have a higher heat flux than others. Recently, a first-of-its-kind radiative heat source in the form of a Solid-State Solar Thermal Simulator (SSSTS) was developed at the University of Adelaide (Alwahabi et al., 2016). Given its uniqueness, the performance of system was not well-understood and has never been integrated into a research campaign. Hence, it is necessary to systematically and comprehensively characterise the SSSTS before incorporating it into experiments for the current research.

1.1. Research Gaps

Based on the background above, several research gaps were identified:

- Lack of understanding of the characteristics and performance of the newly-developed Solid-State Solar Thermal Simulator (SSSTS) and how well it integrates in a research campaign
- Lack of a spatially and temporally resolved particle temperature measurement technique to be used in a particle laden flow within a turbulent flow
- Lack of detailed knowledge about the accuracy of experimental methods in conditions of relevance to suspended flows heated by radiation.
- Lack of understanding on the effects of irradiation-induced buoyancy on particle temperature, concentration, and distribution in laminar, radiatively-heated particle-laden jets.

1.2. Thesis Aim

The overall objective of this project is to contribute to the understanding of heat transfer in particle-laden flows using well-resolved, in-situ and direct particle temperature measurements. In particular, the aim of this thesis are as follows:

- To characterise and integrate the Solid-State Solar Thermal Simulator (SSSTS), a radiative heat source capable of delivering high heat flux reliably, into experimental systems to ensure high controllability of the heating process
- To develop a temporally and spatially resolved particle-temperature measurement technique based on the laser-induced phosphorescence (LIP) technique
- To advance understanding of the effect of irradiation-induced buoyancy on heat and mass transfer of particles in a laminar particle-laden jets
    - To advance understanding of the effect of radiative heating on particle temperature, concentration, and distribution in laminar, radiatively-heated particle-laden jets

1.3. Thesis Outline

This hybrid thesis consists of five regular chapters (Chapters 1 – 4 and 8), and 3 journal papers (Chapters 5 – 7), either published or submitted for publication. Among the journal papers, Chapters 5 and 6 focuses on the development of a non-intrusive, temporally and spatially resolved particle temperature measurement technique, while Chapter 7 presents the application of the thermometry on a radiatively heated, laminar particle-laden jet flow. The outline of the thesis is as follows:

Chapter 2: Literature Review

This chapter provides background information of the techniques used previously for particle temperature measurement techniques and work done thus far in the field of heat transfer in particle-laden flows.

Chapter 3 – Experimental Methods

This chapter presents the experimental arrangements used in this research, including detailed descriptions of the equipment and optical arrangements. Also presented in this chapter are the experimental and calibration methodologies, as well as post-processing procedures. Additionally, the characterisation results of ZnO:Zn thermophosphor particles used throughout this dissertation is presented here.

Chapter 4 – Characterising Solid-State Solar Thermal Simulator

This chapter summarises the work done on characterising the performance of the Solid-State Solar Thermal Simulator (SSSTS) performance, including the operational wavelength, electro-optical efficiency, and heat flux capabilities. The beam profile and diameter of the SSSTS is also presented.

Chapter 5 – Non-intrusive temperature measurement of particles in a fluidised bed heated by well-characterised radiation

This chapter consists of the first published paper, which report on the demonstration of a volume-averaged, non-intrusive particle temperature technique based on the laser-induced phosphorescent (LIP) technique. The thermometry method was used to measure temperature of moving particles in an optically-accessible fluidised bed subjected to high-flux irradiation, achieving heating rates in the order of 23,000°C/s. The influence of irradiation flux and particle mass loading on particle temperatures were also evaluated.

Chapter 6 – Single-shot planar temperature imaging of radiatively-heated fluidized particles

This chapter consists of the second published paper, which presents the demonstration of a single-shot, planar particle temperature measurement technique with a spatial resolution of 51mm/pixel. This technique was applied to particles with diameters between 10μm and 50μm suspended in a highly unsteady flow within a fluidized bed and subjected to heat fluxes, $\dot{Q}_{rad}$, up to 21.1MW/m^2.

Chapter 7 – Influences of Buoyancy in a Particle-laden Jet under the Presence of Strong Irradiation

This chapter consists of the third paper submitted for publication, which presents the investigation of heat transfer in a particle-laden jet under high irradiative conditions. The results presented in this chapter show preferential particle concentration at the jet edge at low heat flux cases ($\dot{Q}_{rad} \leq 6.1$ MW/m^2) but as $\dot{Q}_{rad}$ is increased, the particle number density at the jet edge is seen to decrease while simultaneously increasing at the jet centre. This trend is consistent with the influence of thermophoresis. In addition, the distribution of particles was found to have a direct impact on particle aggregate temperatures, such that regions of high particle number density correlated with regions of high particle temperature, which suggests inter-particle re-radiation is significant. A complex phenomenon that cause hot particles to be found upstream of the heated zone at high fluxes ($\dot{Q}_{rad} \geq 12.2$ MW/m^2), particularly in two distinct regions – one towards the jet axis and the other toward the jet edge. This observation suggests that buoyancy, along with thermophoresis, have significant influence under these conditions, especially at regions of high particle temperatures with high particle concentration.

Chapter 8 – Conclusion and Recommendation of Future Work

This chapter presents the conclusions of the work presented in this thesis, as well as recommendations for future work.

1.4. Publications resulting from present work

This thesis produced four journal papers and four peer-reviewed conference paper, as follows:

List of Journal papers:

- Alwahabi, Z.T., Kueh, K.C.Y., Nathan, G.J., Cannon, S., 2016, *Novel solid-state solar thermal simulator supplying 30,000 suns by a fibre optical probe*, Optics Express 24, A1444-A1453.
- Kueh, K.C.Y., Lau, T.C.W., Nathan, G.J., Alwahabi, Z.T., 2017, *Single-shot planar temperature imaging of radiatively heated fluidized particles*, Optics Express 25, 28764-28775.
- Kueh, K.C.Y., Lau, T.C.W., Nathan, G.J., Alwahabi, Z.T., 2018, *Non-intrusive temperature measurement of particles in a fluidised bed heated by well-characterised radiation*, International Journal of Multiphase Flow 100, 186-195.
- Kueh, K.C.Y., Lau, T.C.W., Alwahabi, Z.T., Nathan, G.J., 2019, *Influences of Buoyancy in a Particle-laden Jet under the Presence of Strong Irradiation*, submitted to International Journal of Heat and Fluid Flow.

List of Conference papers:

- Kueh, K.C.Y., Lau, T.C.W., Nathan, G.J., Alwahabi, Z.T., 2015, *Temperature Measurements by Laser-induced Phosphorescence: Effect of Laser Flux Variation*, 7th Australian Conference on Laser Diagnostics in Fluid Mechanics and Combustion.
- Kueh, K.C.Y., Lau, T.C.W., Nathan, G.J., Alwahabi, Z.T., 2017, *Particle Temperature Measurements in a Flow Using Laser-Induced Phosphorescence*, 3rd World Congress on Mechanical, Chemical, and Material Engineering (MCM'17).
- Kueh, K.C.Y., Lau, T.C.W., Nathan, G.J., Alwahabi, Z.T., 2017, *In-situ, well-resolved planar temperature measurement of radiatively-heated particles*, Asia-Pacific Solar Research Concference 2017.
- Kueh, K.C.Y., Lau, T.C.W., Nathan, G.J., Alwahabi, Z.T., 2017, *Heat Transfer within Particle-laden Laminar Jet Flows*, 21st Australasian Fluid Mechanics Conference.

Chapter 2:

Literature Review

2. Literature Review

2.1. Particle-laden Flows

Turbulent particle-laden jets have been the subject of interest of many studies over the years. Aside from their fundamental scientific significance, proper understanding of these flows would also benefit many industries due to their practical applications in chemical, pharmaceutical, combustion, and more (Kohse-Höinghaus et al., 2005, Steinfeld and Palumbo, 2001, Aldén et al., 2011). However, such flows are complex, where parameters such as volume loading, Stokes number and Reynolds number all influence the form of the flows, preferential particle concentration, and more (Fan et al., 1996, Elghobashi, 2006, Balachandar and Eaton, 2010, Monchaux et al., 2012, Lau and Nathan, 2014, Lau and Nathan, 2017). Therefore, an understanding of particle-laden flows is crucial to optimising the aforementioned processes, as well as aid in the development of new applications.

The effect of particle volume loading, ϕ, on turbulent particle-laden flows can be classified as three regimes, as seen in Figure 2-1 (Elghobashi, 2006, Elghobashi, 1994). The first is the one-way coupling regime, where $\phi \leq 10^{-6}$. Here, the particle phase is influenced by the fluid phase, while having negligible effects on the flow. The second regime is the two-way coupling regime, where $10^{-6} \leq \phi \leq 10^{-3}$. In this regime, the particles actively influence the fluid flow and can be further separated into two zones (A and B) based on the ratio between particle response time and the Kolmogorov time scale, τ_p / τ_k. From direct numerical simulations (DNS) by Ferrante and Elghobashi (2003), the effects of particles on turbulence is highly dependent on the τ_p / τ_k ratio in Zone A, where microparticles ($\tau_p / \tau_k \leq 0.1$) were found to cause both the turbulent kinetic energy (TKE) and its dissipation rate to be larger than single-phase flows. Conversely, large particles ($\tau_p / \tau_k > 1$) were reported to reduce both TKE and dissipation rate relative to their single-phase counterparts. In zone B, as the particle size is increased (thereby, increasing τ_p), the particle Reynolds number increases, and at particle Reynolds number, $Re_p \geq 400$, vortex shedding occurs, resulting in enhanced production of turbulence energy. The third regime is the four-way coupling regime ($\phi \geq 10^{-3}$), where interparticle and fluid-particle interactions both influence the flow field (Elghobashi, 2006). Given than many practical applications of particle-laden flows operate within the second and third regime, it is important to properly understand the interactions of the two phases and the conditions in which they occur in these regimes, particularly in flows with high temperature gradients.

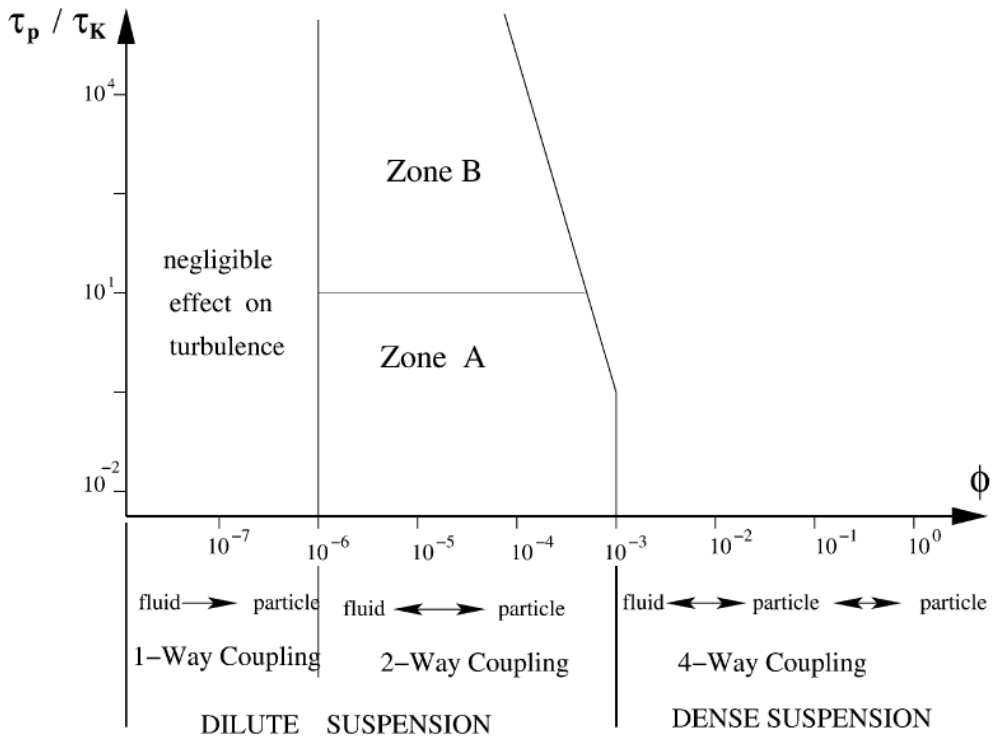

Figure 2-1: Classification of particle-laden turbulent flows based on particle volume loading, ϕ, and the particle response time over the Kolmogorov time scale, τ_{p} / τ_{k}.
Source: Elghobashi (2006).

2.2. Heat Transfer in Particle-laden Flows

In recent years, interest in the development of new and reliable renewable technologies, such as particle receivers for concentrated solar thermal (CST) power systems have grown due to their potential for large-scale power generation, low cost energy storage, and hybridisation (Denholm et al., 2013, Gil et al., 2010, Kuravi et al., 2013, Ho and Iverson, 2014). Ideally, the design target is to optimally maximise radiation capture, while at the same time, minimise re-radiation (Steinfeld and Schubnell, 1993, Ordonez et al., 2014, Steinfeld and Palumbo, 2001) and convective losses, essentially providing effective heat transfer within the site (Z'Graggen *et al.*, 2006), although it is rarely fully achieved. However, optimisation of such system efficiencies often requires large-scale trials, which can be costly, or reliable numerical models informed by detailed and systematic data that are spatially and temporally-resolved, which is difficult to achieve due to non-linear heat and mass transfer mechanisms in such complex flow. Although operational costs of all renewable energy have decreased over the years due to increased penetration into the energy market (IRENA, 2018), it is desirable to further lower the risk of dependence on market penetration and cost of upscaling. CST power systems is still

significantly more expensive than fossil fuel energy systems. To aid in the development and upscaling of such technologies, as well as improve existing process efficiencies of applications operating on the same principals, investigations of this thesis focuses on particle-laden flows subjected to high radiative heat fluxes.

A simplified design of solar receivers consisting of small particles being suspended in a jet flow of a particle receiver and heated by solar radiation reflected upon them through an aperture by the heliostat field is considered in this dissertation as a convenient way to investigate heat transfer in well-characterised environments. Within such simplified system, the expected heat transfer modes occurring within such configurations are: (1) radiative heating by solar radiation on particles, $Q_{rad,heat}$, (2) convective cooling between the particles and surrounding fluids, Q_{conv}, (3) radiative cooling between particles, $Q_{rad,cool}$, and (4) particle sensible temperature increase, Q_{gain}. These heat transfer modes may be combined to lead to the following energy balance equation:

$$Q_{rad,heat} = Q_{conv} + Q_{rad,cool} + Q_{gain} \tag{2-1}$$

where each of these process can be expressed by the following equations:

Radiative heating:

$$Q_{rad,heat} = \alpha \dot{Q}_{rad} A_p \tag{2-2}$$

Convective cooling:

$$Q_{conv} = hA_{p,s}(T_p - T_a) \tag{2-3}$$

Radiative cooling (interparticle re-radiation):

$$Q_{rad,cool} = \varepsilon \sigma A_{p,s}(T_p^4 - T_a^4) \tag{2-4}$$

Heat absorption:

$$Q_{gain} = \dot{m} c_p \frac{dT_p}{dt} \tag{2-5}$$

Here, $\alpha = 0.15$ is the absorptivity (Schunk, 2008), $\dot{Q}_{rad}$ is the laser flux, $A_p = \pi r_p^2$ is the particle cross-sectional area, r_p is the particle radius, $\varepsilon = 0.69$ is the particle emissivity, $\sigma = 5.67 \times 10^{-8}$ W/m^{2}K^4 is the Stefan-Boltzmann constant, $A_{p,s}$ is the particle surface area, $h =$

$\frac{Nu \times d_p}{k_g(T_{film})}$ is the convective heat transfer coefficient, $Nu = 2 + \left(0.4 \times Re^{0.5} + 0.06 \times Re^{\frac{2}{3}}\right) \times Pr^{0.4} \left(\frac{\mu_a}{\mu(T_{film})}\right)^{0.4}$ is the Nusselt number, $Re = \frac{\rho(T_{film}) u_{slip} d_p}{\mu(T_{film})}$ is the Reynolds number, u_{slip} is the slip velocity, k_p is the thermal conductivity of the particle, k_g is the thermal conductivity of the gas, $\dot{m}$ is the mass flow rate, $c_p = (53.999 + 7.851 \times 10^{-4} T_p - 5.868 \times 10^{-5} T_p^{-2} - 127.5\, T_p^{-0.5} + 1.9376 \times 10^{-6}\, T_p^2)$ / 0.08183 J/gK is the calculated particle specific heat capacity (Madelung et al., 1999), T_{film} is the film temperature, T_p is the particle temperature and T_a is the atmospheric temperature. The subscript *a* refers to atmospheric gas parameters. Although highly simplified, Equation 2-1 was used throughout this thesis as a first pass to estimate particle temperature, T_p, under conditions similar to that of the experimental arrangement.

Heat transfer mechanisms involving single, stationary and spherical particles has been extensively analysed for a range of particle diameters, from 2μm to 0.8mm (Fincke *et al.*, 1988, Foss and James Davis, 1996, Grena, 2009, Spjut *et al.*, 1985, Tripathi *et al.*, 2002). These measurements have shown that particle temperature is strongly dependent on incident heat flux and particle sizes. It was found quantitatively that larger particles require a higher energy flux in order to reach equilibrium temperature, though it takes a shorter period of time for them to reach a certain temperature (Tripathi *et al.*, 2002, Fincke *et al.*, 1988, Spjut *et al.*, 1985). This is in line with a study by Monazam and Maloney (1992) who showed particle temperature is heavily dependent on the heat flux, particle absorptivity, particle diameter, and ambient gas thermal conductivity. However, the significance of these parameters on particle temperatures have not been investigated in moving flows.

There are three main forms of heat transfer within a particle-laden flow in a two-way coupling regime – gas-particle heat convection, heat conduction between particles, and inter-particle re-radiation (Mokhtarifar *et al.*, 2015, Grena, 2009). The significance of the first mode becomes more prominent with decreasing particle size and increasing volumetric loading (Fan *et al.*, 1996, Anoop *et al.*, 2009). The second mode occurs when moving particles collide and heat is conducted through the contact points. This form of heat transfer is important to densely loaded systems such as fluidised beds and nanofluids, and is typically the dominating mechanism for particles with high conductivity when there is contact (Kosinski *et al.*, 2014). The last mode is the least-understood, although its role is significant in high temperature conditions, such as those in combustion and concentrated solar thermal particle receiver systems. This is largely

due to difficulty in accurately measuring temperature of moving particles in-situ. As such, there is a need for the development of an accurate, spatially and temporally resolved thermometry technique.

One of the non-linear phenomenon that has been theorised to occur in two-way coupled particle-laden flows is a self-sustained turbulence, specifically under strong irradiance (Zamansky *et al.*, 2012, Zamansky *et al.*, 2014, Rahmani *et al.*, 2018). It was found that under this condition, buoyancy-driven vortices are formed, causing preferential particle concentrations and clustering in the flow (Zamansky et al., 2012, Banko et al., 2019). The temperature gradient across space and time subsequently causes turbulent velocity fluctuations (Zamansky *et al.*, 2012). The direct numerical simulations (DNS) by Frankel *et al.* (2016) found that even when subjected to irradiation, the volume of hot gas at the boundary layer of the particle expands, causing an upward force. Figure 2-2 shows a schematic diagram of the proposed buoyancy effects on (a) individual and (b) clustered particles. It was found that at low irradiation, this buoyant force can reduce settling velocity of particles, reducing the turbulent kinetic energy, TKE, of the flow. Conversely, buoyancy becomes dominant and starts to contribute to TKE at high irradiation. This phenomenon is more pronounced in larger particles due to more buoyant fluid around it as compared to smaller particles. Statistical analysis of the results also showed a correlation between particle concentration and gas temperature (Frankel *et al.*, 2016). However, no direct experimental observations of the role of buoyancy in strongly irradiated flows is available. Hence, new experimental measurements are needed of these phenomena in a radiatively heated particle laden flows under high heating rates.

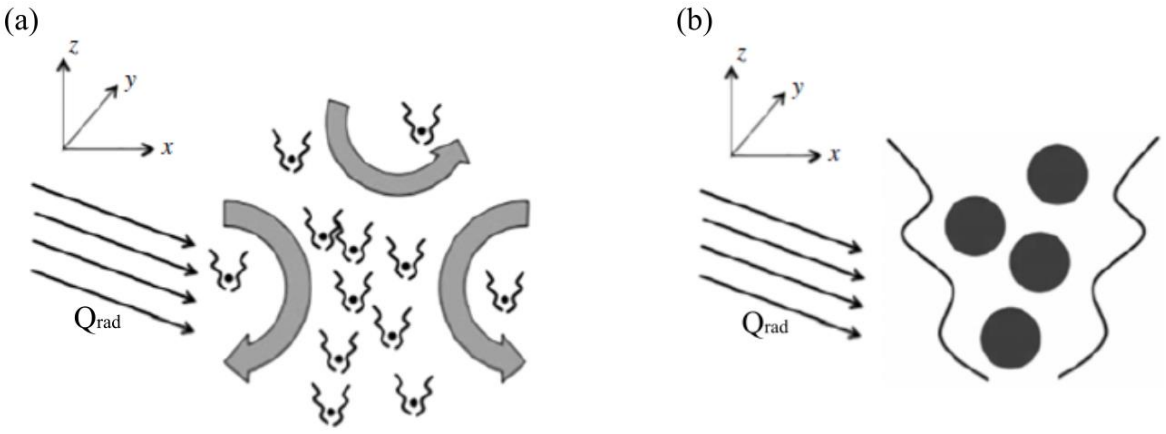

Figure 2-2: Schematic diagram of (1) individual and (b) clustered particles shedding buoyant plumes and generating an upward force, reducing overall descent under the influence of external irradiance. Adapted from: Frankel et al. (2016).

Another phenomenon that has been known to occur in particle-laden flows is thermophoresis, which causes small particles to migrate towards regions of lower temperatures (Han and Mungal, 2000, He and Ahmadi, 1998, Montassier et al., 1991, Talbot et al., 1980, Zheng, 2002). In a flow with thermal gradient, thermophoresis is represented by particles drift velocity, v_T, of $v_T = -D_T \nabla T$, where D_T is the thermophoretic coefficient and ∇T is the temperature gradient (Duhr and Braun, 2006, Braibanti et al., 2008). As such, this phenomenon is typically observed either by measurements of v_T of a charged particle as it moves from rest under the influence of gravity, thermal, and electrostatic forces, or the observation of particle motion are observed within a narrow channel that generates thermal gradient (Talbot *et al.*, 1980). Studies by Tsai *et al.* (2004) showed that thermophoresis can be observed at temperature gradients as low as 68°C for particles of 0.4μm diameters. Typically, these measurements were performed in liquid conditions (Braibanti et al., 2008, Duhr and Braun, 2006), and in gas-particle flows, measurements were done with particles < 1μm diameter at low heating rates (He and Ahmadi, 1998, Tsai et al., 2004). However, the conditions in which thermophoresis occur for particles larger than 1μm has not been experimentally investigated.

Another naturally-occurring condition in particle-laden flows is particle clustering. This is a term used to describe the preferential concentration of particles into highly localised regions in particle-laden flows and is first observed by Squire and Eaton in 1991 (Squires and Eaton, 1991, Longmire and Eaton, 1992, Fessler et al., 1994, Rouson and Eaton, 2001, Elperin et al., 2002, Goto and Vassilicos, 2006, Goto and Vassilicos, 2008, Gualtieri et al., 2013, Lau and Nathan, 2017). Previously, it was found that the Stokes number plays an important role in determining the extent of particle clustering in turbulent flows, the most significant of which occurs where Stokes number is of the order of unity (Fessler et al., 1994, Rouson and Eaton, 2001, Lau and Nathan, 2016). In situations where particle clustering occurs, there exist highly segregated regions of high and low particle concentration, resulting in varying radiative absorption within these regions (Zamansky *et al.*, 2012). This, in turn, affects the occurrence of buoyancy, thermophoresis, and turbulence in the system. Combined, all these mechanisms have caused heat transfer in non-isothermal radiatively heated particle-laden flows to remain poorly understood.

2.3. Particle Temperature Measurement Techniques

Spatially and temporally resolved particle temperature measurement techniques are important to properly investigate heat and mass transfer in two and four-way coupled turbulent flows. However, one of the main challenges currently impeding advancements in this investigation is that there are limited data in this field, stemming from the difficulty in experimental temperature measurement of polydispersed, moving particles at various volumetric loading. Therefore, many studies adopt a technique in which the particle temperature are either assumed to be the same as the gas temperature (Abram *et al.*, 2013, Fond *et al.*, 2012, Hasegawa *et al.*, 2007, Jovicic *et al.*, 2015), or inferred from fundamental heat transfer equations depicting relationships between gas and particle temperature (Katoshevski *et al.*, 2001, Mograbi *et al.*, 2002, Mokhtarifar *et al.*, 2015, Zhao *et al.*, 1999, Zhao and Bar-Ziv, 2002, Ziskind *et al.*, 2001). In particular, many investigations infer gas and particle temperatures from the following (Katoshevski et al., 2001, Mograbi et al., 2002):

$$\frac{F_d}{F_{d,cold}} = \frac{\mu_g(T_{film})}{\mu_g(T_{cold})} \qquad 2\text{-}6$$

where F_d is the measured drag force of particles in electrodynamic chambers, μ_g is the dynamic viscosity of the gas, and T_{film} is the film temperature given by $T_{film} = (T_p + T_{cold}) / 2$. However, given that the dependence of particle temperature on dynamic viscosity is weak (in the order of 10^{-8} magnitude), the accuracy of such temperature measurement for particles is not high. Additionally, this method does not consider the fluctuations in instantaneous heat transfer, and therefore is not applicable to measurements in turbulent flows. Therefore, there is a need to develop a reliable method of measuring instantaneous particle temperatures within a turbulent environment.

The need for spatially and temporally-resolved particle temperature measurements stems from several reasons. Firstly, to be able to investigate turbulent particle-laden flows, a spatially-resolved thermometry technique is necessary to study heat and mass transfer in different parts of the flow field. Additionally, a temporally-resolved thermometry method is important to enable single-shot measurements, particularly in turbulent flows. Laser diagnostics measurement techniques make use of sophisticated instruments to provide continuous in-situ, and high-speed measurements of with high spatial resolution and advanced strategies for quantitative calibration (Abram *et al.*, 2013, Fond *et al.*, 2012, Kohse-Höinghaus *et al.*, 2005). It is non-intrusive and is able to simultaneously measure multiple fluctuating quantities (Fond

et al., 2012). Another important advantage of laser diagnostic techniques is that planar measurements be possible. This would enable a comprehensive review of the effect of inter-particle relationships, as well as the interaction of the flow with the particles on particle temperatures.

One of the earliest measurements of temperature of single stationary particle heated by radiation was performed by Spjut *et al.* (1985) using pyrometry. This investigation demonstrated transient temperature responses of a particle subjected to pulsed laser heating, where the measured particle temperatures achieved accuracies within 25K for the temperature range of 550K to1000K (Spjut *et al.*, 1985). Many studies have since been done using the same technique (Fletcher, 1989, Monazam *et al.*, 1989, Monazam and Maloney, 1992), though significant changes in emissivity were encountered during the process for some. Studies by Monazam *et al.* (1989) and Fincke *et al.* (1988) presented the various emissivity factors that needed to be taken into account when utilising pyrometry and the significance of emissivity uncertainty. They found that an emissivity uncertainty of 20% may result in ±10% error in the overall temperature measurement. Since particle emissivity is typically wavelength-dependent and difficult to be determined, this temperature measurement technique is not suitable for nonblack particles (Rassat and Davis, 1994, Zhao and Bar-Ziv, 2002, Zhao *et al.*, 1999). This, in addition to the fact that pyrometry cannot be used on microparticle in near-ambient temperatures conditions due to weak IR emissions (Spjut *et al.*, 1985), led Rassat and Davis (1994) to develop a technique that utilises Stokes/Anti-Stokes Raman intensity ratios to determine the temperature of a single particle. This method has since been proven to be very precise (within ±3K accuracy in the range of 100K to 300K) in determining the temperature of a single particle (Lübben *et al.*, 1999). Despite that, a drawback of the technique is that the separation of signals from spurious light from adjacent surfaces and particles difficult (Brubach *et al.*, 2006, Jovicic *et al.*, 2015, Kohse-Höinghaus *et al.*, 2005, Zhao *et al.*, 1999, Zhao and Bar-Ziv, 2002). Zhao and Bar-Ziv (2002) then proposed another thermometry technique based on the relationship between free and forced convection, photophoretic forces, and particle temperature. The main advantage of this technique is that it can be applied to any particle material with relative accuracy. However, it can only be used for systems for which the forces mentioned are well-defined (Zhao and Bar-Ziv, 2002, Zhao *et al.*, 1999).

Laser-based methods combine different optical techniques that allow multiple fluctuating quantities to be measured in-situ (Fond *et al.*, 2012). Among the laser diagnostic techniques most commonly used, the coherent anti-Stokes Raman spectroscopy (CARS) technique enables accurate point-resolved measurements and is able to withstand harsh environments, although it is not able to accurately provide 2D measurements in the presence of particles in the gas flow (Brubach *et al.*, 2006, Kohse-Höinghaus *et al.*, 2005). Rayleigh and Raman scattering techniques are able to provide planar measurements and are useful in two-phase flows but has the same drawbacks as that mentioned earlier. Another laser-based method is laser-induced fluorescence (LIF) thermometry. This utilises hydrocarbon tracers added in the gas flow and is a robust technique to study the relationship between mixture formation and temperature (Jovicic *et al.*, 2015, Kohse-Höinghaus *et al.*, 2005). However, LIF investigations of two-phase flows are challenging, particularly because of the large disparity in fluorescence intensity between the two phases and the effect of halation around the particles (Charogiannis and Beyrau, 2013). In contrast, laser-induced phosphorescence (LIP) is a technique in which the temperature dependent properties of thermophosphors (TPs) to determine the temperature of the particles, which does not have the same issue. As such, the LIP technique was chosen as the basis of the current thesis.

2.4. Laser-induced Phosphorescence (LIP)

Temperature influences both the decay time and the emission spectrum of thermophosphors (TPs) in laser-induced phosphorescence (LIP), offering two distinct methods with which to perform thermometry. The first approach is the lifetime method, where the phosphorescence decay time decreases with increasing temperature (variation of up to two or three orders of magnitude). This technique requires the phosphorescence emission to be recorded consecutively at short time intervals during the decay using a framing camera with multiple detectors. The temporal separation between the detectors can be adjusted to minimise errors, with accuracy up to 2K (Fond et al., 2012). However, this method requires TPs with lifetime varying below the microsecond scale over the temperature range of interest, as well as an advanced camera capable of capturing more than 100,000 frames per excitation pulse in turbulent flow conditions. The second approach is the emission method, which makes use of phosphorescent emissions of TPs governed by the temperature-dependent Boltzmann distribution, where the emission spectra shifts with respect to wavelength. Temperatures of the thermophosphors can then be determined by relative temperature dependency. An example of the phosphorescent emission spectra of BAM:Eu thermophosphor is presented in Figure 2-3. Here, temperature of the BAM:Eu TP ratio is determined by taking the ratio of two emission ranges, one at 400 ± 20 nm (labelled red in Figure 2-3), and another at 456 ± 5 nm (labelled blue in Figure 2-3), chosen to optimise temperature sensitivity and signal-to-noise ratio (Sarner et al., 2008). It was found that the accuracy of the emission method is high, with a standard deviation of 0.01% at 340K and 2.3% at 873K (Sarner et al., 2008, Jovicic et al., 2015), and is straightforward to apply to planar measurements over a wide range of temperature, needing only two detectors and a single exposure (Fond et al., 2012). As such, the emission method of the LIP technique was used in this thesis campaign to be further developed to enable in-situ particle temperature measurements.

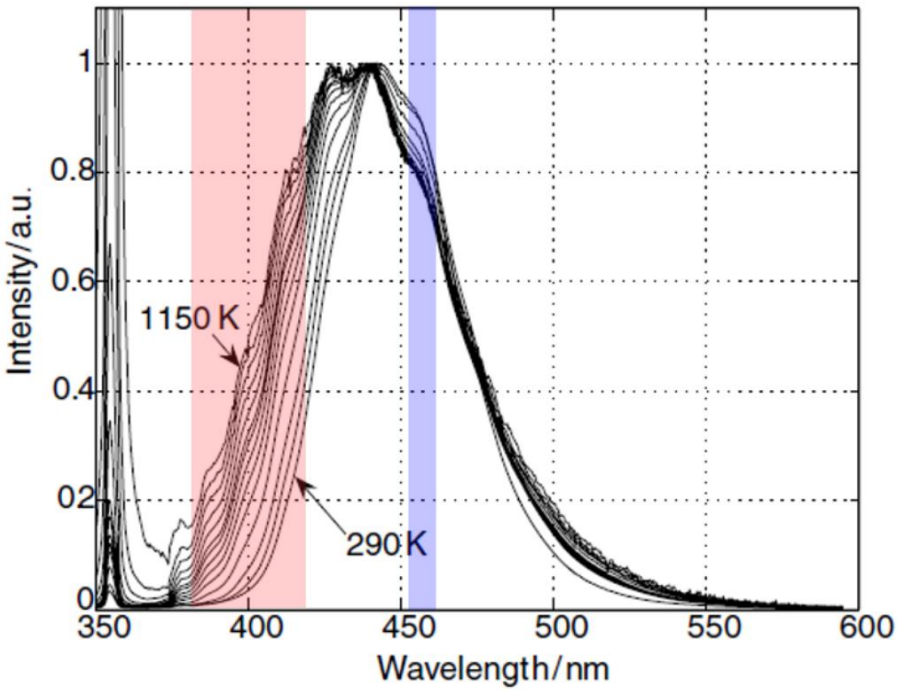

Figure 2-3: Example of temperature-dependent emission spectrum of BAM:Eu thermophosphor. Adapted from: Sarner et al. (2008).

In the past, laser-induced phosphorescence (LIP) has been successfully used to measure gas temperatures through the measurement of particle temperature suspended in the gas flow (Abram *et al.*, 2013, Fond *et al.*, 2012, Jovicic *et al.*, 2015). This approach generally utilises TPs and assumes thermal equilibrium between the gas and solid phases, as in the studies by Hasegawa *et al.* (2007), Abram *et al.* (2013), and Lawrence *et al.* (2013). While the assumption is sound for small particles, the same assumption may not be applicable for larger particles for which convective cooling forces and particle absorptivity play more significant roles (Koizumi *et al.*, 2010, Monazam *et al.*, 1989). Additionally, inter-particle heat transfer should also be taken into account, especially in turbulent conditions where particle clustering is predisposed to occur.

Similar to LIF, LIP first requires an excitation source, such as laser radiation, chemical reactions, or thermal excitation in flames to excite the TPs. Following excitation, the TPs emit phosphorescence due to relaxation of electrons from the excited state to the ground state. Phosphorescence differs from fluorescence as fluorescence occurs from electric dipole-allowed transitions and phosphorescence occurs from forbidden ones (Aldén *et al.*, 2011). As such, phosphorescent materials have a longer lifetime (in the order of microseconds) as compared to fluorescent ones (in the order of nanoseconds), which are closer to the temporal resolution of

ICCD cameras (Charogiannis and Beyrau, 2013) that are to be used in this thesis. This would allow maximum signal collection within the phosphorescence lifetime. Furthermore, a range of thermophosphors exist, each with different temperature sensitivities and response times, allowing the LIP method to be optimised for a particular experimental condition by the selection of an appropriate thermophosphor. Considering that LIP is a relatively simple technique with respect to experimental setup and post processing compared to the aforementioned techniques (Lawrence *et al.*, 2013), it was selected as the appropriate measurement technique for this thesis.

Thermophosphors particles typically consist of ceramic hosts doped with low concentrations of rare-earth ions, which act as luminescent activators. These materials emit radiation following UV excitation, the intensity and spectral response of which are dependent on its temperature. Unlike the previously mentioned LIF hydrocarbon tracers, TPs are able to survive high temperatures (Yu *et al.*, 2010), are chemically inert and are insensitive to pressure and local gas composition (Brübach *et al.*, 2007, Feist *et al.*, 2003). There are many different types of TPs, each with its own characteristics and has varying temperature sensitivity ranges. A number of studies have investigated various TPs (Brübach *et al.*, 2013, Feist *et al.*, 2003, Sarner *et al.*, 2008, Seyfried *et al.*, 2005), characterising properties such as decay lifetime, emission intensity, operating temperature, and effect of oxygen quenching. This information has been comprehensively described in the review by Aldén *et al.* (2011), as seen in Figure 2-4.

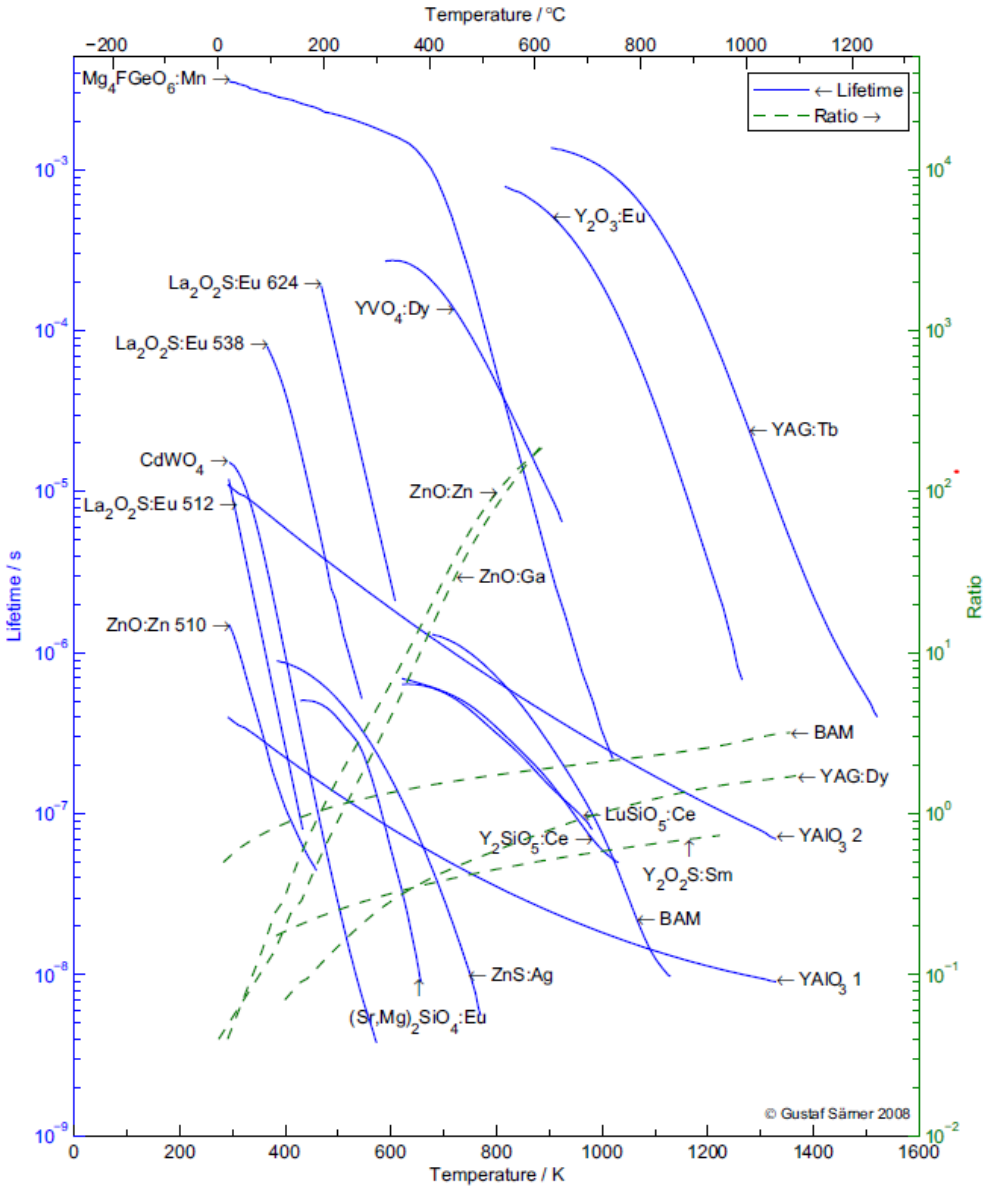

Figure 2-4: Phosphorescent lifetime and ratio dependence on temperature. Source: Aldén et al. (2011).

In selecting the TP to be used in for investigation of particle-laden flows subjected to high irradiation, several factors were taken into consideration. First, the decay lifetime should be long enough for the signal intensity to be distinguishable over the temperature change of the investigation, but short enough (in the microsecond range) to provide high temporal resolution to maximise collection of phosphorescence emission during short exposure times (Fond *et al.*, 2012). Additionally, short phosphorescent emission lifetime allows the possibility of time-gating the signal collection to discriminate interfering background information (Aldén *et al.*, 2011). Second, the TP should have sufficient sensitivity to temperature in the expected temperature range of the measurement object. Thirdly, a large change in emission spectrum

over small temperature range is desirable for precise measurements. And lastly, the TP should emit high signal intensity and be minimally affected by degradation and oxygen quenching (Bizarri and Moine, 2005, Feist *et al.*, 2003, Linden *et al.*, 2009, Sarner *et al.*, 2008). For the purpose of the present research, it is necessary to identify the appropriate TP to be used in turbulent particle-laden flow subjected to radiative heating by a heating laser with high energy flux (small heating area).

Previously, LIP technique have been used in two ways, the first of which is to carry out surface temperature measurements by coating TPs onto the surface using special adhesives known as binder materials, typically liquid that can be easily mixed with the TP powder (Sarner *et al.*, 2008). Alternatively, the LIP technique was employed to measure gas temperatures, where small TP particles, typically in the 1-2μm range, were seeded as tracers in preheated jet flows (Jovicic *et al.*, 2015, Abram *et al.*, 2013, Fond *et al.*, 2012). However, this technique has never been used to measure temperatures of particles large enough to have temperatures different from the gas phase, much less particles in unsteady state.

Table 1 presents a summary of the conditions under which previous heat transfer investigations were performed and their investigation techniques. Here, it can be seen that numerical modelling remain popular, making up over 25% of previous heat transfer studies. Of the previous experimental measurements, only nine were performed with planar temperature measurements (Abram et al., 2013, Fond et al., 2012, Hasegawa et al., 2007, Heyes et al., 2006, Jenkins et al., 2012, Jovicic et al., 2015, Lawrence et al., 2013, Mann et al., 2014, Rabenstein and Leipertz, 1997). Of these, none were performed in conditions where there are temperatures between the particle and gas phases are distinctly different. Therefore, there is a need to more detailed investigations in particle-laden flows where the two phases are not in thermal equilibrium. To do this, not only is a particle thermometry technique that is spatially and temporally resolved needed, a well-controlled heat source that is capable of high heating rates where the particle relative to the flow have a significant temperature differential is important.

Table 1: Summary of literature review of particle-laden flow investigations.

Author	***System***	***Temperature Measurement Technique***	***Particle Size Investigated***	***Volume Loading Classification***	***Spatial Resolution***
Abram *et al.* (2013)	Preheated Jet	PIV; LIP	2μm	unknown	Planar: 0.72mm
Agarwal (1991)	Fluidised bed	Numerical Modelling	22.9mm - 62mm	Assumed 1-way coupling	n/a
Anoop *et al.* (2009)	Nanofluid suspended and heated by hotwire	Thermocouple	45nm; 150nm	4-way coupling	Volume-averaged
Arcen *et al.* (2012)	Turbulent channel flow with imposed hot plate on top and cold plate at bottom	DNS	50-140μm	1-way coupling	n/a
Basu (1990)	Fluidised bed	Numerical Modelling	87-227μm	Assumed 1-way coupling	n/a
Biyikli (2015)	Fluidised bed	Numerical Modelling	465μm; 1400μm	Assumed 4-way coupling	n/a
Bizarri and Moine (2005)	Plate coated with thermophosphor	Photomultiplier tube	n/a	n/a	Area-averaged
Brübach *et al.* (2007)	Plate coated with thermophosphor	Photomultiplier tube	n/a	n/a	Area-averaged
Chen *et al.* (2006)	Particle receiver	CFD	100-900μm	4-way coupling	n/a
Collier *et al.* (2004)	Fluidised bed	Thermocouple	3-10mm	4-way coupling	Volume-averaged
Feist *et al.* (2003)	Furnace coated with thermophosphor	Photomultiplier tube	n/a	n/a	Area-averaged
Fincke *et al.* (1993)	Particle seeded in torch	Pyrometry	5-75μm	n/a	Volume-averaged
Fletcher (1989)	Preheated Jet	Pyrometry	106-149μm	1-way coupling	Volume-averaged
Frankel *et al.* (2016)	Particle-laden flow subjected to irradiation	DNS	40μm	4-way coupling	n/a

Author	*System*	*Temperature Measurement Technique*	*Particle Size Investigated*	*Volume Loading Classification*	*Spatial Resolution*
Fond *et al.* (2012)	Preheated Jet	LIP	2μm	unknown	Planar: 400μm
Grena (2009)	A single particle subjected to irradiation	CFD	0.4-0.8mm	n/a	n/a
Hasegawa *et al.* (2007)	Preheated Jet	LIF	4μm	4-way coupling	Planar: 180μm
Heyes *et al.* (2006)	Plate coated with thermophosphor	LIP, ThC	4μm	n/a	Planar
Jenkins *et al.* (2012)	Thermophosphor in flame	LIF	1.7μm	4-way coupling	Planar: 86μm
Jovicic *et al.* (2015)	Preheated Jet	LIP	2μm	4-way coupling	Planar: 100μm
Katoshevski *et al.* (2001)	Heated single particle suspended in electrodynamic chamber	Emprical formula conversion	65-141.6μm	1-way coupling	n/a
Koizumi *et al.* (2010)	Heated single particle suspended in wind tunnel	Thermocouple	50mm	n/a	n/a
Lawrence *et al.* (2013)	Preheated Jet	LIP	1.8-10.2μm	4-way coupling	Planar: resolution unknown
Lungu *et al.* (2015)	Fluidised bed	CFD	500μm	4-way coupling	n/a
Mann *et al.* (2014)	Impinging jet burner	CARS + LIF	unknown	4-way coupling	Planar: 140x 200μm
Mokhtarifar *et al.* (2015)	Fluidised bed	ThC	253μm	Assumed 1-way coupling	Volume-averaged
Monazam *et al.* (1989)	Heated single particle suspended in electrodynamic chamber	Pyrometry	130μm	1-way coupling	Volume-averaged
Omrane *et al.* (2008)	Preheated Jet	PIV, LIP	1μm	4-way coupling	58μm
Pustovalov (2005)	A single particle subjected to irradiation	Numerical Modelling	14-40μm	n/a	n/a

Author	*System*	*Temperature Measurement Technique*	*Particle Size Investigated*	*Volume Loading Classification*	*Spatial Resolution*
Rabenstein and Leipertz (1997)	Laminar flat-flame burner	Raman	unknown	unknown	Planar: 410μm
Rassat and Davis (1994)	Heated single particle suspended in electrodynamic chamber	Raman	52μm	1-way coupling	Volume-averaged
Sarner *et al.* (2008)	Plate coated with thermophosphor	LIP	4μm	1-way coupling	Volume-averaged
Scott *et al.* (2004)	Fluidised bed	ThC	0.71-9mm	2-way coupling	Volume-averaged
Spjut *et al.* (1985)	Heated single particle suspended in electrodynamic chamber	Pyrometry	10-50μm	1-way coupling	Volume-averaged
Tang *et al.* (2013)	A single particle subjected to irradiation	Raman	1.2μm	n/a	Volume-averaged
Tribelsky *et al.* (2011)	A single particle subjected to irradiation	Numerical Modelling	1nm-10mm	n/a	n/a
Zamansky *et al.* (2014)	Particle-laden flow subjected to irradiation	DNS	unknown	4-way coupling	n/a
Kueh *et al.* (2018)	Fluidised bed	LIP	2-50μm	2-way coupling	20μm
Kueh *et al.* (2017)	Fluidised bed	LIP	2-50μm	2-way coupling	20μm
Kueh *et al.* (2019)	Particle-laden flow subjected to irradiation	LIP	50-350μm	2-way coupling	20μm

2.5. Radiative Heat Source

An important consideration for investigations of particle heat transfer is the availability of a well-defined source of heating. Previous experimental studies on heat transfer of a spherical particle undergoing radiative heating were often performed with sources of heating such as deuterium and xenon lamps (Bizarri and Moine, 2005, Liu et al., 2012). Although these heat sources are cheaply procurable and easy to handle, there are a few drawbacks associated with the equipment. Firstly, the radiant power of such heat source is not well-understood due to non-uniformity in the radiation profile from overlapping radiation when multiple lamps are used. An example of this is shown in Figure 2-5. Although these simulators generally provide a good Gaussian profile at the focus plane, "hot-spots" are found away from it, making heating with large test sections uneven (Petrasch et al., 2006, Mincuzzi et al., 2014). Secondly, there is uncertainty in the degree of polarisation, and lastly uncertainty of spectral radiance. These elements are especially important as they enable experimental repeatability, minimise experimental error, as well as provide information for more accurate modelling analysis. In contrast, laser heating is a more superior method of providing effective radiative heating as it is easy-to-control, its energy flux levels well-defined and it can be utilised to focus on a point or sheet with accuracy (Cozzani et al., 1995). As such, a laser was used as the main source of heating for the purpose of the present research.

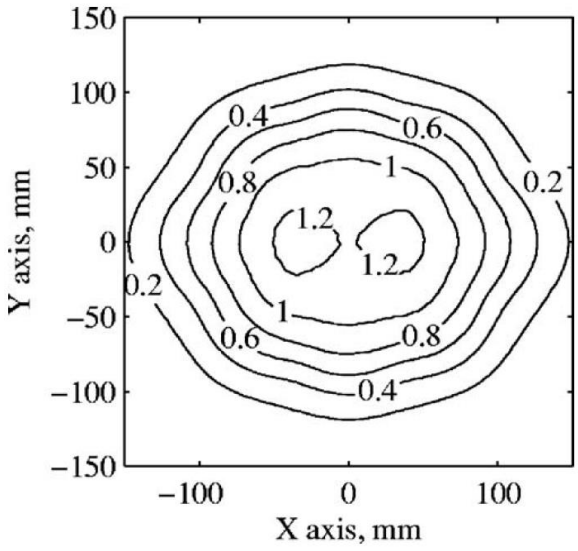

Figure 2-5: Example of radiative flux map in MW/m^2 with "hot-spots" in the radiative profile 150mm out of focus. Source: Petrasch et al. (2006).

A recent development in experimental methods provides new opportunities to achieve the high heating rates that are needed for the particle temperature to differ significantly from the fluid, while also avoiding strong interference to optical diagnostic methods. This development is the Solid-State Solar Thermal Simulator, SSSTS (Alwahabi et al., 2016). However, due to it being the first of its kind, the performance of system was not well-understood and has never been integrated into a research campaign. Hence, it is necessary to systematically and comprehensively characterise the SSSTS before incorporating it into experiments for the current research.

2.6. Summary of Literature Review and Research Gaps

Based on the literature review above, several research gaps were identified:

1. Lack of understanding of the characteristics and performance of the newly-developed Solid-State Solar Thermal Simulator (SSSTS) and how well it integrates in a research campaign
2. Lack of a spatially and temporally resolved particle temperature measurement technique to be used in a particle laden flow within a turbulent flow
3. Lack of experimental data on the influence of irradiation-induced buoyancy on heat and mass transfer in particle-laden flows

Therefore, the objective of this thesis is three-fold:

1. To properly characterise and integrate the recently-developed Solid-State Solar Thermal Simulator (SSSTS) into experimental systems
2. To develop a temporally and spatially resolved particle-temperature measurement technique that is applicable in turbulent flows based on the laser-induced phosphorescence (LIP) technique
3. To advance the understanding of the effect of irradiation-induced buoyancy on particle temperature, concentration, and distribution in laminar, radiatively-heated particle-laden jets. This is done using the technique developed in in Objective 2.

Chapter 3:

Experimental Methods

3. Experimental Methods

3.1. Overview

Chapter 3 presents the experimental methods used in this dissertation. The first section focuses on the development of an in-situ, spatially and temporally resolved particle temperature measurement technique applicable in a high volumetric loading environment with unsteady flow, while the second focuses on the application of the developed technique on a radiatively-heated particle-laden jet flow.

For all investigations, the experiments can be divided into three main parts – the radiative heat source, the two working sections, and the optical arrangement. The radiative heat source and optical arrangement were kept constant for the length of the thesis, while the working sections were modified to fulfil the needs of the various stages of the present dissertation.

Table 3-1 presents a summary of the experimental campaigns conducted throughout this candidature. The first three experiments (I-III) were performed with an optically-accessible fluidised bed as the working section. This arrangement was used in the development of in-situ, single-shot particle temperature measurement techniques, as well as in the characterisation of a unique radiative heat source developed in-house. The set up was chosen to allow for the developed thermometry techniques to be tested to measure particle temperature under unsteady, fast moving conditions. The recirculation of particles within the fluidised bed test section also allows for higher residence times in the heating region, therefore enabling testing of the techniques on high particle temperatures. Conversely, Experiment IV was performed with a particle-laden jet flow seeded within a wind tunnel, where the developed thermometry techniques were applied to particles in a well-known laminar flow condition.

Table 3-1: Summary of experiments conducted in the present candidature.

Experiment	***Working Section***	***Purpose***
I	Optically-accessible Fluidised bed	Characterisation of the Solid-State Solar Thermal Simulator
II	Optically-accessible Fluidised bed	Development of area-averaged, single-shot particle temperature measurement technique
III	Optically-accessible Fluidised bed	Development of single-shot, planar particle temperature measurement technique
IV	Particle-laden Jet in a Wind Tunnel	Investigating effect of radiative heating on heat and mass transfer of particles

3.2. Optically-accessible Fluidised Bed Experiments

3.2.1. Equipment

Figure 3-1 presents an optically-accessible fluidised bed used to suspend particles in an unsteady flow. It can be seen in Figure 3-1(a) that the fluidised bed has four 32mm diameter circular apertures diametrically opposed, two to allow for heating and excitation lasers to pass through and two for optical measurement access. Air jets were placed at each optical access-enabling aperture, as seen in Figure 3-1(b), to provide aerodynamic sealing to mitigate particle egress. During investigations, it was found that ZnO:Zn thermophosphors have a tendency to aggregate, consistent with findings by Abram et al. (2013). As such, a mix of ZnO:Zn TPs and $CaSO_4 \cdot 2H_2O$ particles were chosen to be placed in the fluidised bed and dry air was used to fluidise the particles. These were done to avoid humidity and mitigate the propensity for particle agglomeration in the system. A mass flow controller (Alicat Scientific, MC 20slpm) was used to deliver a constant airflow of 6.5L/min to the fluidised bed via two inlets, with the air flow subsequently passing through a layer of glass beads and sintered plate designed to generate uniform fluidising streams into the bed. Three K-type thermocouples, one placed on the outer surface of the top of the fluidised bed to monitor the temperature of the system, while the second and third were placed inside the fluidised bed 50mm above and below the heating region respectively to measure the overall change gas temperature due to convective heating from the heated particles.

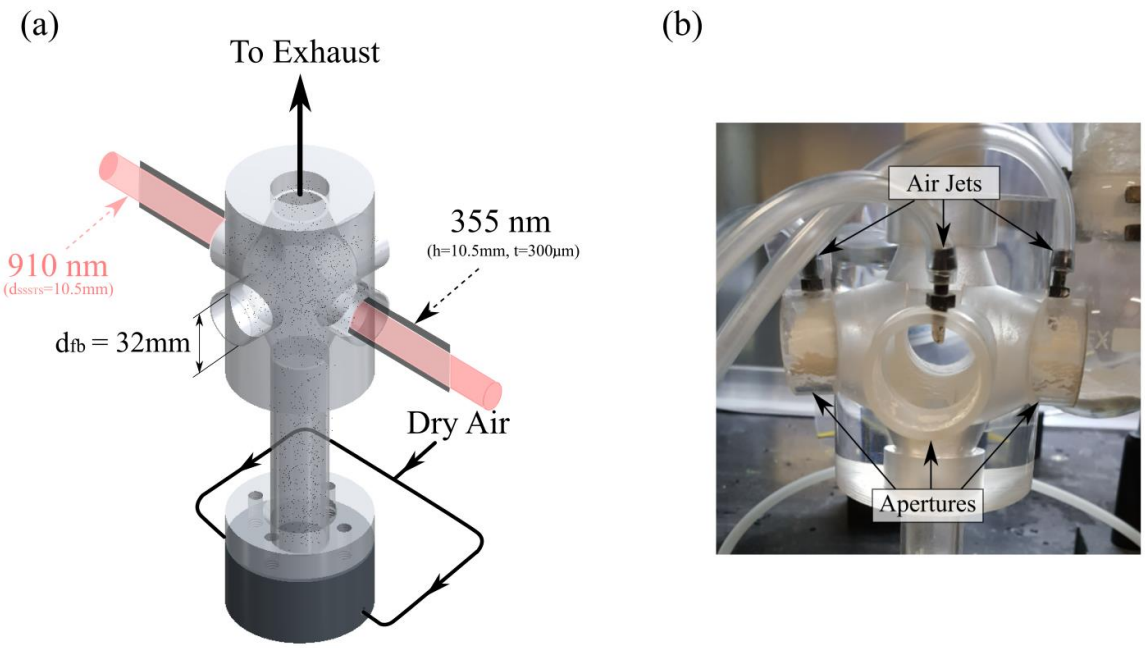

Figure 3-1: (a) Schematic diagram of the optically-accessible fluidised bed used for the development of particle temperature measurement technique. Thermophosphors, which are suspended in the fluidised, are heated with a 910nm wavelength radiative heating with a beam diameter of 10.5mm and excited with a 355nm Nd:YAG laser (10.5mm×300μm); (b) Air jets supplied to the optical access-enabling apertures of the fluidised bed to provide aerodynamic sealing to mitigate particle egress.

3.2.2. Optical Arrangement

Figure 3-2 presents the optical arrangements used for Experiments I and II to characterise the solid-state solar thermal simulator (SSSTS) and to develop the area-averaged, single-shot particle temperature measurement technique, respectively. Thermophosphors (TPs) in the working section were excited by the third harmonic of an Nd:YAG laser (Quantel Q-smart 850) operated at 5.27 ± 0.47mJ and 355nm. Investigations of the effect of excitation laser flux on particle temperature found that a 10% increase of laser flux corresponds to a 2% temperature increase/decrease. Therefore, the operating excitation laser fluence of 5.27 ± 0.47mJ was carefully selected, such that it is strong enough to deliver sufficient excitation to the TPs to result in strong phosphorescent signals, but not strong enough to heat up the particles. A polariser placed up-beam of the Nd:YAG laser was used to manipulate the laser fluence to the desired energy. Three cylindrical lenses were positioned in series to collimate the excitation laser beam into a 0.3mm (t)× 18mm(h) laser sheet in the test section. This formation of a thin excitation laser sheet is important as it provides spatial resolution in the out-of-plane direction, allowing the planar particle temperature measurements to be measured.

Additionally, the laser beam path (blue line) was aligned such that it offsets the SSSTS beam path (red line) by 7° and intercepts in the 10.5mm waist at the centre of the test section. A UV silica plate was placed 300mm away from the Fibre-Optic Head (FOH) to split the laser beam into a 92:8 ratio and subsequently directed into water-cooled power meters (Gentec model HP100A-4KW- HE), which acted as beam dumps as well as provide in-situ power measurements at a sample frequency of 10Hz. This was done to enable measurements of irradiative power before and after the test section, which would provide a measurement of radiative heat absorbed by particles in the working section. When operated at high power (>500W), it was observed that the temperature of the FOH approaches 70°C, which significantly reduces the electro-optical efficiency of the SSSTS. As such, a constant flow of air was provided across the FOH, and a K-type thermocouple was attached to the housing of the FOH to monitor and ensure an operating temperature between 18°C and 30°C.

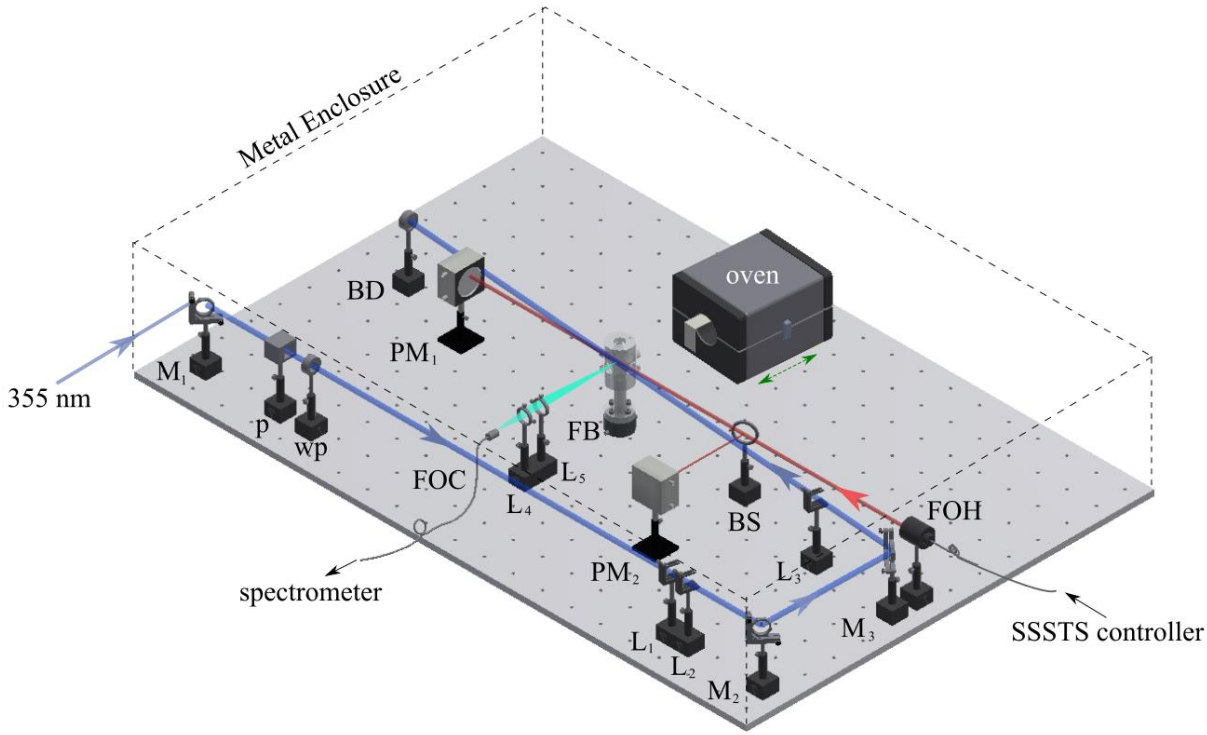

Figure 3-2: Optical arrangement for Experiments I and II to characterise the solid-state solar thermal simulator (SSSTS) and to develop the area-averaged, single-shot particle temperature measurement technique . Blue line: 355nm Nd:YAG laser beam path; Red line: 910nm SSSTS heating laser beam path; Cyan line: optical collection by fibre-optic cable (FOC) of phosphorescent emission. BD: Beam Dump; BS: Beam Splitter; L: Lens; M: Mirror; P: Polariser; PM: Power Meter; wp: waveplate; FOH: Fibre-Optic Head of the SSSTS.

Figure 3-3 presents an example of phosphorescent emissions of ZnO:Zn thermophosphors within the excitation laser sheet. It can be seen here that while a mix of ZnO:Zn TPs and $CaSO_4 \cdot 2H_2O$ particles were present in the working section, only TPs within the laser sheet produced phosphorescent emission signals. The phosphorescent emission signals from the whole area were collected using a round-to-linear fibre-optic cable (Thorlabs, BFL200HS02) via two light-focusing optic lenses. The resultant single-shot signals collected by the fibre-optic cable were those averaged over the 0.3mm (*t*)× 18mm(*h*) area of the laser sheet. These signals collected were then recorded with a spectrometer (Princeton Instruments-Acton Series Spectro-graph) with 600 grooves per mm grating. The spectrometer gain, gate width, and gate delay were set to 1, 26ns, and 51ns respectively, to ensure maximum phosphorescent signals from the ZnO:Zn TPs were collected.

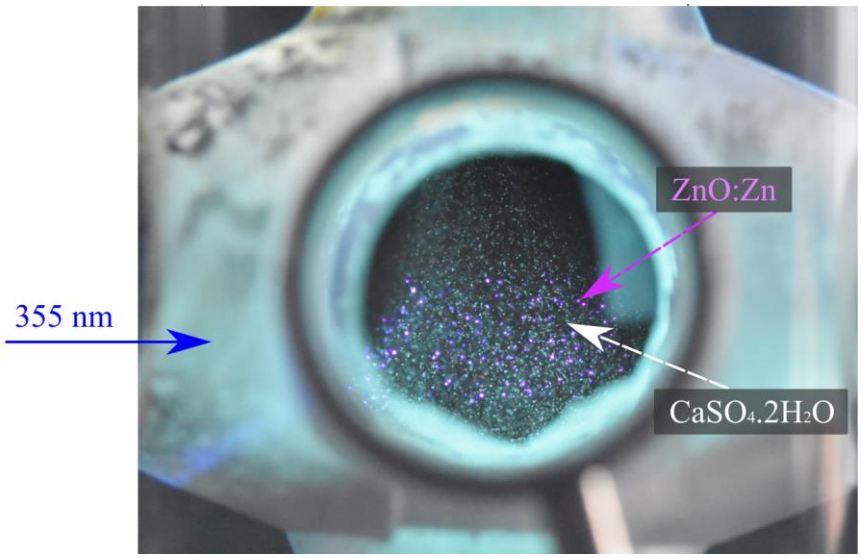

Figure 3-3: Excitation of ZnO:Zn and $CaSO_4 \cdot 2H_2O$ mixture using the 355nm Nd:YAG laser. Only ZnO:Zn thermophosphors within the 0.3mm (t)× 18mm(h) excitation laser sheet emits phosphorescent signals.

For safety, the entire system was enclosed within a metal box with safety interlocks where the operation of the SSSTS is not possible unless several criteria were achieved. These include ensuring water supply for the power meters were turned on, making sure temperatures recorded by thermocouples placed in and around the system were below 30°C, doors to the laboratory were locked, air supply to cool down the fibre optic head was turned on, and the metal enclosure was completely closed. The temperature of all thermocouples (including the ones mounted in

the fluidised bed and SSSTS systems) were monitored with a digital-to-analogue converter and recorded to a computer at a rate of 0.0167 Hz. Conditions within the closed metal enclosure can be monitored via signals transferred from the two monitoring cameras placed inside the metal enclosure.

Figure 3-4 presents the optical arrangement for Experiment III, where single-shot planar particle temperature measurements were performed. It can be seen that the optical alignment of the current experiment was kept the same as Experiments I and II, with the exception of an ICCD camera (PI-Max/PI-Max2, Princeton Instruments) fitted with an image splitter (Opto-Split II, Cairns Research) in place of the fibre-optic cable, as seen in Figure 3-4. Since two images can be taken simultaneously with the image splitter, potential errors associated with different time-delays and/or angular distortion that are typical of using traditional two-camera systems are avoided. Two high transmission (>93%) interference filters at 392 ± 9nm (FF01-392/18-25, Semrock) and 440 ± 20nm (FF01-440/40-25, Semrock) were placed within the image splitter, which uses an in-built conventional dichroic mirror to split the image 50:50. The selection of the interference filters were based on the sensitivity of ZnO:Zn TP spectra to temperature change, and were chosen to enable maximum signal capture. Additionally, an f/2.8 Tamron imaging lens and a 40mm spacer were used on the image splitter to ensure that the viewing region was a 15mm × 10.8mm area. This resulted in a spatial resolution of 51μm/pixel. The camera gain, gate delay, and gate width were set to 5, 51ns, and 26ns respectively. Due to the short decaying lifetime of the ZnO:Zn TPs, the ICCD camera was triggered by the Nd:YAG laser pulse timing to ensure image collection was performed after excitation.

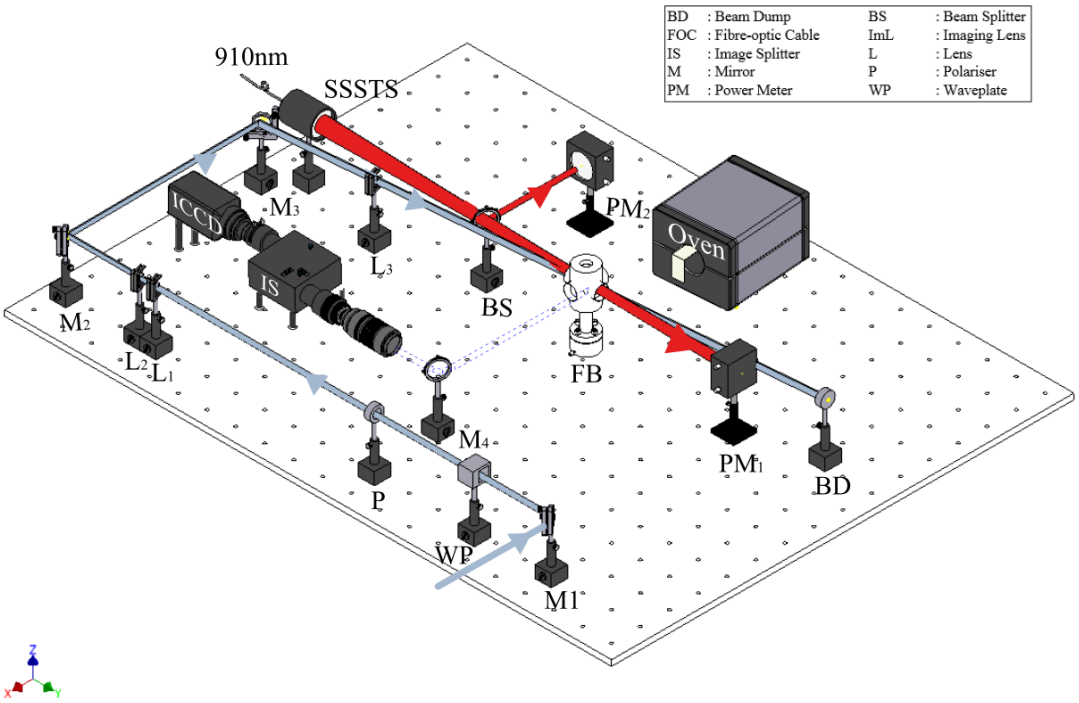

Figure 3-4: Optical arrangement for Experiment III, where planar particle temperature measurements were performed. Labels are presented in the intext table. Blue line: 355nm Nd:YAG laser beam path; Red line: 910nm SSSTS heating laser beam path.

3.2.3. Methodology

3.2.3.1. Calibration

Calibration experiments were performed at the start of every experiment to relate phosphorescent emissions to particle temperature. The calibration optical arrangements matched those described in Figure 3-2 and Figure 3-4, with the exception of a ZnO: Zn TP-coated flat plate placed in an oven (MTI Corporation, OTF- 1200X-S) in place of the fluidised bed and wind tunnel. A separate K-type thermocouple was attached to the surface of the TP-coated plate to measure the temperature of the TP during calibration. The calibration was performed for 45 temperatures ranging from 22°C to 400°C and at each temperature, the thermophosphor-coated plate was allowed to reach thermal equilibrium, as measured by the attached K-type thermocouple, before 400 single-shot phosphorescence spectra and images were recorded.

Figure 3-5 presents the phosphorescent emission spectra of the ZnO:Zn thermophosphors for temperatures between 22°C and 300°C and two spectral bands, I_1 = 410nm – 440nm and I_2 = 383nm – 401nm to be used for relative temperature dependency. These spectral ranges

were chosen to optimise temperature sensitivity and signal-to-noise ratio. It can be seen here that all exhibit the same trend, i.e., a clear right shift in the peak wavelength position with increased temperature. This demonstrates the sensitivity of ZnO:Zn emission spectrum to temperature within the recorded temperature range. Although a decrease in phosphorescence signal was observed with increased temperature, in line with the findings of Abram et al. (2015), good signal levels were still detected.

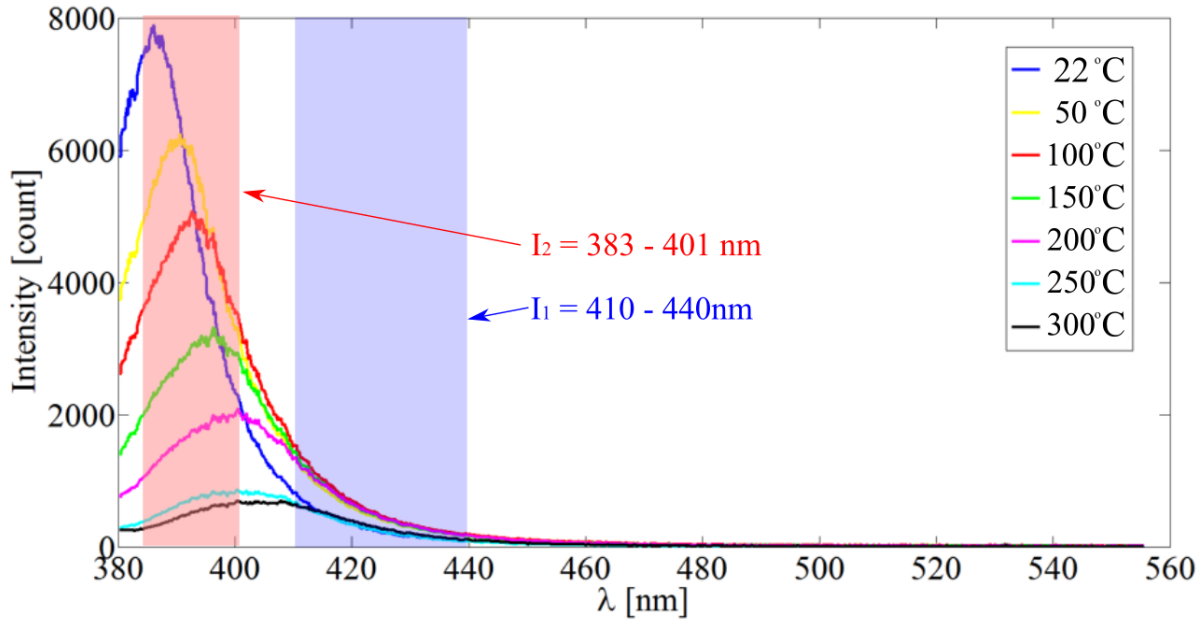

Figure 3-5. Phosphorescence emission spectra of ZnO:Zn thermophosphors at temperatures between 22°C and 300°C and the two spectral bands, I_1 = 410nm – 440nm and I_2 = 383nm – 401nm to be used for relative temperature dependency.

Figure 3-6 shows a typical signal-to-noise ratio, where the typical strongest and weakest peak signal from the ZnO:Zn TP emission were presented in Figure 3-6(a) and (b) respectively. It should be noted that the spectra presented in Figure 3-6(b) was scaled to approximately 100 times the actual signal. It is evident that at low temperatures where the signal is the strongest, the noise is negligible. For the case where the signal is the weakest (Figure 3-6(b)), the resulting signal-to-noise ratio (SNR) is still 22.8.

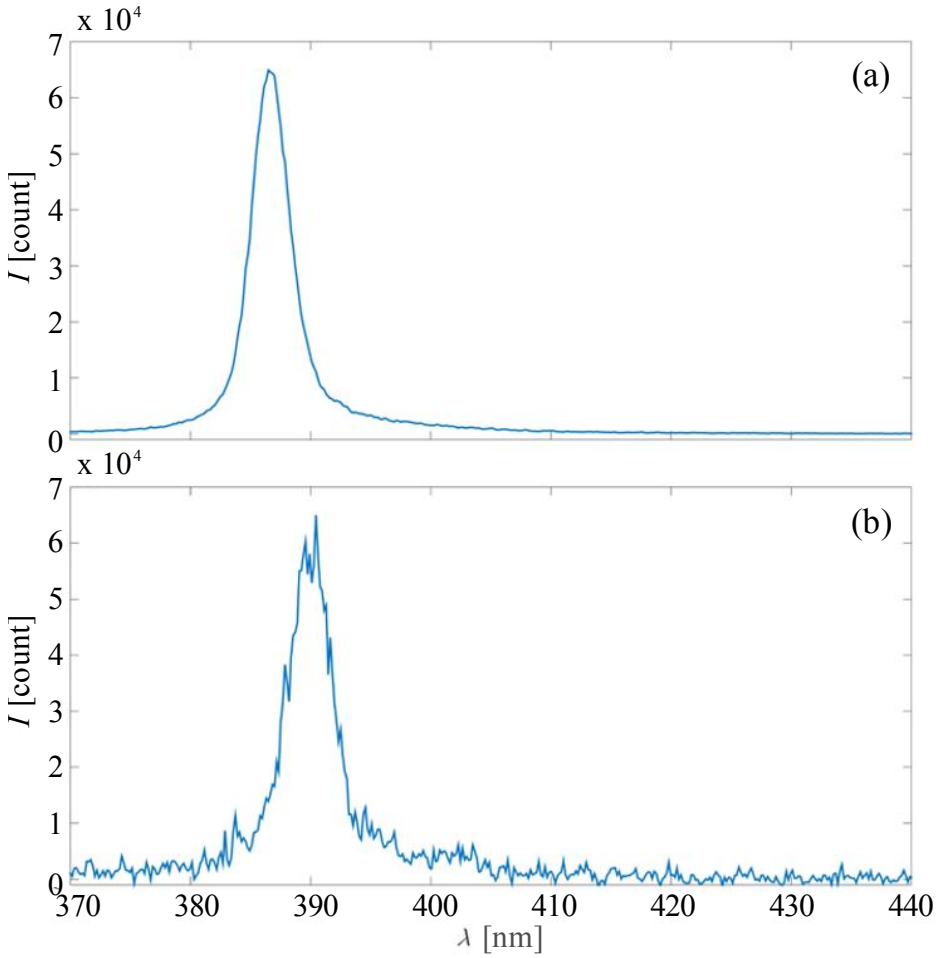

Figure 3-6: Typical single-shot spectrum signal and signal-to-noise ratio of ZnO:Zn excited at 355nm. (a) Strongest signal strength before signal reaches saturation; (b) Typical weak signal presented approximately 100 times its signal strength.

3.2.3.2. Experiments

For Experiments I – III, particles in the optically accessible fluidised bed were simultaneously subjected to excitation by the 355nm Nd:YAG laser and radiative heating by the SSSTS. Temperatures of the heated particles were measured for heat fluxes, $\dot{Q}_{rad}$, in the range of 2.4 MW/m^2 $\leqslant \dot{Q}_{rad} \leqslant$ 21.1 MW/m^2. For each of these measurements, the first 50 ($\approx$30s) and last 100 ($\approx$60s) of the 800 total shots were recorded with the SSSTS deliberately switched off to enable investigation of heating and cooling of particles. Background measurements were also taken at the start of each experimental campaign with the SSSTS switched off and without the presence of particles.

3.2.3.3. Post-Processing

For Experiments I and II, the intensity ratio, I_1/I_2, was calculated by deducting the background signal and dividing the sum of phosphorescent signal intensity at 383nm – 401nm, $\sum_{\lambda=383}^{401} I_\lambda$, and at 410nm – 440nm, $\sum_{\lambda=410}^{440} I_\lambda$, against each other, such that:

$$\frac{I_1}{I_2} = \frac{\sum_{\lambda=410}^{440} I_\lambda}{\sum_{\lambda=383}^{401} I_\lambda} \quad (1)$$

These intensity bands were chosen from commercially available filter bandwidths to provide the maximum intensity ratio without compromising spectral resolution.

An investigation of the influence of the excitation (355 nm) laser fluence revealed that I_1/I_2 varies by approximately 25% between laser fluence values of 2.6mJ/cm^2 and 5.17mJ/cm^2. To correct for this influence, a method proposed by Abram et al. (2013) whereby the I_1/I_2 is calculated by normalising the I_1/I_2 recorded at room temperature, $(I_1/I_2)_{ref}$:

$$\frac{I_1}{I_2} = \frac{I_1}{I_2} \times \frac{I_{2,ref}}{I_{1,ref}} \quad (2)$$

For Experiment III of the current dissertation, where spatially-resolved particle temperature measurements were performed, split images recorded by the ICCD camera fitted with image splitter were recorded side-by-side, with the combined images spanning a 15mm × 10.5mm area. Figure 3-7 presents the image processing procedure, the steps of which are outlined below:

a) I1 taken at 440 ± 20nm; (b) I2 taken at 392 ± 9nm; (c) the super-position of two images after thresholding data below 1000 counts; (d) particle temperatures inferred from I1/I2 and calibration data.

1. The original images were divided into two sub-images using in-house Matlab scripts, as seen in Figure 3-7(a) and (b) which were taken with 440 ± 20nm and 392 ± 9nm filters respectively.
2. Each instantaneous image was subtracted with the average pixel count of the background images to remove electrical noise. The resultant signal-to-noise ratio (SNR) for the images taken with the 392 ± 9nm filter varied from 13 at $\dot{Q}_{rad}$ = 0W/m^2 to 5.6 at $\dot{Q}_{rad}$ = 21.1MW/m^2. Conversely, the SNR for the images taken with the 440 ± 20nm filter were between 5.4 at $\dot{Q}_{rad}$ = 0 W/m^2 and 11 at $\dot{Q}_{rad}$ = 21.1 MW/m^2. This is due to

a shift in the phosphorescent emission spectra as the particle temperatures increase due to increasing heat flux.

3. Each pixel with signal intensities less than 1000 count was thresholded to account for excited thermophosphor particles not in the focusing plane of the camera. This was done to ensure non-physical data where particles appear artificially larger than their actual size do not bias the overall data.
4. Particle sizes were distinguished from pixel counting. Due to weak phosphorescent signals at the outer edges of the particle agglomerates leading to low signal-to-noise ratios, the weighted centroid of each particle agglomerate was found and used to reject signal from the pixels at the outside of the particles.
5. The two sub-images were super-positioned to overlap each other to within plus/minus 0.1 pixels. This was achieved by utilizing the same image processing method as for the superposition the sub-images with a gridded target, which enables the average offset between the two sub-images to be calculated.
6. Arrays of intensity ratios, I_1/I_2, were then calculated by dividing the two sub-images on a pixel-by-pixel basis, as presented in Figure 3-7(c).
7. Particle temperatures were then inferred from I_1/I_2 and from the calibration curve, as seen in Figure 3-8.

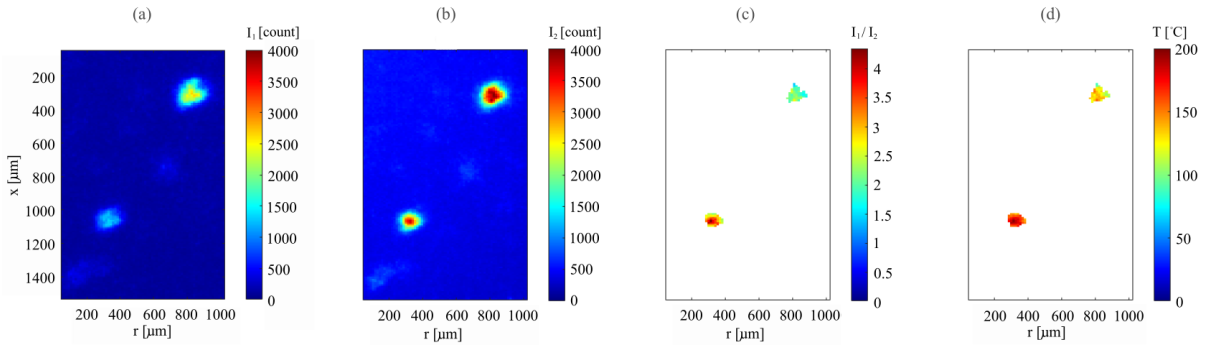

Figure 3-7: Image processing procedure: (a) I_1 taken at 440 ± 20nm; (b) I_2 taken at 392 ± 9nm; (c) the super-position of two images after thresholding data below 1000 counts; (d) particle temperatures inferred from I_1/I_2 and calibration data.

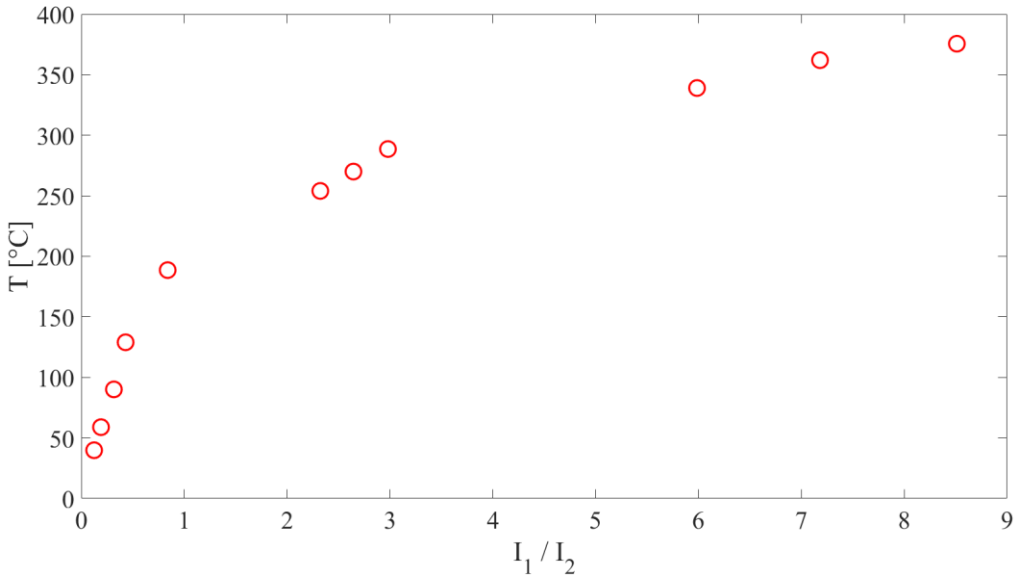

Figure 3-8: Plot of calibration curve for planar measurement depicting relationship between intensity ratio and temperature.

3.3. Particle-laden Jet Experiment

3.3.1. Equipment

Figure 3-9 presents the working section used in Experiments IV of the present dissertation, where investigations were carried out on particle-laden jet flows in a 300mm × 300mm vertical wind tunnel. The dimensions of wind tunnel were designed to ensure minimal boundary effects to the imaging region. Similar to the optically-accessible fluidised bed, the wind tunnel has three apertures – two to enable heating and excitation beam path access, and one for optical measurements. Two optical shields were also placed within the wind tunnel to ensure particles do not deposit onto the aperture windows during experiments. This was done to ensure that the particles do not interfere with measurements, and in the worst-case scenario, extreme heating of particles deposited in the path of the SSSTS beam would damage the wind tunnel. A combination of two screens and a honeycomb layer were placed directly below the wind tunnel inlet to generate nominally uniform co-flow with negligible boundary effects within the imaging section.

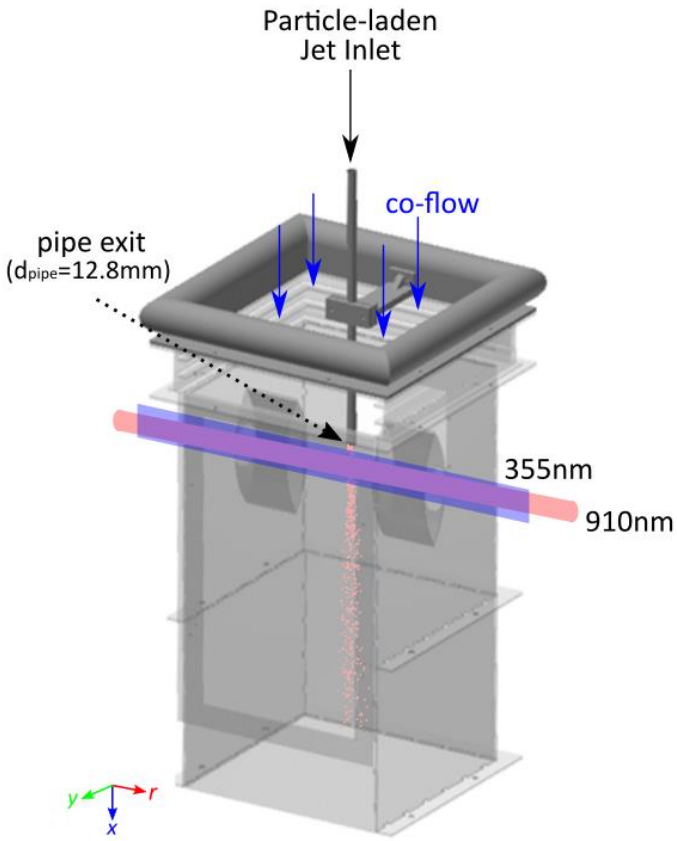

Figure 3-9: Particle-laden jet seeded through a 12.8mm pipe into a 300mm × 300mm wind tunnel. Blue laser path indicates the 355nm Nd:YAG laser, while red laser path indicates the 910nm SSSTS heating beam.

A laminar particle-laden jet was produced from a pipe with diameter, d_{pipe} = 12.8mm, placed in the centre of the wind tunnel. The pipe length-to-diameter ratio was kept at 39.1, a ratio sufficient to establish a fully-developed laminar flow in a single phase flow, although the required length for a fully-developed laminar, two-phase flow is not well-understood.

Figure 3-10 presents a fluidised bed feeder used to seed the particles into the test section at a volumetric mass flow rate of 13L/min. Dry air and a pressure-controlled system were used in this fluidised bed feeder to minimise agglomeration common in TPs. Here, dry air was introduced into the system via two inlets. A primary air flow of 12 L/min was fed from the bottom of the fluidised bed feeder to maintain the fluidisation, while a secondary air flow of 1 L/min was transported through the pipe to ensure the particles were seeded into the wind tunnel. For both streams of airflows, mass flow controllers (Alicat Scientific, MC 20 SLPM and MC 5SLPM) were used to maintain the volumetric flow rate. Two valves, one at the inlet of the secondary air and one on top of the feeder, were used to control the pressure within the feeder

and particle mass loading in the system. Although most of the particles were transported through the 1mm hole by the primary air stream, some of the smaller particlers were unavoidably transported through the bypass stream (colored in red in Figure 3-10), resulting in two distinctly different particle size ranges.

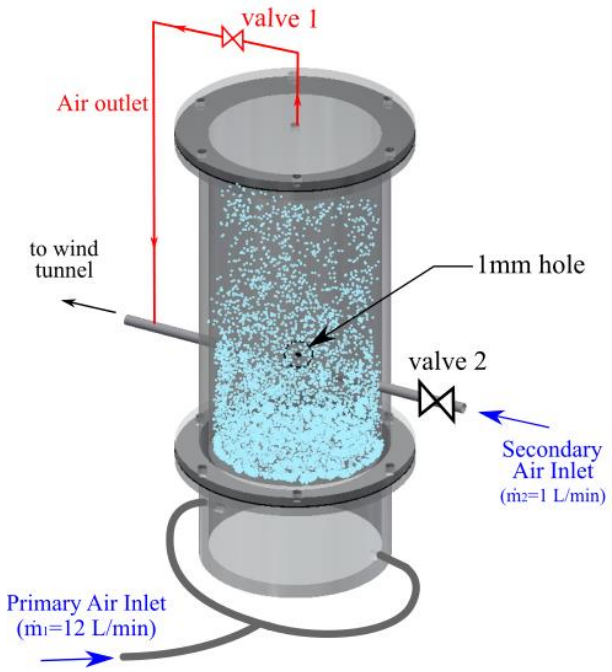

Figure 3-10: Schematic diagram of fluidised bed feeder used to deliver particles into the test section.

3.3.2. Optical Arrangement

The experimental set up for Experiment IV is similar to that described for Experiment III with the exception of the wind tunnel replacing the optically-accessible fluidised bed. For this setup, the SSSTS beam was placed 2mm below the pipe exit ($0.2 \leq x/D \leq 0.8$), and the viewing area of the ICCD camera was placed directly at the jet exit, to allow for viewing of half of the particle-laden jet. The viewing region was a 15mm × 10.8mm area, starting at $r/D = 0$ and $x/D = 0.04$. This area was specifically chosen to enable investigation of the particle-laden flow upstream and downstream of the heating region.

3.3.3. Methodology

For the second section of the thesis, temperatures of ZnO:Zn particle aggregates and their respective positions were investigated at 13 different heat fluxes between 0 MW/m^2 and 35.3 MW/m^2. For each flux, 4000 single-shot planar images were collected over several days to ensure repeatability. Calibration, experimental, and post-processing processes developed from the first section of the thesis were similarly applied.

3.4. Particle Characterisation

The first order theoretical model as described by Equation 2-1 was used to calculate the approximate operating temperature for all investigations in the scope of this candidature. It was determined that the expected temperature range would not exceed 627°C, making the ZnO:Zn the most appropriate TP as it has the highest temperature sensitivity within the expected operating temperature (Aldén et al., 2011). Additionally, due to the expected short residence time of the particles in the heat source, the short decaying lifetime of ZnO: Zn is advantageous for single-shot measurements.

Although ZnO:Zn TPs (Phosphor Technology) were specified by manufacturing data to have a size distribution of 2µm to 8µm, it was found during investigations that the sole use of these TPs led to significant agglomeration. This is in line with previous investigations by Abram *et al.* (2013). As such, a dry sample of ZnO: Zn was analysed with a Mastersizer 2000 particle sizer (Malvern Instruments). Figure 3-11 shows the particle aggregate size distribution as measured by the Masetersizer 2000. It found that despite having ultrasonic waves in the Mastersizer to break apart the agglomerated particles, the ZnO:Zn particle size distribution ranged between the nanometer range to 80µm (see Figure 3-11). This is further supported by scanning electron microscope (SEM) images taken of ZnO:Zn samples, as seen in Figure 3-12.

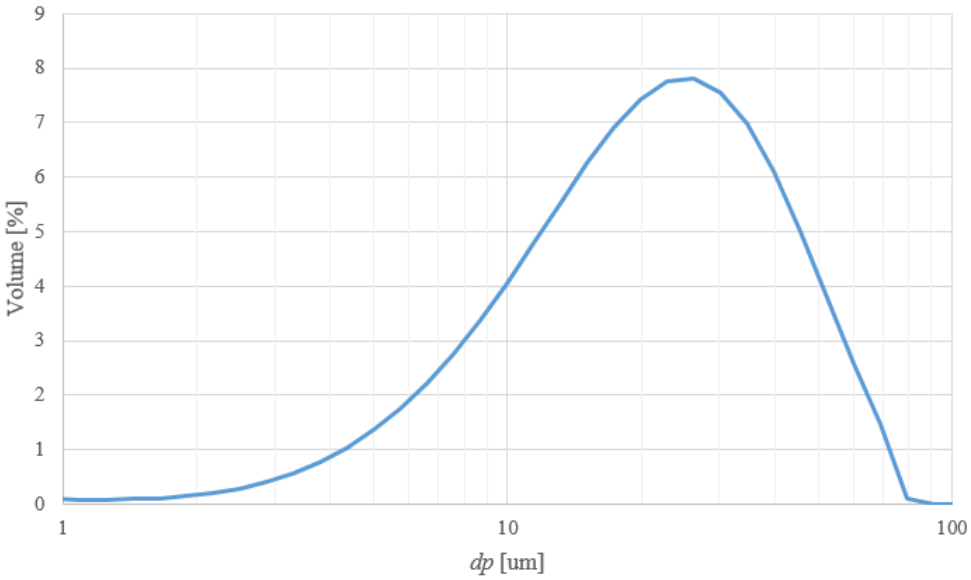

Figure 3-11: Particle aggregation size distribution obtained from the Mastersizer 2000 (Malvern Instruments).

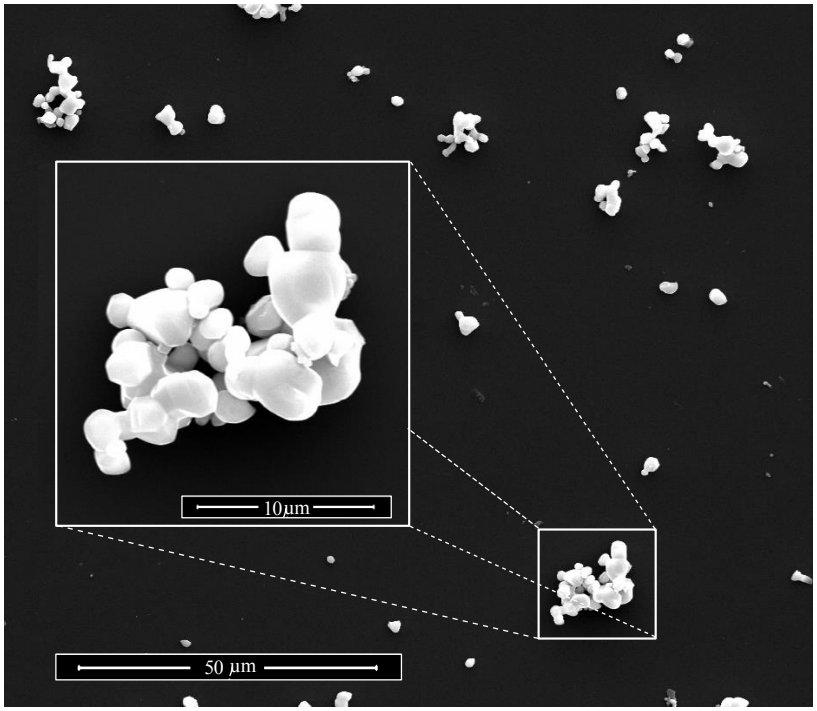

Figure 3-12: Example of ZnO:Zn agglomerates, taken with an SEM micrograph.

Chapter 4:

Characterising the Solid-State Solar Thermal Simulator

4. Solid-State Solar Thermal Simulator

4.1. Overview

The development of accurate particle temperature measurement techniques is a challenging process that requires having a reliable heat source whose characteristics are well-understood is an integral part of this thesis research. To aid in this, a 3.2kW Solid-State Solar Thermal Simulator (SSSTS) was developed at the University of Adelaide. Given that it is the first of its kind, it is necessary to properly characterise the performance of this device. The present chapter addresses this challenge. It should be noted that this chapter is based on materials previously published by Alwahabi et al. (2016), but focuses on components primarily done as part of this thesis campaign.

The SSSTS is comprised of 41 fibre-coupled diode laser modules (Nlight, Model e06.0900915200), each producing ~80W of continuous power at 45-55% efficiency. A pilot light operating at 16mW and a visible wavelength of 658nm was also included in the SSSTS to aid in the alignment of heating beam culminating from the system. The laser-fibre modules (LFMs) are divided into 6 groups (labelled Groupes I-VI in Figure 4-1) of 7, with each group spliced into a laser combiner (labelled C_L in Figure 4-1). The combined groups were then further bundled into a custom-built fibre combiner with a fibre-optic head, FOH, to deliver the radiative output. The FOH is comprised of an adjustable three-lens system with an effective focal length of 80.2mm and a focal diameter of 50mm. Cooling plates connected to an external water chiller (Polyscience 6500 Series Chiller) and in-built thermocouples within each group were also installed to maintain operating temperature of the SSSTS between 18°C and 30°C. To obtain the desirable radiative heat fluxes from the SSSTS, the electrical input power of the SSSTS is changed via an in-built PC.

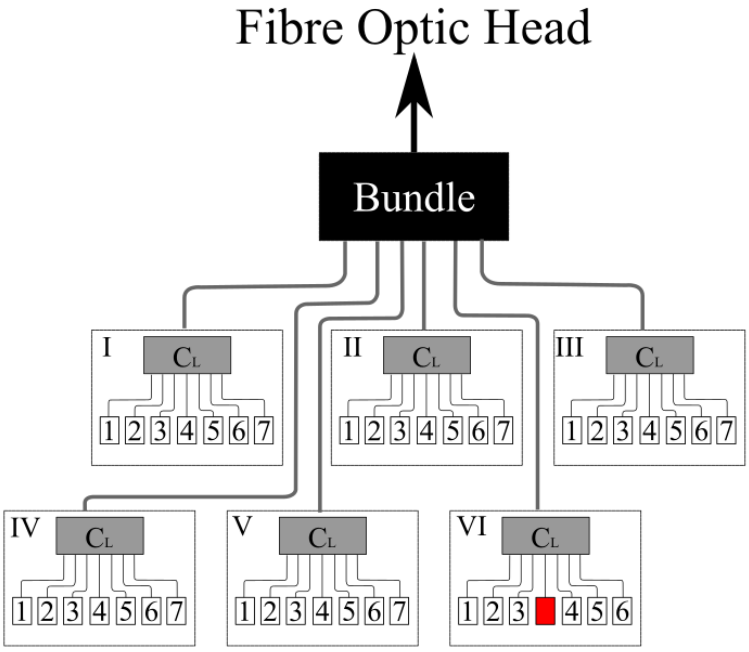

Figure 4-1: A schematic diagram of the forty-one power-delivering laser fibre modules (LFMs) labelled 1-7, grouped into 6 (I-VI), which deliver light to the Solid State Solar Thermal Simulator (SSSTS). A visible pilot light (coloured red) is also included in the system to aid in the visualisation of output radiation beam path from the Fibre-optic head (FOH).

4.2. Characterisation of the Solid-State Solar Thermal Simulator

To characterise the SSSTS, the optically-accessible fluidised bed experiment set up described in Section 3.2 was used. Additionally, the beam profile of the SSSTS on the surface of the power meter was recorded with an SLR camera ((Nikon D5500 with Tamron f = 90 mm Macro lens). Figure 4-2 presents the beam profile of SSSTS taken at 920mm from the FOH (black line) compared to simulated typical Gaussian (blue dashed line) and top-hat profiles (red dash-dot line). The same near top-hat profile was observed, regardless of the distance from the FOH, with only the radial distance changing, making the SSSTS a true point source. This addresses the need identified in Chapter 2.5, where a heat source with a uniform radiation profile is needed for a well-controlled heating region.

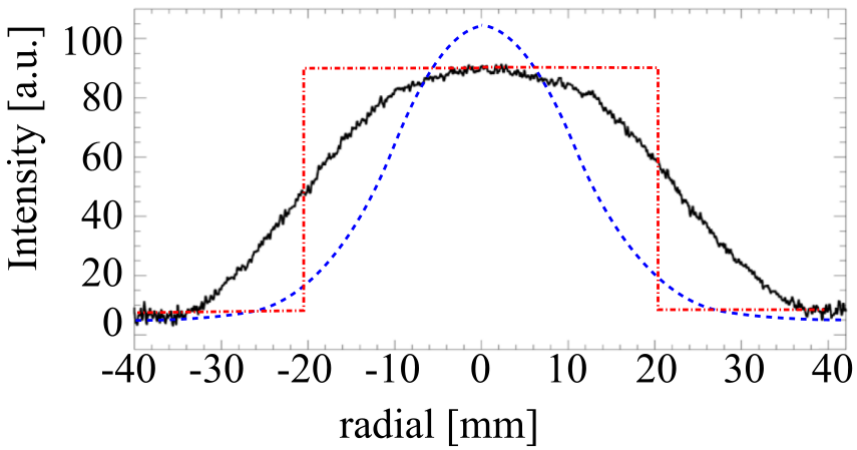

Figure 4-2: Beam profile of the SSSTS (black continuous line) taken at 920mm from the fibre-optic head (FOH), compared to a Gaussian profile (blue dashed line) and a top-hat profile (red dash-dot line).

Figure 4-3 presents the beam diameter convergence of the SSSTS, the waist (inset) at which all experiments in this dissertation were conducted. Each tick mark in the main and inset figures represent 10mm and 1mm respectively. It can be seen that the beam diameter, d_{SSSTS}, converges from 46mm at the FOH to a waist of 10.5mm ± 0.1mm at 520mm – 540mm from the FOH. Due to this convergence, different heat fluxes can be obtained by manipulating the test section distance from the FOH. However, to ensure constant heat flux throughout the working section, all experiments in this dissertation were conducted within this 20mm-length beam waist.

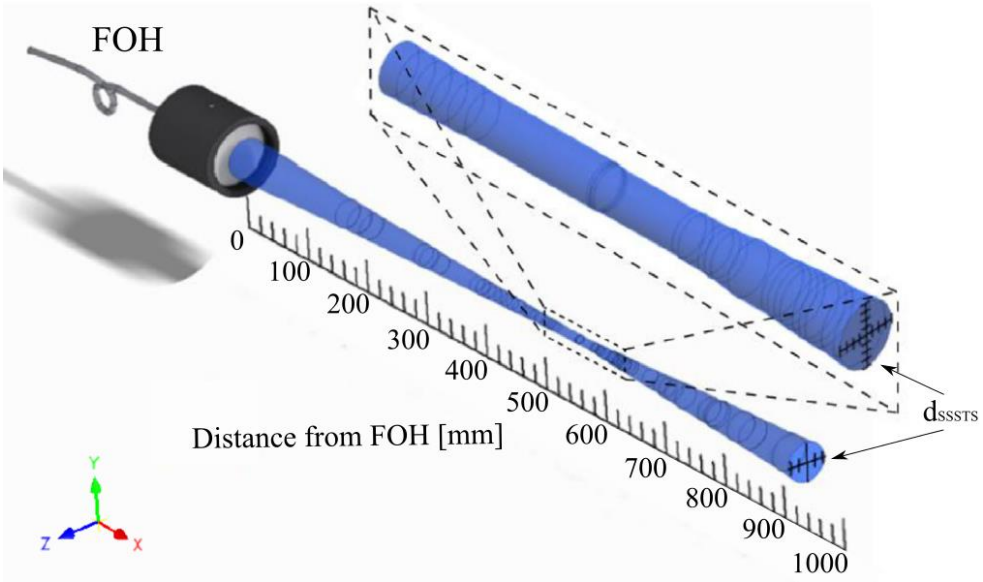

Figure 4-3: SSSTS radiative beam convergence with respect to the distance from the fibre-optic head (FOH). Each tick mark for the beam profile diameter, d_{SSSTS}, represents 10mm. Inset shows the SSSTS beam waist of 10.5mm between 520mm and 540mm from the FOH, where all experiments of this dissertation were conducted. Each tick mark in the inset figure is 1mm.

Figure 4-4 presents the change in radiative emission peak wavelength with respect to the operating temperature, as measured by the in-built thermocouple in Group VI of the SSSTS. It can be seen that the peak wavelength of the radiative source increases with increasing operating temperature, ranging between 904nm and 918.5nm when the diode temperature is between 17.2°C and 21.4°C. The wavelength change of the SSSTS can thus may be characterised by the equation:

$$\Delta\lambda_{peak} = 3.764\,\Delta T_{IV} \qquad 4\text{-}1$$

where ΔT_{IV} is the temperature measured by the thermocouple in Group VI of the SSSTS. Within this operating wavelength, the radiative emission can only be absorbed by the solid phase and not the gas, allowing for large temperature disparity scenarios between the two phases. Given the dependence of the emission wavelength on operating temperature, it is important that sufficient cooling be provided to the SSSTS to ensure consistent heating for all future experiments using this system.

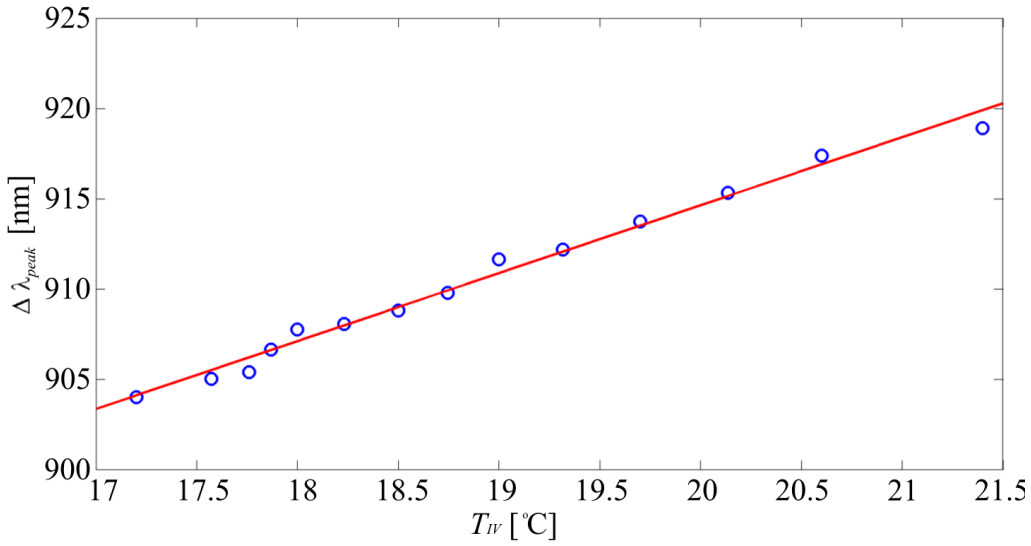

Figure 4-4: Change in peak wavelength of the SSSTS as a function of the operating temperature, as measured by the in-built thermocouple in Group VI.

As mentioned in Chapter 2.2, optimisation of CST systems often requires large-scale trials with low electrical efficiencies and there is a need for a more effective radiative heating equipment. As part of the characterisation of the SSSTS operation, the optical power output, $Q_{out,optical}$, temperature, T_{group}, and electro-optical efficiency, $\eta_{o\text{-}e}$, of each LFM group were measured for a range of input current between 2A – 17A. Here, $Q_{out,optical}$ was measured with a power meter, and $\eta_{o\text{-}e}$ calculated from the following:

$$\eta_{o-e} = \frac{Q_{out,optical}\,[W]}{Q_{in,elec}\,[W]} \qquad 4\text{-}2$$

Here, $Q_{in,elec}$ is calculated by multiplying the input current and voltage. The results are presented in Figure 4-5. It can be seen from Figure 4-5(a) that although groups I-V each have 7 LFM, the efficiency of each LFM group were not identical, with a maximum deviation of 20%. An overall maximum electro-optical efficiency was achieved at input current of 6A, with Groups VI and I having the highest and lowest efficiency of 55.3% and 47.2% respectively. Conversely, the power output increment shown in Figure 4-5(b) was found to increase with input current, with the $Q_{out,optical}$ for groups I-V being similar to each other, and group VI supplying much less. This is consistent with expectation, given the number of power-supplying LFMs present in each group. This trend was similarly found for the LFM temperatures seen in Figure 4-5(d).

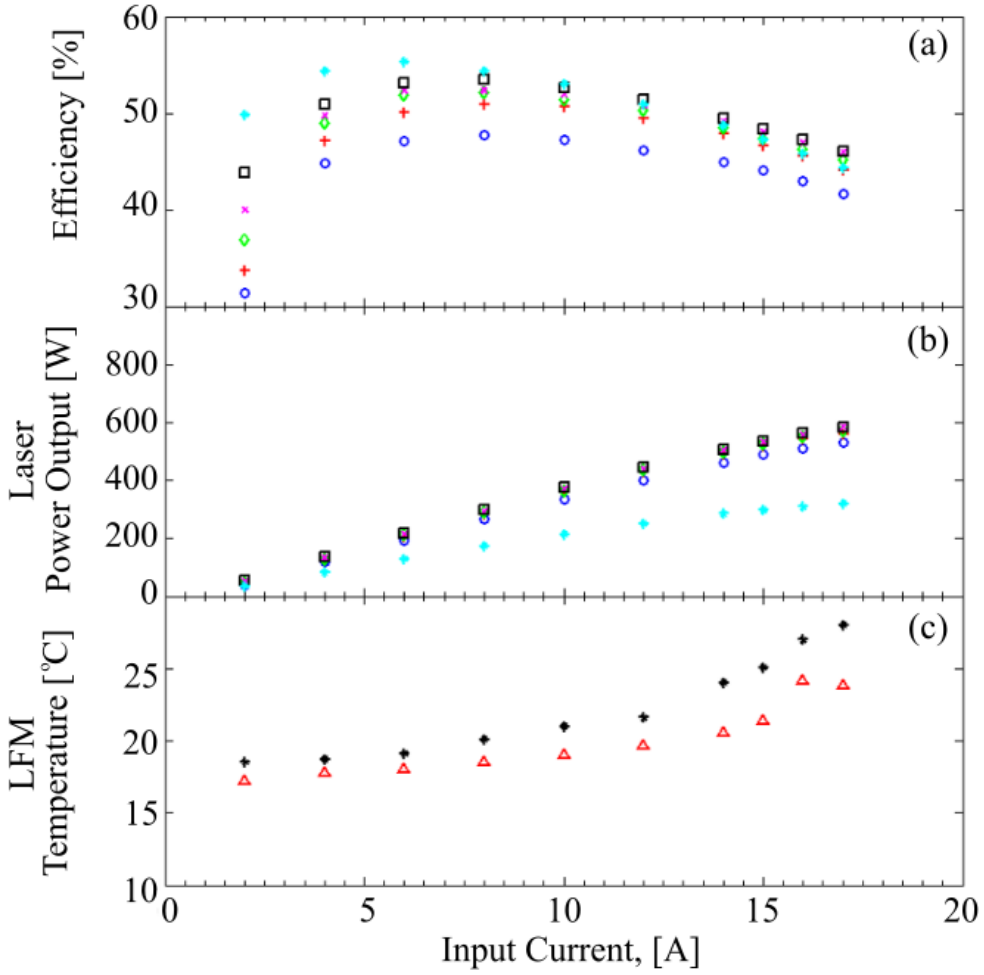

Figure 4-5: The Solid-State Solar Thermal Simulator (SSSTS)'s (a) electro-optical efficiency, $\eta_{o\text{-}e}$, (b) optical power output, $Q_{out,}$, (c) electrical input power, $Q_{in,\,elec}$, and (d) laser-fibre module (LFM) temperature ,T_{LFM}, as a function of the input electrical current, I. ○: Group I; +: Group II; ◇: Group III; ×: Group IV; □: Group V; ✤: Group VI; △: Groups I – V; ✦: Group VI.

Figure 4-6 presents the radiative flux with respect to input current, where the fluxes were calculated from three different beam diameter: (a) 10.5mm, (b) 20mm, (c) 40mm. This was done by dividing power outputs measured by the power meter against the beam diameters. It was found that a maximum input current of 17A results in a continuous power output of 3.18kW. At the beam waist where the diameter is 10.5mm, this translates to a maximum heat flux of 36.6 MW/m^2.

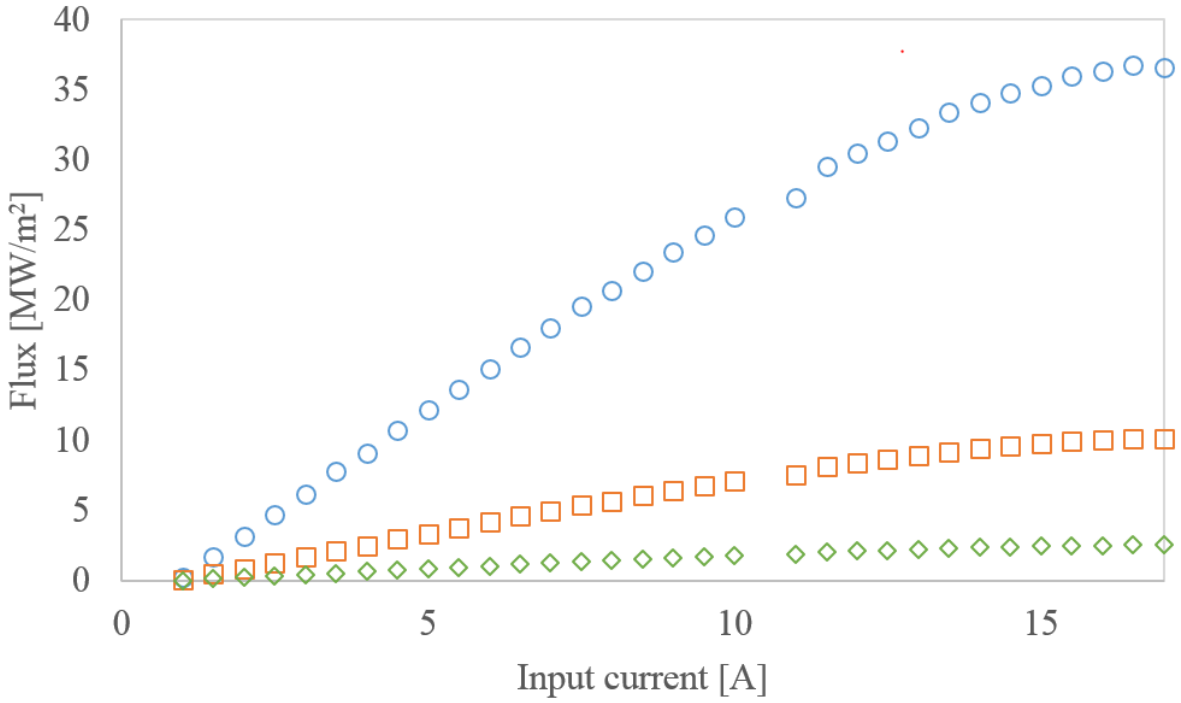

Figure 4-6: Calculated radiative flux from three different beam diameter with respect to input current. Circle: 10.5mm; square: 20mm; diamond: 40mm.

4.3. Conclusion

The characteristics and performance of the Solid-State Solar Thermal Simulator (SSSTS) was investigated in this chapter to determine its suitability to be incorporated into the current research. It was found that the SSSTS is a true point source and has a near top-hat radiative beam profile, enabling it to provide uniform heating regardless of the distance from the power-delivering fibre-optic head (FOH). Additionally, the SSSTS beam diameter was found to converge from 46mm at the fibre-optic head (FOH) to a waist of 10.5mm ± 0.1mm at 520mm – 540mm from the FOH. This constant 20mm-length beam waist is advantageous as it provides assurance of constant heat flux in this region. As such, all experiments of this dissertation were conducted in this region. The SSSTS operates at a peak wavelength of 911nm ± 7nm, depending on the operating temperature. This operating wavelength is important to the current research as it is only absorbed by the particle phase and not the gas phase, enabling conditions with high temperature disparity between the two phases.

Chapter 5:

Non-intrusive Temperature Measurement of Particles in a Fluidised Bed Heated by Well-characterised Radiation

Statement of Authorship

Title of Paper	Non-intrusive temperature measurement of particles in a fluidised bed heated by well-characterised radiation
Publication Status	☑ Published ☐ Accepted for Publication ☐ Submitted for Publication ☐ Unpublished and Unsubmitted work written in manuscript style
Publication Details	K.C.Y. Kueh, T.C.W. Lau, G.J. Nathan, Z.T. Alwahabi, Non-intrusive temperature measurement of particles in a fluidised bed heated by well-characterised radiation, International Journal of Multiphase Flow, 100 (2018) 186-195.

Principal Author

Name of Principal Author (Candidate)	Kimberley C.Y. Kueh		
Contribution to the Paper	Set up experimental arrangements, performed experiment, process and analyse results. Took primary responsibility of writing the paper and responding to the reviewers.		
Overall percentage (%)	60		
Certification:	This paper reports on original research I conducted during the period of my Higher Degree by Research candidature and is not subject to any obligations or contractual agreements with a third party that would constrain its inclusion in this thesis. I am the primary author of this paper.		
Signature		Date	23/08/2019

Co-Author Contributions

By signing the Statement of Authorship, each author certifies that:

i. the candidate's stated contribution to the publication is accurate (as detailed above);

ii. permission is granted for the candidate in include the publication in the thesis; and

iii. the sum of all co-author contributions is equal to 100% less the candidate's stated contribution.

Name of Co-Author	Timothy C.W. Lau		
Contribution to the Paper	Assisted in the processing of experimental results and editing of manuscript.		
Signature		Date	28/08/2019

Name of Co-Author	Graham J. Nathan		
Contribution to the Paper	Supervised the analysis of experimental results and assisted with editing the manuscript.		
Signature		Date	26/8/2019

Name of Co-Author	Zeyad T. Alwahabi			
Contribution to the Paper	Supervised the experimental campaigns and processing of results. Assisted with editing the manuscript.			
Signature			Date	

International Journal of Multiphase Flow 100 (2018) 186–195

Contents lists available at ScienceDirect

International Journal of Multiphase Flow

journal homepage: www.elsevier.com/locate/ijmulflow

Non-intrusive temperature measurement of particles in a fluidised bed heated by well-characterised radiation

Kimberley C.Y. Kueh[a,c], Timothy C.W. Lau[a,c], Graham J. Nathan[a,c], Zeyad T. Alwahabi[b,c,*]

[a] School of Mechanical Engineering, The University of Adelaide, SA 5005 Adelaide, Australia
[b] School of Chemical Engineering, The University of Adelaide, SA 5005 Adelaide, Australia
[c] Centre of Energy Technology, The University of Adelaide, SA 5005 Adelaide, Australia

ARTICLE INFO

Article history:
Received 26 May 2017
Revised 3 October 2017
Accepted 21 December 2017
Available online 27 December 2017

ABSTRACT

We report an important step towards the in-situ measurement of heat transfer in particle-laden flows via direct measurement of the temperatures of fluidised particles. Laser-induced phosphorescence (LIP) was employed to provide non-intrusive, temporally resolved and in-situ measurement of suspended particles as a function of heat flux and radiation attenuation. Excitation was performed at 355 nm with a repetition rate of 1.67 Hz. Particles were transported with dry air within an optically-accessible fluidised bed and heated with a well-defined source of high-flux radiation from a 3 kW solid-state solar thermal simulator radiation to achieve heating rates in order 23,000°/s. Particle and gas temperatures were measured simultaneously with the former determined from thermo-phosphorescent emissions following excitation at 355 nm. Irradiation flux and mass loading were found to play important roles in particle and gas temperature rise. Confidence in the method was obtained by verifying internal consistency between the energy absorbed by the particles and the temperature rise of the gas phase, taking into account the variability of particle mass loading.

1. Introduction

In-situ and instantaneous measurement of the temperatures of micron-sized particles within a turbulent environment is challenging. Currently, all of the methods reported of a system that provides the direct temperature measurement of particles suspended in a turbulent flow have limited spatial and/or temporal resolution. Previous temperature measurement techniques developed have exploited the heat transfer relationship between the gas and solid-phases of a two-phase flow (Abram et al., 2013; Basu, 1990; Chen et al., 2006; Collier et al., 2004; Parmar and Hayhurst, 2002). In these cases, the solid particles within the flows are either assumed to be small enough for their heat transfer processes to be modelled as a gas (i.e. the two-phase effects are essentially neglected) (Abram et al., 2013; Hasegawa et al., 2007; Jovicic et al., 2015), or the temperature of the particles is inferred from fundamental heat transfer equations (Katoshevski et al., 2001; Lin, 1999; Mograbi et al., 2002). However, while these equations are well established for idealised conditions, they do not take into account the more complex effects such as the 2-way and 4-way coupling regimes in turbulent flows, which include particle-fluid coupling, inter-particle interactions and particle clustering. They also become inaccurate for high heating rates of particles in the order of 10,000 °C/s in applications such as solar receivers (Piatkowski et al., 2011), combustion (Müller et al., 2017) and gasification, both from solar and auto-thermal conditions using oxygen (van Eyk et al., 2016). Additionally, the analysis of Rosner and Park (1988) showed that a high particle mass loading in a thermophoretically-modified aerosol particle transport system increases exponentially the boundary layer wall heat transfer coefficient. Although this analysis does not investigate the effect of particle mass loading on the solid-phase heat transfer, it provides further evidence that the influence of particle mass loading should not be neglected. Hence, there is a need to demonstrate a more reliable thermometry method to directly measure the temperature of suspended particles without influencing the gas-phase.

In recent decades, laser diagnostic measurement techniques have been developed to provide the in-situ and high-speed measurement of an increasing number of parameters with high temporal resolution (Abram et al., 2013; Fond et al., 2012; Kohse-Höinghaus et al., 2005). One such technique of particular relevance to the measurement of particle temperature is laser-induced phosphorescence (LIP), which utilises the temperature-dependent properties of thermophosphors (TPs) to measure the temperature

* Corresponding author at: School of Chemical Engineering, The University of Adelaide, SA 5005 Adelaide, Australia.
E-mail address: zeyad.alwahabi@adelaide.edu.au (Z.T. Alwahabi).

https://doi.org/10.1016/j.ijmultiphaseflow.2017.12.017
0301-9322/

Nomenclature

FOH	Fibre-optic head
LIP	Laser-induced phosphorescence
SNR	Signal-to-noise
SSSTS	Solid-state solar thermal simulator
TP	Thermophosphor
$\dot{Q}_{att}$	Attenuated power [W]
$\dot{Q}_{conv,c}$	Convective cooling power [W]
$\dot{Q}_{gain}$	Power absorbed [W]
$\dot{Q}_{in}$	Power input [W]
$\dot{Q}_{out}$	Power output [W]
$\dot{Q}_{rad,h}$	Radiative heating power [W]
$\dot{Q}_{rad,c}$	Radiative cooling power [W]
$\bar{T}$	Average temperature [°C]
A_p	Particle surface area [m^2]
A_s	Cross-sectional laser sheet area [m^2]
c_p	Specific heat capacity [J/K]
d_p	Particle diameter [m]
h	Heat transfer coefficient [W]/m^2K
I	Intensity [count]
$\frac{I_1}{I_2}$	Intensity ratio
m	Particle mass [g]
Nu	Nusselt number
P	Power [W]
T	Temperature [°C]
t	Time [s]
ΔT	Change in particle temperature with respect to room temperature [°C]
ε	Emissivity
λ	Wavelength [nm]
σ	Stephan-Boltzmann constant [W]/m^2K^4
χ	Attenuation
Φ	Heat flux [MW/m^2]

Subscripts

a	ambient
g	gas
p	particle

of particles. This technique requires an excitation source, such as laser radiation, to excite the TPs. Following excitation, the TPs emit phosphorescence, which is generated by the relaxation of electrons from the excited state to the ground state. The emission can then be collected using either an ICCD camera fitted with an image splitter, or with two ICCD cameras. An advantage of this technique is that phosphorescent materials have a lifetime close to the temporal resolution of typical intensified cameras (Charogiannis and Beyrau, 2013). This enables the maximum emission intensity to be collected during experiments. Furthermore, a large range of TPs that are available, each with their own operating temperature ranges and decay lifetimes (Aldén et al., 2011; Feist et al., 2003; Heyes et al., 2006). This offers the potential for a TP to be selected to match the expected temperature range on a case-by-case basis. Good accuracy can be anticipated given that errors in particle temperature measurements of between 5–10% have previously been reported in the previous studies of Abram et al. (2013) and Jovicic et al. (2015). However, the method is yet to be applied to resolve particle temperature in an environment in which the particles are at a significantly different temperature from that of the surrounding flow, notably in a system where the particles are simultaneously heated with a source of high flux radiation.

The present investigation employs a source of high-flux, well-characterised radiation at a wavelength of 910 nm that is absorbed only by the particle phase and not by the gas phase. Furthermore, the heat flux is sufficiently high for the difference between the particle temperature and the gas-phase temperature to be representative of conditions that occur in industrial systems. This is a challenge, given both the very short time-constants of small particles and the short residence times in turbulent flows [21, 24, 25]. The short residence time results from the need to use velocities of about 20 m/s or higher in a suspension flow to avoid particle fall-out. This is achieved with a solid-state radiation source, which has only recently become available with sufficient power and intensity. The solid-state system reported by Alwahabi et al. (2016) provides 3 kW of continuous radiation at fluxes of up to 30,000 kW/m^2. This laser generates the opportunity to establish a system that can provide in-situ measurements of temperature under conditions in which the heat transfer between the gas phase and particle phase is both well characterised and significant.

The aim of the present investigation is to demonstrate a direct, non-intrusive, temporally resolved, in-situ particle temperature measurement simultaneously with radiation attenuation. The combined measurement would be a key step towards fully understanding heat transfer in particle-laden flows. More specifically, we aim to demonstrate a temporally-resolved, volume-averaged application of LIP (that is, averaged over a measurement volume that is larger than an individual particle) with particles heated with well-controlled high flux radiation. This paper further aims to experimentally verify the relationship of gas and particle temperature, where a two-phase thermometry is performed simultaneously.

2. Theoretical approach

To select an appropriate thermophosphor (TP) for the current investigation, an estimate of the expected temperature rise was required. This was obtained with a simple first-order heat transfer model of heat transfer to a single moving particle subjected to radiative heating at high fluxes, using with in-house Matlab codes. The model considers: (1) radiative heating of the particle, (2) convective cooling between the particle and surrounding flow, (3) re-radiation, (4) heat gain within the particle. These heat transfer modes may be expressed with the following energy balance equation. The mentioned heat transfer modes may be expressed with the following energy balance equation:

$$\dot{Q}_{rad,h} = \dot{Q}_{conv,c} + \dot{Q}_{rad,c} + \dot{Q}_{gain} \tag{1}$$

where $\dot{Q}_{rad,h}$, $\dot{Q}_{conv,c}$, $\dot{Q}_{rad,c}$, and $\dot{Q}_{gain}$ are the radiative heating, convective and radiative losses, and particle heat gain respectively. Each of these processes can be expressed by the following equations:

Radiative heating:

$$\dot{Q}_{rad,h} = \varepsilon \frac{P}{A_s} A_p F_{12} \tag{2}$$

Convective cooling:

$$\dot{Q}_{conv,c} = hA_p(T_p - T_a) \tag{3}$$

Radiative cooling:

$$\dot{Q}_{rad,c} = \alpha\sigma A_p\left(T_p^4 - T_a^4\right) \tag{4}$$

Heat absorption:

$$\dot{Q}_{gain} = \dot{m}_P c_P \frac{d\left(T_{p,t} - T_{p,t-1}\right)}{dt} \tag{5}$$

where ε is the absorptivity specific to the particle material, $\frac{P}{A_s}$ is the energy flux from the radiative heat source (P is given by the power from the heat source, while A_s is the cross-sectional area of the heat source), $A_p = 4\pi r^2$ is the surface area of the particle

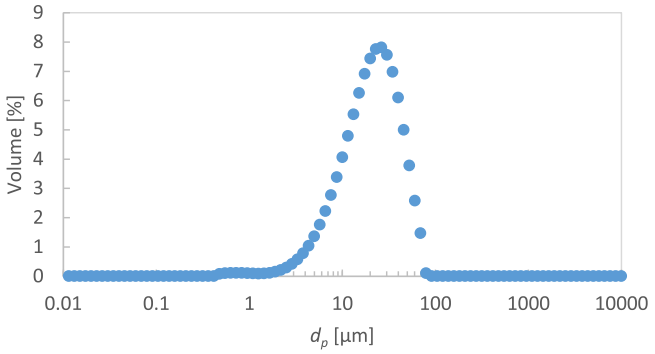

Fig. 1. The size distribution of the ZnO: Zn particles as measured with the Mastersizer 2000 (Malvern Instrument).

being heated, $F_{12} = 0.5$ is the view factor, $h = \frac{Nu}{d_p k}$ is the heat transfer coefficient, T_p is the particle temperature, T_a is the atmospheric temperature, α is the absorptivity, σ is the Stefan-Boltzmann constant, m is the mass of the particle, c_p is the specific heat capacity, t is time and ΔT is taken as $(T_{p,t} - T_{p,t-1})$. For the radiative cooling term (Eq. (4)), the particle surface area was used because the radiative cooling is transmitted in all directions from the particle. Parameters in this model were chosen to match as closely as possible to the experiment.

3. Experimental work

The experimental apparatus is comprised of three main sections - a fluidised bed with optical access to generate a turbulent flow of suspended particles, a controllable Solid-State Solar Thermal Simulator (SSSTS) (Alwahabi et al., 2016) and a laser-induced phosphorescence (LIP) system for temperature measurement.

3.1. Particle characterisation

From the theoretical model mentioned above, it was found that the expected temperature range of the present investigation would be < 627 °C. Hence, the ZnO: Zn thermophosphor was selected as the appropriate TP as it has the highest temperature sensitivity within the expected operating temperature (Aldén et al., 2011). Additionally, due to the expected short residence time of the particles in the heat source, the short decaying lifetime of ZnO: Zn is advantageous.

The ZnO: Zn TPs (Phosphor Technology) particles have a size distribution of 2 μm–50 μm, as shown in Fig. 1. During the investigation, it was found that the sole use of these TPs led to significant agglomeration and poor fluidisation, in line with the findings of Abram et al. (2015). As such, the ZnO: Zn TPs were mixed together with $CaSO_4{\cdot}2H_2O$ particles with a volume ratio of 4:1 within the fluidised bed. The size distribution of the $CaSO_4{\cdot}2H_2O$ particles is 100μm-200 μm. The larger $CaSO_4{\cdot}2H_2O$ particles promoted particle fluidisation by breaking up agglomerated particles of ZnO: Zn. However, only the ZnO: Zn TPs emit a phosphorescence signal when excited at the excitation wavelength of 355 nm and exhibits thermo-phosphorescent properties which allows for temperature measurements. Given the nature of the fluidised bed, the particles of different size tended to be fluidised at different heights, with the larger and heavier particles preferentially distributed toward the bottom of the bed and the smaller, lighter particles distributed towards the top.

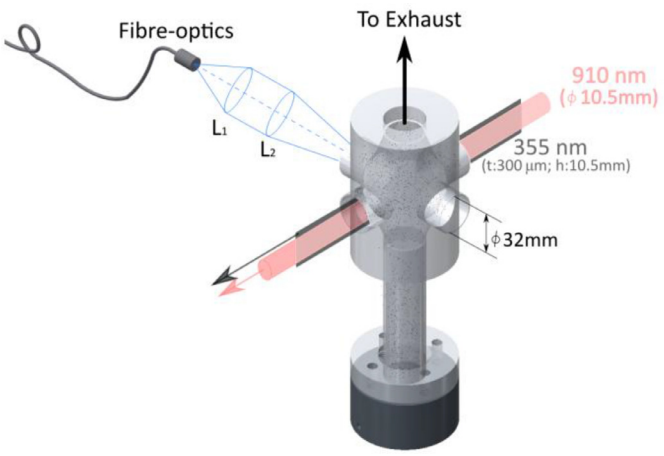

Fig. 2. The optically-accessible fluidised bed, with a fibre-optical coupled detector to collect the phosphorescence signal from particles. The ZnO:Zn particles are heated with a 910 nm wavelength Solid-State Solar Thermal Simulator (SSSTS) with a beam diameter of 10.5 mm and excited with a 355 nm Nd:YAG laser 300 μm thick and 10.5 mm high. Note: the 355 nm beam height is exaggerated for clarity. (For interpretation of the references to colour in this figure legend, the reader is referred to the web version of this article.)

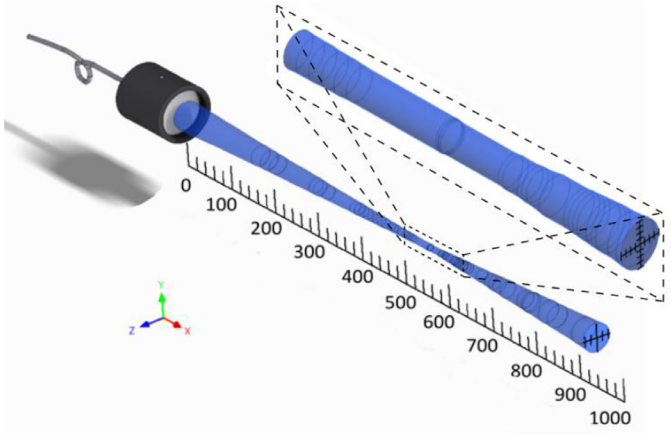

Fig. 3. Beam shape of Solid-state Solar Thermal Simulator (SSSTS) used to heat the particles, adapted from Alwahabi et al. (2016) with each tick indicating 10 mm. Insert: SSSTS beam waist of 10.5 mm ± 0.1 mm over the distance of 520 mm–540 mm from fibre-optical head. Ruler indicates 1 mm between each tick.

3.2. Optically-accessible fluidised bed

The flow of suspended particles was assessed in an optically-accessible fluidised bed as shown in Fig. 2. The fluidised bed has four 32 mm diameter circular apertures diametrically opposed, two allowing the laser beams to pass through the axis of the reactor and two to provide unrestricted optical access for the measurement systems. A layer of glass beads and a sintered plate were placed below the fluidised bed to generate a nominally uniform flow of the fluidising stream. A flow controller (Alicat Scientific, MC 20slpm) was used to maintain a constant airflow of 6.5 L/min to the fluidised bed via two inlets. Dry air was used to avoid humidity and minimise the propensity for particle agglomeration within the bed. The outlet from the top of the fluidised bed was connected to an exhaust line to remove any elutriated particles from the laboratory. Additionally, three *K*-Type thermocouples were placed in the fluidised system, one on the outer surface, one protruding inside the fluidised bed upstream of the heating zone, and one about 50 mm downstream from the heating zone to measure the overall rise in the gas-phase temperature. The three thermocouples were

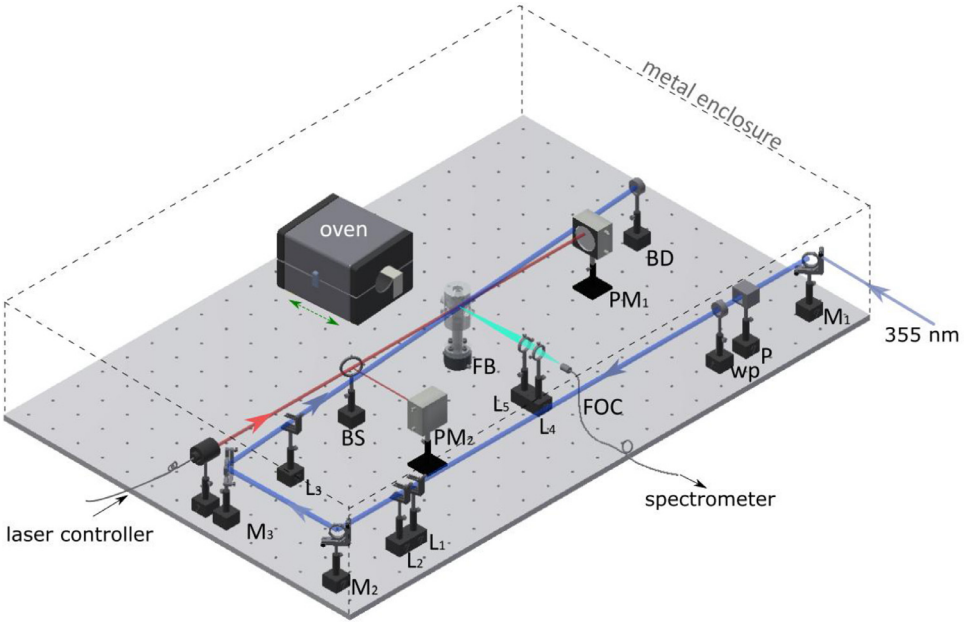

Fig. 4. The optical arrangement. Blue line: 355 nm Nd:YAG laser beam path; Red line: 910 nm SSSTS heating laser beam path; Cyan line: optical collection path of phosphorescence emission. Temperature-controllable oven replaces fluidised bed during calibration. BD: Beam Dump; BS: Beam Splitter; FOC: Fibre-optic Cable; L: Lens; M: Mirror; P: Polariser; PM: Power Meter; wp: waveplate. (For interpretation of the references to colour in this figure legend, the reader is referred to the web version of this article.)

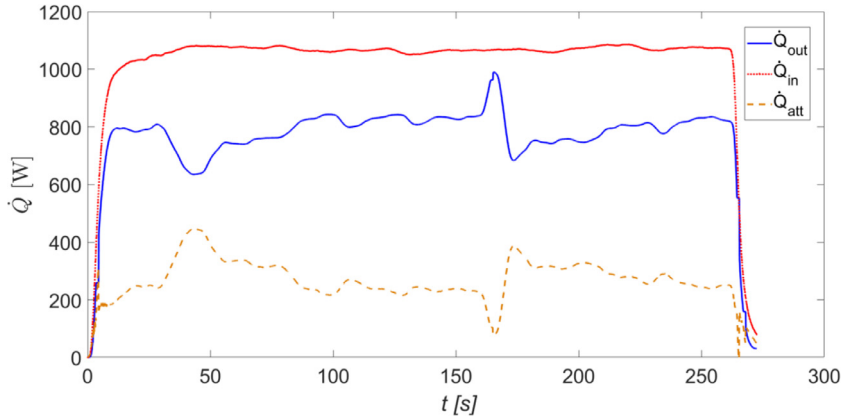

Fig. 5. Typical power measurements on the input, $\dot{Q}_{in}$, and output, $\dot{Q}_{out}$, sides of the fluidised bed system as well as attenuated power, $\dot{Q}_{att}$.

installed at an angle to the horizontal to prevent the settling of particles on top of the thermocouples. The first of the thermocouples was used to monitor the overall temperature of the fluidised bed to ensure the experiment was performed in a safe environment. (Note that the experiment heats only a small fraction of the total bed so that the overall temperature rise is typically in the order of 30°–80 °C).

3.3. Solid-State solar thermal simulator (SSSTS)

The SSSTS generates irradiation with a Gaussian profile (Alwahabi et al., 2016) that converges from a diameter of 46 mm at the fibre-optic head (FOH) to a waist of 10.5 mm ± 0.1 mm diameter over the distance of 520 mm–540 mm from the FOH, as shown in Fig. 3. The SSSTS operates at a peak wavelength of 910 nm (red beam shown in Fig. 2), which is absorbed by the particles but not by the air. Importantly, the beam profile of the SSSTS is well-defined, both in the focal plane and on either side, allowing ray tracing to be undertaken reliably. These beam characteristics allow the irradiation flux and beam size in the working section to be varied by varying its position relative to that of the focal plane. However, the experiment was conducted within the 20 mm length beam waist to ensure constant heating rate throughout the working section. Since the SSSTS controller can be used to regulate its electrical input power, this was used as the preferred method to control heat flux. Additionally, a UV silica plate was placed 300 mm away from the front of the Fibre-optic Head (FOH) of the SSTS laser to split the laser beam into a 92:8 ratio. Both beams were directed to water-cooled power meters (Gentec model HP100A-4KW-HE) that acted as beam dumps, while also providing in-situ laser power measurements at a sample frequency of 10 Hz. A K-type thermocouple was also mounted to the outer surface of the FOH to ensure its temperature does not exceed 40 °C.

3.4. Optical arrangement

The optical arrangement for the experiment is presented in Fig. 4. The third harmonic of the Nd: YAG (Quantel Q-smart 850) laser operated at 5.27 ± 0.47 mJ and 355 nm is directed into the fluidised bed chamber to excite the ZnO: Zn thermophosphors (TPs). A three-lens bundle was used to form an excitation laser sheet of 300 µm thickness and 10.5 mm height. The path of

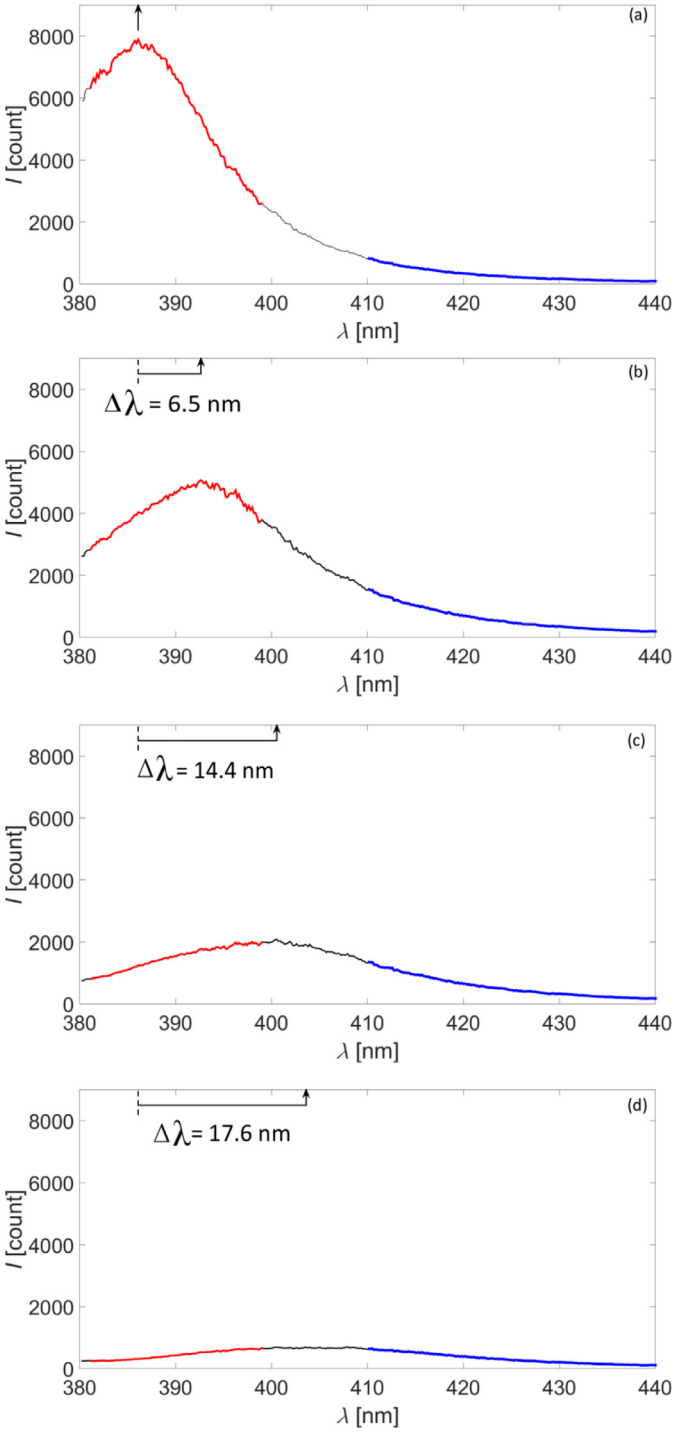

Fig. 6. Four ZnO:Zn spectra emission as a function of the collection wavelength at: (a) 35 °C, (b) 103 °C, (c) 207 °C and (d) 300 °C. The arrow indicates the shift in peak wavelength, Δλ, relative to that at 35 °C. Intensity ratios are calculated by taking sum of those collected over the range 381 nm – 399 nm (red line) relative to those collected over the range 410 nm – 440 nm (blue line). (For interpretation of the references to colour in this figure legend, the reader is referred to the web version of this article.)

the Nd: YAG laser was offset from the SSSTS beam path by 7° such that they intercept on the axis of the 10.5 mm waist of the SSSTS beam and at the centre of the fluidised bed, as shown in Fig. 2. A spectrometer (Princeton Instruments-Acton Series Spectrograph) utilising a 600 groove per mm grating was used to collect the phosphorescence emission signals through a two-lens light-collecting channel, directed to a round-to-linear fibre bundle (Thorlabs, BFL200HS02). This signal was collected through focusing optics (Fig. 2) from an effective "probe volume" with an estimated diameter of 32 mm, which is larger than the width of the laser sheet. That is, the total volume of the measurement probe was 9.6mm^3, although no signal is generated from the region upstream from the Nd: YAG laser. Hence, the probe is much larger than the individual particles and the signal is averaged from all particles in this volume for each measurement. The resolved spectra were then recorded using an ICCD camera (Princeton Instruments-Max4) at 1.67 Hz. For safety, the entire system was placed within metal enclosure with safety interlocks so that it cannot be operated unless the system is fully enclosed, while various temperatures in the system are monitored at all times with a K-type thermocouple mounted to the enclosure. The temperatures of all five thermocouples (including the ones mounted in the fluidised bed and SSSTS systems) were monitored with a digital-to-analogue converter and recorded to a computer at a rate of 0.0167 Hz. Alarm limits were set for each thermocouple (in the range 40–100 °C) to allow time for the experiments to be stopped in the event of an alarm. The calibration experiments matched the optical and experimental arrangement of the main experiment, except that a ZnO: Zn TP coated flat plate heated by an oven (MTI Corporation, OTF-1200X-S) was used instead of a fluidised bed. Here, the flat plate was placed normal to the Nd: YAG laser path, and the phosphorescence emission signal was collected similar to the main experiment. Additionally, a *K*-type thermocouple was attached to the front of the flat plate to measure directly the temperatures of the TPs during the calibration.

3.5. Methodology

3.5.1. Temperature calibration

The calibration was performed at 45 different temperatures ranging from 23 °C and 425 °C. At each temperature, the thermophosphor-coated plate was allowed to reach thermal equilibrium, as measured by the attached thermocouple, before 400 single-shot phosphorescence spectra were collected. From each measured spectra, the ratio of intensity of each signal, $\frac{I_1}{I_2}$, was calculated using:

$$\frac{I_1}{I_2} = \frac{\sum_{\lambda=410}^{440} I_\lambda}{\sum_{\lambda=381}^{399} I_\lambda} \tag{6}$$

where $\sum_{\lambda=410}^{440} I_\lambda$ and $\sum_{\lambda=381}^{399} I_\lambda$ are the sum of intensity emissions taken at wavelengths 410 nm–440 nm (plotted by the blue line of Fig. 6) and 381 nm–399 nm (plotted by the red line of Fig. 6) respectively. These intensity bands were chosen from the commercially available filter bandwidths to provide the maximum intensity ratio without compromising spectral resolution. Additionally, an investigation of the influence of laser fluence of the excitation (355 nm) laser on $\frac{I_1}{I_2}$ revealed that $\frac{I_1}{I_2}$ varies by approximately 25% between laser fluence values of 2.6 mJ/cm^2 and 5.17 mJ/cm^2. To correct for this influence, a method proposed by Abram et al. (2015) whereby all values of $\frac{I_1}{I_2}$ are normalised by the $\frac{I_1}{I_2}$ recorded at room temperature, $(\frac{I_1}{I_2})_{ref}$, was utilised. The resulting $(\frac{I_1}{I_2})/(\frac{I_1}{I_2})_{ref}$ were then plotted against each temperature to obtain a calibration curve from which particle temperatures can be inferred.

3.5.2. Particle mass loading measurement

Besides particle temperature measurements, another parameter that is important in the present investigation is the particle mass loading, which varies with time despite the constant fluidising velocity. The influence of mass loading was determined by comparing the two power meter readings to calculate the attenuated power of

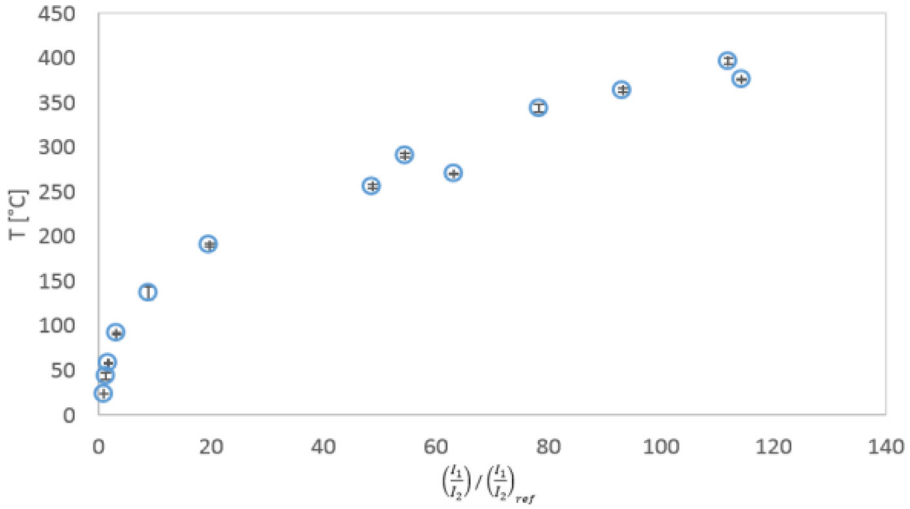

Fig. 7. Calibration curve showing relationship between the measured ZnO:Zn temperature, T and the intensity ratio with respect to a reference intensity ratio $(\frac{I_1}{I_2})/(\frac{I_1}{I_2})_{ref}$, calculated by taking the ratio of intensity emissions collected at wavelengths 410nm-440 nm and 381 nm–399 nm respectively.

the SSSTS beam, $\dot{Q}_{att}$, by the particles:

$$\dot{Q}_{att} = \dot{Q}_{in} - \dot{Q}_{out}. \quad (7)$$

here, $\dot{Q}_{in}$ is the power input as measured by the power meter before the fluidised bed, and $\dot{Q}_{out}$ is the power output as measured by the one after. Given the measurements from the two power meters were split in a 92:8 ratio, $\dot{Q}_{in}$ and $\dot{Q}_{out}$ were obtained by multiplying each by $\frac{100}{92}$ and 12.5 respectively. In this way, $\dot{Q}_{att}$ is directly dependent to the particle mass loading. Fig. 5 presents a typical time-series of power measurements with the two power meters recorded over approximately 2500 shots at 10 Hz and $\Phi = 12.4$ MW/m^2. As can be seen, $\dot{Q}_{att}$ was not constant throughout the time-series, indicating large-scale unsteadiness in the fluidised bed. The number of particles within the field of view can subsequently be estimated by comparing Eqs. (7) and (5):

$$\dot{Q}_{att} = \sum_{i=1}^{N_p} \dot{m}_{P,i} c_{P,i} \Delta T_i \quad (8)$$

3.5.3. Real-time single-shot area-averaged particle temperature measurement

To demonstrate the technique on radiatively heated moving particles in real-time, 14 sets of measurements were taken in the range of 2.4 MW/m$^2 \leq \Phi \leq$ 21.1 MW/m^2. For each of these measurements, the first 50 (≈30 s) and last 100 (≈60 s) of the 800 total shots were recorded with the SSSTS switched off. After each measurement, and before the next, the particles in the fluidised bed were replenished and the system was allowed to cool to room temperature. Recorded phosphorescence emissions were then processed with in-house Matlab codes to calculate $\frac{I_1}{I_2}$ and subsequently infer particle temperatures.

4. Results and discussion

4.1. Temperature calibration

Fig. 6 presents examples of the phosphorescence spectra relative to wavelength at $T = 35$ °C, 103 °C, 203 °C and 300 °C. Here, all exhibit the same trends, i.e., a clear right shift in the peak wavelength position, $\Delta\lambda$, with increased temperature. This demonstrates the sensitivity of ZnO: Zn emission spectrum to temperature within the recorded temperature range. As it can be seen, the phosphorescence emission decreases with temperature, consistent with findings from Abram et al. (2013). However, this has no consequence on the ratio, $\frac{I_1}{I_2}$, used to relate the phosphorescence to temperature, as both I_1 and I_2 are of the same scale at any given temperature. Additionally, this influence is further mitigated by comparing it to a reference intensity ratio, $(\frac{I_1}{I_2})/(\frac{I_1}{I_2})_{ref}$, as mentioned in Section 3.5.1.

Fig. 7 presents the calibration of $(\frac{I_1}{I_2})/(\frac{I_1}{I_2})_{ref}$as a function of the measured ZnO: Zn T, which was obtained from the calibration process. It can be seen that $(\frac{I_1}{I_2})/(\frac{I_1}{I_2})_{ref}$ increases with temperature, where the relationship can be described by $T = 92.89 \ln\left(\frac{(\frac{I_1}{I_2})}{(\frac{I_1}{I_2})_{ref}}\right) + 28.2$, while the scatter in the data reveals that these measurements are accurate to within 3%−12%, which is consistent with the accuracy found in previous similar investigations (Abram et al., 2013; Sarner et al., 2008).

4.2. Real-time single-shot area-averaged particle temperature measurement

Fig. 8 presents the time-history of the SSSTS being switched off (Fig. 8a1), on at $\Phi = 12.4$ MW/m^2 (Fig. 8a2), off again (Fig. 8a3), single-shot temperature measurements of ZnO: Zn particles, T_p, (Fig. 8b1–b3), averaged T_p at every 5 measurements with a fitted curve plotted in red, $\overline{T_p}$, (Fig. 8c1–c3) and $\dot{Q}_{att}$ (Fig. 8d1–d3). Here, the cases labelled b1, c1, and d1 are related to measurements taken when the SSSTS is switched off, while b2, c2, d2 are related to when it was switched on, and b3, c3, d3 are related to when it was switched off again (i.e., cooling). It can be seen from Fig. 8(b2) and (c2) that while heating effects were immediately observed when the SSSTS was switched on, where some T_p approaches approximately 350 °C, the particle temperature rise with respect to room temperature, ΔT_p is typically 50 °C - 150 °C when SSSTS is turned on. To determine the local heating rate of the particles within the irradiated zone, several 2D images were taken with an ICCD camera (Princeton Instruments – PI-MAX) aligned normal to the laser sheet, with the exposure time set to 3 ms. The length of each particle travel path recorded was then divided by the 3 ms exposure time to obtain an average velocity of 0.21 m/s. On this basis, given the path length through the heating zone of 10.5 mm, the average residence time was 0.035 s, with the maximum value of 0.05 s. Dividing the maximum temperature rise, ΔT_{max}, by the residence time, the local heating rate has an average and maximum value of

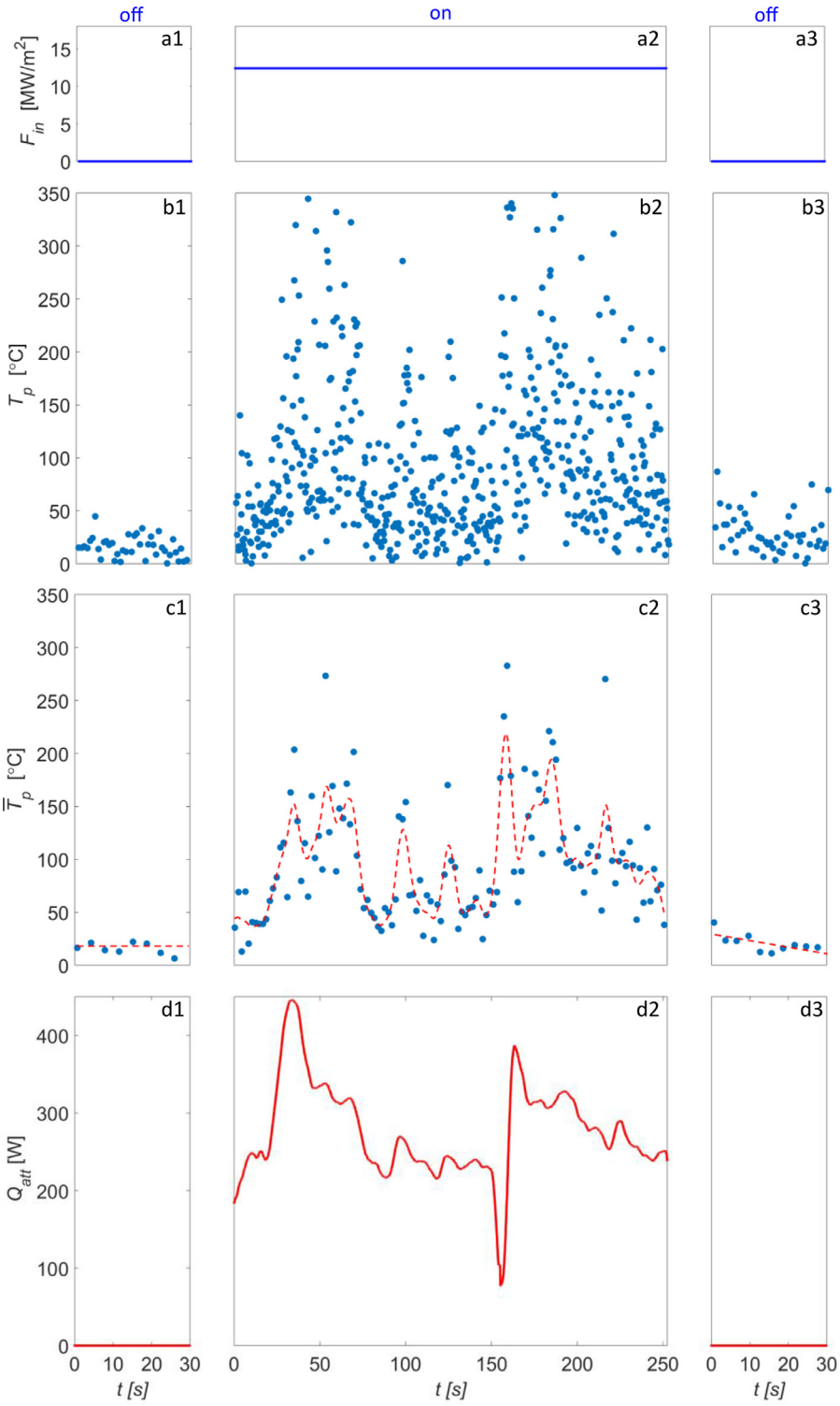

Fig. 8. Time-series measurements over ≈5 mins for which (a) first ≈30 s were with the SSSTS switched off, the next ≈250 s with it switched on at $\Phi = 12.4$ MW/m^2 and ≈30 s shots with it switched off, (b) scatter plots of single-shot measurements of particle temperature rise, with the fitted curve in red, (c) mean particle temperature measurement averaged at every 5 measurements, (d) the attenuated power of the SSSTS beam by the ZnO:Zn particles. (For interpretation of the references to colour in this figure legend, the reader is referred to the web version of this article.)

23,000 °C/s and 33,000 °C/s respectively, for an irradiation flux of $\Phi = 18.72$ MW/m^2.

Cooling effects can be observed from Fig. 8(c3), where T_p is seen to decrease linearly with time after the heating laser is switched off. This cooling can be expressed by:

$$\Delta T_p = -0.89t. \quad (9)$$

Significant scatter can be observed in the single-shot temperature measurements in Fig. 8(b2). This fluctuation in T_p is attributed to the unsteadiness of the particle mass loading, consistent with the fluctuations in the measured values of $\dot{Q}_{att}$ recorded in Fig. 8(d2), which ranged between 80 W and 450 W.

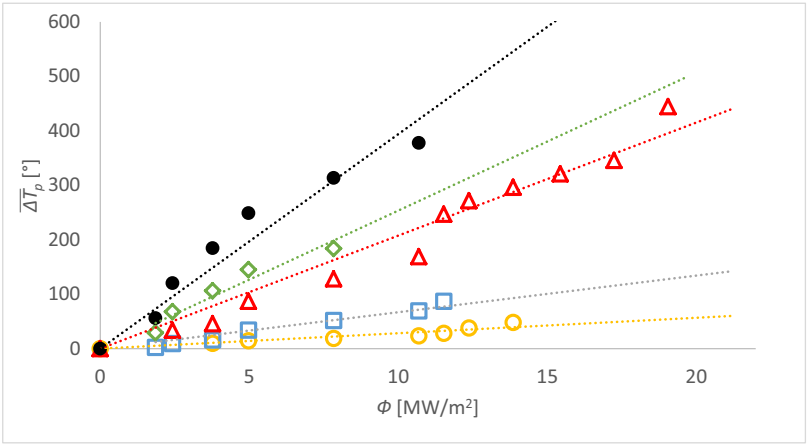

Fig. 9. Dependence of particle temperature rise with respect to irradiation fluxes and attenuation (or particle mass loading). χ: ○ 20% □ 30% △ 40% ◇ 60% ● 70%.

A large amount of scatter is observed in the single-shot temperature measurements in Fig. 8(b2). This fluctuation in T_p is attributed to the unsteadiness of the particle mass loading, consistent with the fluctuations in the measured values of $\dot{Q}_{att}$ recorded in Fig. 8(d2), which ranged between 80 W and 450 W.

The temperature of a single particle is determined from an energy balance that depends on particle diameter, absorptance, heating rate, initial particle temperature and temperature of the surrounding medium. Since the radiation flux is constant for a given experimental run, the strong dependence of $\dot{Q}_{att}$ on T_p implies that the temperature of the surrounding fluidising medium varies with local fluctuations in mass loading. Given the strong inter-particle heat transfer in a fluidised bed, these fluctuations are transferred to the surrounding medium.

To isolate the effects of mass loading, the attenuated power by the particles, χ was calculated from the ratio: $\chi = 1 - \frac{\dot{Q}_{out}}{\dot{Q}_{in}}$ for each irradiation flux, Φ cases. The calculated χ and measured ΔT_p were then sorted and paired from high to low. The pairs were subsequently sorted into 7 bins from 10%–70% and compared against Φ. Fig. 9 presents the dependence of $\Delta\overline{T_p}$ on Φ for various values of χ. Consistent trends can be seen, with a linear relationship between temperature and flux for a given value of attenuation. This provides confidence in the measurement. Furthermore, the temperature increases with the attenuation. For example, for $\Phi = 7.8$ MW/m^2, a value of $\chi = 60\%$ is required to achieve a $\Delta\overline{T_p}$ of ~183 °C, while for a $\Delta\overline{T_p}$ of ~377 °C, a χ of 70% is required. This indicates that χ highly influences $\Delta\overline{T_p}$ and the relationship between $\Delta\overline{T_p}$ and Φ can be expressed as follows:

$$\Delta\overline{T_p}(\Phi) = K\Phi. \tag{10}$$

where K [m^{2}K/MW] is a constant related to χ. Here, the linear relationship between temperature difference and heat flux is due to the theoretical expectation presented in Eq. (2).

The relationship of the empirical constant, K, as a function of χ was presented in Fig. 10 and a least-square fitting was used to describe this relationship:

$$K = 1.31e^{4.8\chi} \tag{11}$$

This results in an expression for $\Delta\overline{T_p}$ that can be described by:

$$\Delta\overline{T_p}(\Phi, \chi) = \left(1.31e^{4.8\chi}\right)\Phi \tag{12}$$

This expression fits the data points with an accuracy of approximately 98% for attenuation of 10–30% and 60–70%, although it is approximately 60% for attenuation of 40%. This agreement provides important confirmation that the measurements are internally

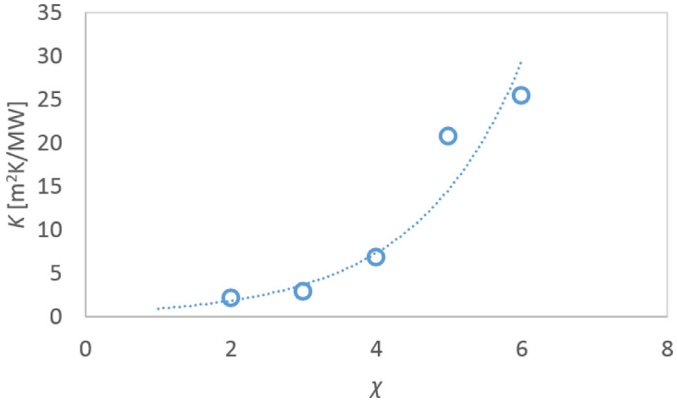

Fig. 10. Dependence of constant K from Eq. (9) on attenuation, χ, with a line fitted through it.

self-consistent, which provides further confidence in the measurement. Additionally, it corresponds to the theoretical expectations described in Section 2. Nevertheless, it should be noted that the current equation is entirely empirical, so that the constants have no general significance.

Although a decrease in phosphorescence signal was observed with increased temperature from Fig. 6, this is in line with the findings of Abram et al. (2015), good signal levels were still detected as presented in Fig. 11. The signal-to-noise ratio was evaluated for the fluidised particle cases for which the peak signal from the TP emission was the strongest and weakest, i.e. for at T = 30 °C and 352 °C, respectively. These measured spectra are presented in Fig. 11(a) and (b), where it should be noted that the scale in Fig. 11(b) is 95 times smaller than that in (a). For the T = 30 °C case, where the signal is greatest, the noise is negligible. For the case where the signal is the weakest (Fig. 11(b)), the resulting signal-to-noise ratio (SNR) is 22.8. It should be noted that although the signal appears different from the spectra emissions presented in Fig. 6, the calibration curve is still applicable since it depends only on $(\frac{I_1}{I_2})/(\frac{I_1}{I_2})_{ref}$, as mentioned in Section 3.5.1.

Fig. 12 presents the variation in the mean values of both particle temperature, $\Delta\overline{T_p}$, and the gas temperature at the outlet of the reactor, $\Delta\overline{T_g}$, averaged over the 250 s when the SSSTS was switched on, as a function of the Φ. It can be seen that despite the fluctuations in shot-to-shot measurements of $\Delta\overline{T_p}$ shown in Fig. 8, the mean values exhibit a clear trend that is consistent with expectation. Furthermore, the gas phase temperature scales with the particle temperature at a value of approximately half the magnitude

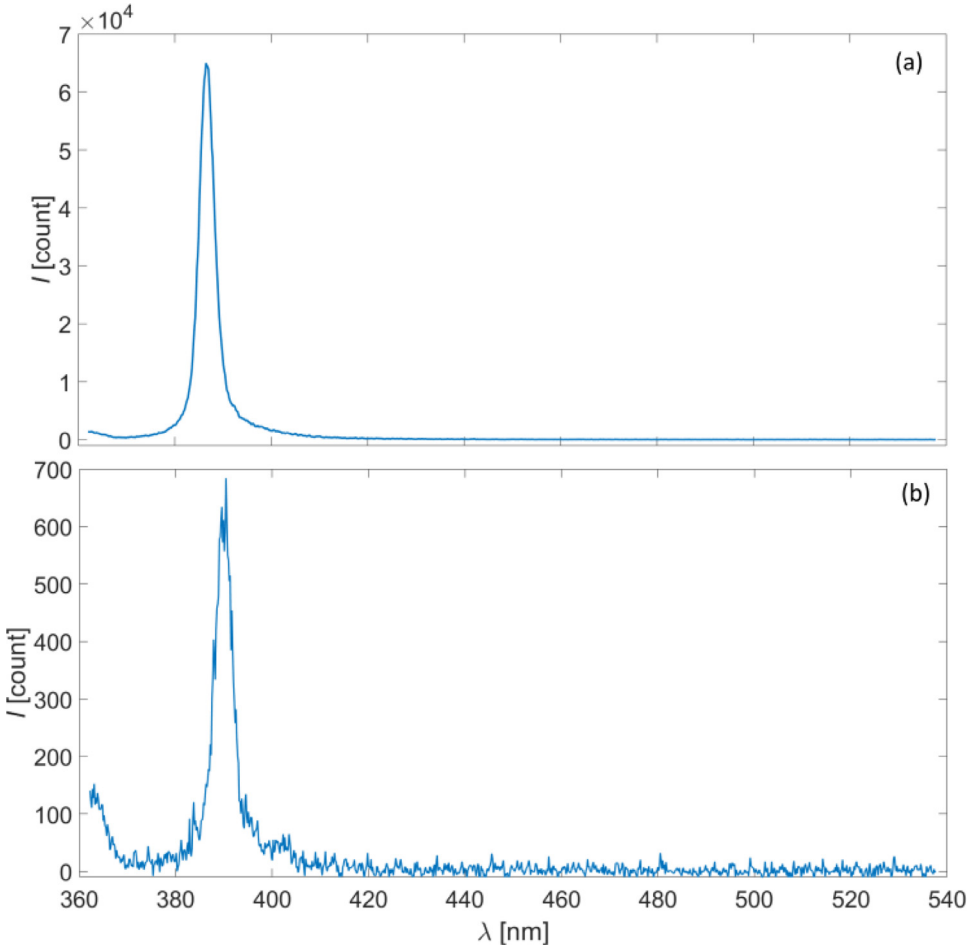

Fig. 11. Typical spectrum signal and signal-to-noise ratio of ZnO:Zn excited at 355 nm. (a) Strongest signal strength before signal reaches saturation; (b) Typical weak signal presented approximately 100 times its signal strength.

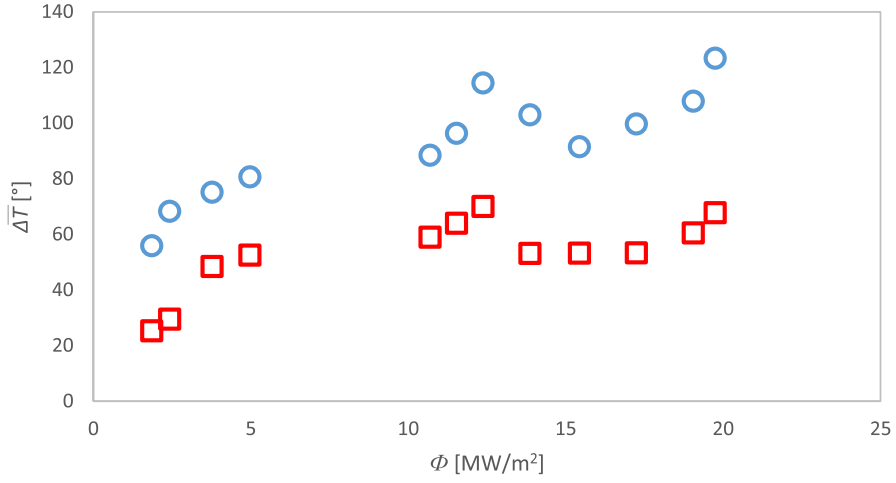

Fig. 12. Effect of irradiation fluxes, Φ, on the average measured particle temperatures, $\bar{T}_p$ (circle) and averaged measured gas temperatures, $\bar{T}_g$, (square) over 650 instantaneous shots where the particles are radiatively heated.

(noting the different scale for the two parameters in the figure) implying a relationship that is close to one of proportionality.

It is important to note that the gas phase temperature is measured 50 mm downstream from the position at which the particles are measured. Hence, this gives time for the heat to be transferred from the particle phase to the gas. This is not intended to provide a local measurement of the heat transfer rate, but rather to give further confidence in the reliability of the measurements.

5. Conclusion

Temperature measurements of irradiated particles in a fluidised bed have been demonstrated using laser-induced phosphorescence (LIP). Uniform and high radiation flux, up to 20,000, suns was supplied by a newly developed solid-state solar thermal simulator. It was found that the mass loading, in addition to the irradiation flux, has a major impact on the particle's temperatures. A relationship between the particle temperature, attenuated power, and irradiation flux has been developed. Furthermore, the relationship between particle and gas temperature has been found. The maximum particle temperature was 465.8 °C recorded at radiation flux of 18.72 MW/m^2 and 40% radiation attenuation. Furthermore, it was found, on average, the measured gas temperature is 44 °C lower than the measured particle temperature. Furthermore, the method is applicable to planar imaging and therefore has potential to be employed together with other diagnostics methods, such as a particle image velocimetry.

Acknowledgement

We gratefully acknowledge support from the Australian Research Council through its Discovery grant 150102230 and Linkage Grant LE130100127.

The authors would also like to thank Mr Jeffrey Hiorns and Mr Jason Peak, from the mechanical workshop at the School of Chemical Engineering, for his outstanding technical support. The financial support from the Institute or Mineral and Energy Resource (IMER) and the Faculty of Engineering, Computer & Mathematical Science (ECMS) at The University of Adelaide is acknowledged.

References

Abram, C., Fond, B., Beyrau, F., 2015. High-precision flow temperature imaging using ZnO thermographic phosphor tracer particles. Opt. Express 23, 19453–19468.

Abram, C., Fond, B., Heyes, A.L., Beyrau, F., 2013. High-speed planar thermometry and velocimetry using thermographic phosphor particles. Appl. Phys. B 111, 155–160.

Aldén, M., Omrane, A., Richter, M., Sarner, G., 2011. Thermographic phosphors for thermometry: a survey of combustion applications. Prog. Energy Combust. Sci. 37, 422–461.

Alwahabi, Z.T., Kueh, K.C.Y., Nathan, G.J., Cannon, S., 2016. Novel solid-state solar thermal simulator supplying 30,000 suns by a fibre optical probe. Opt. Express 24, A1444–A1453.

Basu, P., 1990. Heat transfer in high temperature fast fluidized beds. Chem. Eng. Sci. 45, 3123–3136.

Charogiannis, A., Beyrau, F., 2013. Laser induced phosphorescence imaging for the investigation of evaporating liquid flows. Exp. Fluids 54, 1–15.

Chen, H., Chen, Y., Hsieh, H.-T., Siegel, N., 2006. Computational fluid dynamics modeling of gas-particle flow within a solid-particle solar receiver. J. Solar Energy Eng. 129, 160–170.

Collier, A.P., Hayhurst, A.N., Richardson, J.L., Scott, S.A., 2004. The heat transfer coefficient between a particle and a bed (packed or fluidised) of much larger particles. Chem. Eng. Sci. 59, 4613–4620.

Feist, J.P., Heyes, A.L., Seefeldt, S., 2003. Oxygen quenching of phosphorescence from thermographic phosphors. Measure. Sci. Technol. 14, N17–N20.

Fond, B., Abram, C., Heyes, A.L., Kempf, A.M., Beyrau, F., 2012. Simultaneous temperature,mixture fraction and velocity imaging in turbulent flows using thermographic phosphor tracer particles. Opt. Express 20, 22118–22133.

Hasegawa, R., Sakata, I., Yanagihara, H., Johansson, B., Omrane, A., Aldén, M., 2007. Two-dimensional gas-phase temperature measurements using phosphor thermometry. Appl. Phys. B 88, 291–296.

Heyes, A.L., Seefeldt, S., Feist, J.P., 2006. Two-colour phosphor thermometry for surface temperature measurement. In: Colour and Design in the Natural and Man–Made Worlds. Elsevier Ltd, pp. 257–265.

Jovicic, G., Zigan, L., Will, S., Leipertz, A., 2015. Phosphor thermometry in turbulent hot gas flows applying Dy:YAG and Dy:Er:YAG particles. Measure. Sci. Technol. 26.

Katoshevski, D., Zhao, B., Ziskind, G., Bar-Ziv, E., 2001. Experimental study of the drag force acting on a heated particle. J. Aerosol Sci. 32, 73–86.

Kohse-Höinghaus, K., Barlow, R.S., Aldén, M., Wolfrum, J., 2005. Combustion at the focus: laser diagnostics and control. Proc. Combust. Inst. 30, 89–123.

Lin, J., 1999. Temperature analysis of the powder streams in coaxial laser cladding. Opt. Laser Technol. 31, 565–570.

Mograbi, E., Ziskind, G., Katoshevski, D., Bar-Ziv, E., 2002. Experimental study of the forces associated with mixed convection from a heated sphere at small Reynolds and Grashof numbers. Part II: assisting and opposing flows. Int. J. Heat Mass Transfer 45, 2423–2430.

Müller, F., Poživil, P., van Eyk, P.J., Villarrazo, A., Haueter, P., Wieckert, C., Nathan, G.J., Steinfeld, A., 2017. A pressurized high-flux solar reactor for the efficient thermochemical gasification of carbonaceous feedstock. Fuel 193, 432–443.

Parmar, M.S., Hayhurst, A.N., 2002. The heat transfer coefficient for a freely moving sphere in a bubbling fluidised bed. Chem. Eng. Sci. 57, 3485–3494.

Piatkowski, N., Wieckert, C., Weimer, A.W., Steinfeld, A., 2011. Solar-driven gasification of carbonaceous feedstock-a review. Energy Environ. Sci. 4, 73–82.

Rosner, D.E., Park, H.M., 1988. Thermophoretically augmented mass-, momentum- and energy-transfer rates in high particle mass loaded laminar forced convection systems. Chem. Eng. Sci. 43, 2689–2704.

Sarner, G., Richter, M., Aldén, M., 2008. Investigations of blue emitting phosphors for thermometry. Measure. Sci. Technol. 19.

van Eyk, P.J., Ashman, P.J., Nathan, G.J., 2016. Effect of high-flux solar irradiation on the gasification of coal in a hybrid entrained-flow reactor. Energy Fuels 30, 5138–5147.

Chapter 6:

Single-shot Planar Temperature Imaging of Radiatively-heated Fluidized Particles

Statement of Authorship

Title of Paper	Single-shot planar temperature imaging of radiatively heated fluidized particles
Publication Status	☑ Published ☐ Accepted for Publication ☐ Submitted for Publication ☐ Unpublished and Unsubmitted work written in manuscript style
Publication Details	K.C.Y. Kueh, T.C.W. Lau, G.J. Nathan, Z.T. Alwahabi, Single-shot planar temperature imaging of radiatively heated fluidized particles, Optics Express, 25 (2017) 28764-28775.

Principal Author

Name of Principal Author (Candidate)	Kimberley C.Y. Kueh		
Contribution to the Paper	Set up experimental arrangements, performed experiment, process and analyse results. Took primary responsibility of writing the paper and responding to the reviewers.		
Overall percentage (%)	60		
Certification:	This paper reports on original research I conducted during the period of my Higher Degree by Research candidature and is not subject to any obligations or contractual agreements with a third party that would constrain its inclusion in this thesis. I am the primary author of this paper.		
Signature		Date	23/08/2019

Co-Author Contributions

By signing the Statement of Authorship, each author certifies that:

i. the candidate's stated contribution to the publication is accurate (as detailed above);

ii. permission is granted for the candidate in include the publication in the thesis; and

iii. the sum of all co-author contributions is equal to 100% less the candidate's stated contribution.

Name of Co-Author	Timothy C.W. Lau		
Contribution to the Paper	Assisted in the processing of experimental results and editing of manuscript.		
Signature		Date	28/08/2019

Name of Co-Author	Graham J. Nathan		
Contribution to the Paper	Supervised the analysis of experimental results and assisted with editing the manuscript.		
Signature		Date	26/8/2019

Name of Co-Author	Zeyad T. Alwahabi		
Contribution to the Paper	Supervised the experimental campaigns and processing of results. Assisted with editing the manuscript.		
Signature		Date	

Research Article | Vol. 25, No. 23 | 13 Nov 2017 | OPTICS EXPRESS 28764
Optics EXPRESS

Single-shot planar temperature imaging of radiatively heated fluidized particles

KIMBERLEY C.Y. KUEH,[1,3] TIMOTHY C.W. LAU,[1,3] GRAHAM J. NATHAN,[1,3] AND ZEYAD T. ALWAHABI[2,3,*]

[1]School of Mechanical Engineering, The University of Adelaide, SA 5005 Adelaide, Australia
[2]School of Chemical Engineering, The University of Adelaide, SA 5005 Adelaide, Australia
[3]Centre of Energy Technology, The University of Adelaide, SA 5005 Adelaide, Australia
*zeyad.alwahabi.@adelaide.edu.au

Abstract: A single-shot, non-intrusive planar technique for measuring the temperature of radiatively heated particles with good spatial resolution has been demonstrated. This technique has been applied to particles with diameters between 10µm and 50µm, suspended in a highly unsteady flow within a fluidized bed. The particles were heated with a high-flux radiation source to provide high and well-characterized heat fluxes ranging from 2.4 MW/m^2 ≤ Φ ≤ 21.1 MW/m^2. Each measurement is derived from two images with an area of 15mm × 10.8mm using an image splitter and a single ICCD camera. An average of 30 particles were recorded in each image with a spatial resolution of 51 pixels/mm. A maximum temperature rise of 350°C was recorded with a heat flux of 21.1 MW/m^2, with a corresponding heating rate of up to 23,000°C/s, given the maximum residence time of the particles in the heating region of 0.05s. The normalized temperature distribution within an individual particle agglomerate was found to be up to ± 4%, which is attributable to ICCD noise so that the mean temperature is well resolved.

OCIS codes: (110.0110) Imaging systems; (120.0120) Instrumentation, measurement, and metrology.

References and links

1. A. C. Eckbreth, *Laser Diagnostics for Combustion Temperature and Species*, 1st ed. (Combustion Science and Technology, 1996).
2. C. Abram, B. Fond, A. L. Heyes, and F. Beyrau, "High-speed planar thermometry and velocimetry using thermographic phosphor particles," Appl. Phys. B **111**, 155–160 (2013).
3. C. Abram, B. Fond, and F. Beyrau, "High-precision flow temperature imaging using ZnO thermographic phosphor tracer particles," Opt. Express **23**(15), 19453–19468 (2015).
4. F. Müller, P. Poživil, P. J. van Eyk, A. Villarrazo, P. Haueter, C. Wieckert, G. J. Nathan, and A. Steinfeld, "A pressurized high-flux solar reactor for the efficient thermochemical gasification of carbonaceous feedstock," Fuel **193**, 432–443 (2017).
5. G. Bizarri and B. Moine, "On BaMgAl10O17: Eu2+ phosphor degradation mechanism: Thermal treatment effects," J. Lumin. **113**, 199–213 (2005).
6. G. Jovicic, L. Zigan, S. Will, and A. Leipertz, "Phosphor thermometry in turbulent hot gas flows applying Dy:YAG and Dy:Er:YAG particles," Meas. Sci. Technol. **26**, 015204 (2015).
7. G. Särner, M. Richter, and M. Aldén, "Investigations of blue emitting phosphors for thermometry," Meas. Sci. Technol. **19**, 125304 (2008).
8. H. Chen, Y. Chen, H.-T. Hsieh, and N. Siegel, "Computational Fluid Dynamics Modeling of Gas-Particle Flow Within a Solid-Particle Solar Receiver," J. Sol. Energy Eng. **129**, 160–170 (2006).
9. J. Brubach, A. Dreizler, and J. Janicka, "Gas compositional and pressure effects on thermographic phosphor thermometry," Meas. Sci. Technol. **18**, 764–770 (2007).
10. J. P. Feist, A. L. Heyes, and S. Seefeldt, "Oxygen quenching of phosphorescence from thermographic phosphors," Meas. Sci. Technol. **14**(17–N), 20 (2003).
11. J. P. Holman, *Heat Transfer*, 10th ed. (McGraw Hill Book Company, 1986).
12. K. F. Cai, E. Müller, C. Drašar, and A. Mrotzek, "Preparation and thermoelectric properties of Al-doped ZnO ceramics," Mater. Sci. Eng. B **104**, 45–48 (2003).
13. L. de Martín, J. Sánchez-Prieto, F. Hernández-Jiménez, and J. R. van Ommen, "A settling tube to determine the terminal velocity and size distribution of fluidized nanoparticle agglomerates," J. Nanopart. Res. **16**, 2183 (2013).
14. M. Aldén, A. Omrane, M. Richter, and G. Sarner, "Thermographic phosphors for thermometry: A survey of combustion applications," Pror. Energy Combust. Sci. **37**, 422–461 (2011).

#305901 https://doi.org/10.1364/OE.25.028764
Journal © 2017 Received 5 Sep 2017; revised 31 Oct 2017; accepted 31 Oct 2017; published 6 Nov 2017

Optics EXPRESS

15. M. Köhler, K. P. Geigle, W. Meier, B. M. Crosland, K. A. Thomson, and G. J. Smallwood, "Sooting turbulent jet flame: characterization and quantitative soot measurements," Appl. Phys. B **104**, 409–425 (2011).
16. M. Lawrence, H. Zhao, and L. Ganippa, "Gas phase thermometry of hot turbulent jets using laser induced phosphorescence," Opt. Express **21**(10), 12260–12281 (2013).
17. M. Löffler, F. Beyrau, and A. Leipertz, "Acetone laser-induced fluorescence behavior for the simultaneous quantification of temperature and residual gas distribution in fired spark-ignition engines," Appl. Opt. **49**(1), 37–49 (2010).
18. R. Grena, "Thermal simulation of a single particle in a falling-particle solar receiver," Sol. Energy **83**, 1186–1199 (2009).
19. R. Hasegawa, I. Sakata, H. Yanagihara, B. Johansson, A. Omrane, and M. Aldén, "Two-dimensional gas-phase temperature measurements using phosphor thermometry," Appl. Phys. B **88**, 291–296 (2007).
20. S. P. Kearney, R. W. Schefer, S. J. Beresh, and T. W. Grasser, "Temperature imaging in nonpremixed flames by joint filtered Rayleigh and Raman scattering," Appl. Opt. **44**(9), 1548–1558 (2005).
21. T. C. Lau and G. J. Nathan, "The effect of Stokes number on particle velocity and concentration distributions in a well-characterised, turbulent, co-flowing two-phase jet," J. Fluid Mech. **809**, 72–110 (2016).
22. T. C. W. Lau and G. J. Nathan, "A method for identifying and characterising particle clusters in a two-phase turbulent jet," Int. J. Multiph. Flow **88**, 191–204 (2017).
23. W. Liu, J. Zhang, M. Zhou, and Y. Wang, "The thermal and irradiation degradation mechanisms of Eu 2+,Mn2+ co-doped BaMgAl10O17 phosphor," Sci. China Phys. Mech. Astron. **55**, 1757–1762 (2012).
24. Z. T. Alwahabi, K. C. Y. Kueh, G. J. Nathan, and S. Cannon, "Novel solid-state solar thermal simulator supplying 30,000 suns by a fibre optical probe," Opt. Express **24**(22), A1444–A1453 (2016).

1. Introduction

The heating of particles suspended in a flow is a phenomenon that occurs in a wide range of industrial processes, such as in combustion environments, mineral processing plants and, more recently, in the particle receivers under development for high temperature concentrated solar thermal (CST) systems [1,2]. However, the heat transfer in these non iso-thermal particle-laden flows remains poorly understood because of its complexity, which arises from the coupled and non-linear mechanisms of particle-fluid interactions, inter-particle collisions, particle clustering and radiation attenuation [3,4]. This lack of detailed understanding limits current capacity to optimize particle-laden systems, improve process efficiencies and develop new technologies. Therefore, a reliable, non-intrusive, in situ and spatially resolved technique to measure particle temperatures is necessary for the study of heat transfer within turbulent particle-laden flows. Good temporal resolution is also needed to allow multiple fluctuating qualities to be measured. The overall objective of the present investigation is to contribute to meeting this need.

A range of alternative laser diagnostic measurement techniques meet the criteria by making use of various sophisticated instruments and different optical components to provide in situ and high-speed measurements with high resolution that allow multiple fluctuating quantities to be measured [5]. Among the laser diagnostic techniques most commonly used for temperature measurement of the gas phase, the coherent anti-Stokes Raman spectroscopy (CARS) technique is well-established for accurate point-resolved measurements, and recently planar measurements, even in harsh environments. However, it is not yet to be developed for measurements in the presence of particles [6]. Alternatively, Rayleigh scattering technique is well-established for planar measurements of the gas phase, but are not suited to the measurement of flowing particle temperature [7]. They are also challenging to implement in the presence of particles because of the strong interference from spurious light scattering. Another laser-based method is the laser-induced fluorescence (LIF) thermometry. This utilizes tracers added to the gas flow and is a robust technique typically used to study the relationship between mixture formation and temperature [8]. However, LIF investigations are suited to the measurement of gas or liquid phase, rather than to particles and must also address the effect of halation around the particles.

In contrast, laser-induced phosphorescence (LIP) is a technique that mitigates the effects of these occurrences by using the temperature-dependent properties of thermophosphors (TPs) to determine the temperature of the particles. This technique makes use of phosphorescent emissions of TPs governed by the temperature-dependent Boltzmann

Optics EXPRESS

distribution where the emission spectra shifts with respect to wavelength, the extent of the shifting of which varies with the type of TP used [9]. For the present investigation, the spectral intensity ratio method of LIP is used. Here, the intensity ratio, I_r, is calculated by:

$$I_r = \frac{I_1 - B_1}{I_2 - B_2} \times \frac{I_{2,ref}}{I_{1,ref}} \quad (1)$$

where I is the phosphorescent emission intensity, B is the background signal, the subscripts 1 and 2 is the signal taken at the 2 selected wavelength region and ref denotes a reference case [8]. One advantage of this technique is that a range of TPs exist, each with its own properties such as decay lifetime, emission intensity, operating temperature, and effect of oxygen quenching as documented by many studies [10–12]. This offer the potential to optimize the measurement for any given experimental condition by the selection of an appropriate TP. However, applications of LIP to date have mostly been directed to measurement of the gas-phase temperature using the TP as a tracer, rather than as a measurement of the particle phase itself [13–15]. These measurements have found that volume-averaged measurement of the gas-phase temperature is most effective with relatively high volumetric loadings of the TP. Importantly, this avoids the need to resolve the temperature of individual particles. The resulting accuracy of this type of measurement has been reported to be high. For instance, Abram *et.al* [14]. reported a temperature precision of 4K (5.3%) at low temperature ranges (~363K), and up to 3K (1.4%) at higher temperatures (~500K) using 2µm Eu:BAM particles, while Lawrence *et.al* [16]. reported measurement errors up to 3.1% for 2.9µm Eu:BAM particles and 10.1% for 10.2µm Dy:YAG particles. However, these approaches of using tracer particles in LIP to measure the flow temperature relies on the assumption that the temperature of the gas phase and the particle phase are in equilibrium locally. Hence it can only be applied where heating rates are relatively low and cannot be used to measure heat transfer between particles and the flow. Additionally, despite the high accuracy of the technique, little progress has been made on its application to single-shot particle temperature measurement.

In addition to a laser diagnostic method, a systematic study of the accuracy of a particle temperature measurement technique requires a well-controlled heat source that is capable of achieving high enough heating rates of the particle relative to the flow for the two phases to have a significant temperature differential. This is necessary to measure heat transfer in a particle-laden flow. The preferred method of achieving well-defined, high heating rates of particles is via a radiative heat source because this can be used to heat only the particles via careful choice of wavelength to avoid absorption lines of the gas phase. Previously, radiative heat sources to achieve this have employed various types of lamps such as deuterium, xenon, and tungsten [17,18]. However, these sources cannot be used to generate a true point source, but rather generate "hot-spots" in which certain heating regions have higher heat fluxes than others. It is also difficult to achieve sufficiently high heating rates for the particle temperature to differ significantly from that of the fluid. An alternative solid-state system that achieves uniform, high fluxes with known optical direction has recently been demonstrated by Alwahabi *et.al* [19]. This Solid-State Solar Thermal Simulator (SSSTS) is capable of delivering continuous, well-defined heat flux of up to 36.6 MW/m^2 and operates at a peak wavelength of approximately 910nm, which is absorbed by particles but not by the air.

This investigation is to demonstrate a direct, in situ, non-intrusive, planar measurement of particle temperature in a turbulent flow under well-characterized heating with high-flux radiation. In particular, we aim to determine the resolution and accuracy of a temporally and spatially-resolved, single-shot application of LIP for the measurement of the temperature of micron-sized particles suspended in an unsteady flow heated with a high flux source of laser irradiation.

Optics EXPRESS

2. Experimental

2.1 Particle heating by radiation

The particles were heated with the well-defined and high heat flux heat source Solid-state Solar Thermal Simulator (SSSTS) reported by Alwahabi *et.al* [19]. This provides 3kW of continuous radiation at fluxes, Φ, of up to 36.6 MW/m^2 for which the heating profile, region, and flux are well-characterized and easily controlled. The 910nm wavelength of the SSSTS was chosen to minimize heating of the carrier gas, which in the current experiment was dry air. The SSSTS beam converges from a diameter of 46mm at the fiber-optic head (FOH) to a waist of 10.5 ± 0.1mm diameter over the distance of 520mm-540mm from the FOH.

2.2 Optical arrangement

The optical arrangement is presented in Fig. 1. Here, the third harmonic of an Nd:YAG laser (Quantel Q-smart 850) operated at 5.27 ± 0.47mJ and 355nm (shown in purple in Fig. 1) was used to excite the ZnO:Zn TPs suspended within in a fluidized bed (FB). Three cylindrical lenses (L_1, L_2 and L_3) were used in series to manipulate the excitation laser beam and generate a laser sheet of 300µm thickness at the measurement test section. The subsequent phosphorescent emissions (shown as dotted lines in Fig. 1) from the ZnO:Zn TPs were then recorded with an ICCD camera (PI-Max/PI-Max2, Princeton Instruments) through a 40mm spacer (sp) and an f/2.8 Tamron imaging lens (ImL). The imaging area was 15 mm × 10.8 mm, viewing the y and z plane of Fig. 1. An image splitter, IS (Opto-Split II, Cairns Research), with an in-built conventional dichroic mirror with a 50:50 ratio was used to transmit two images onto a single ICCD camera, as shown in Fig. 2. The use of a single ICCD camera offers the advantage over the more commonly used 2-camera system for LIP of minimizing errors during image processing because both images are collected simultaneously. Two high transmission (> 93%) interference filters at 392 ± 9nm (FF01-392/18-25, Semrock) and 440 ± 20nm (FF01-440/40-25, Semrock) were selected specifically to detect ZnO:Zn phosphorescent emissions. These two bands were selected because they provide the highest sensitivity to the particle temperatures below 625°C [12]. The camera gain, gate width and gate delay were set to 5, 26ns and 51ns respectively, to maximize the phosphorescence signal. The mirror (labelled as M4 in Fig. 1) was also carefully aligned to be 45° with respect to the ICCD camera to minimize relative distortion of recorded images.

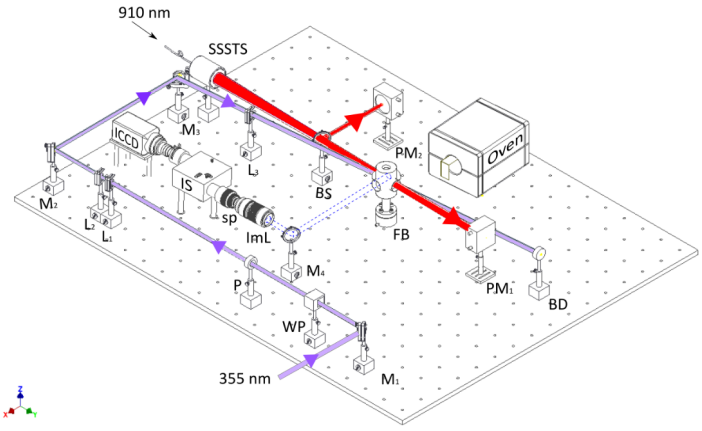

Fig. 1. Optical arrangement. Note that the temperature-controllable oven replaces the fluidized bed during calibration. Purple line: 355nm Nd:YAG laser beam path; Red line: 910nm Solid-State Solar Thermal Simulator (SSSTS) beam path; Blue dashed line: optical collection path of phosphorescence emission. BD: Beam Dump; BS: Beam Splitter; ImL: Imaging Lens; L: Lens; M: Mirror; P: Polariser; PM: Power Meter; sp: spacer; WP: Waveplate.

Optics EXPRESS

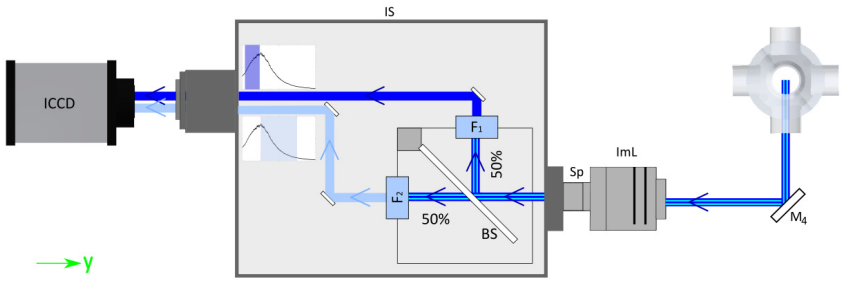

Fig. 2. Image collection via an image splitter. The phosphorescence signal from the excited particles in the fluidized bed were reflected by a mirror (M_4) and passed through the imaging lens (ImL) and spacer (Sp) before entering the image splitter (IS). A beam splitter (BS) within was used to separate the signal to a 50:50 ratio and allowed to pass through different filters, F_1 (392 ± 9nm) and F_2 (440 ± 20nm), the collection wavelengths of which are shaded in blue in the insets. Images over the z and y planes were then collected with an ICCD camera. Temperature is determined from the ratio of the filtered images.

The thermophosphor particles chosen here are made from ZnO:Zn and obtained from Phosphor Technology with a size distribution of 1µm-50µm. It was found during the course of the investigation that the sole use of ZnO:Zn TPs led to significant particle agglomeration, consistent with the findings of Abram *et.al* [14]. Other previous investigations [20,21] have also shown that particles in a fluidized bed of the diameter and sphericity used here have a natural tendency to agglomerate. To minimise these effects, 100µm-200µm sized $CaSO_4{\cdot}2H_2O$ particles were mixed with the TPs with a volumetric ratio of 20:80. These $CaSO_4{\cdot}2H_2O$ particles were chosen not only for their size, but also because they do not emit any phosphorescent signals when excited at the excitation wavelength of 355nm (thereby avoiding interference with signals emitted by the ZnO:Zn particles). The mixture of $CaSO_4{\cdot}2H_2O$ and ZnO:Zn particles was placed in an optically-accessible fluidized bed. The fluidized bed has four 32mm diameter apertures positioned diametrically opposed from each other, with two transmitting the Nd:YAG laser and SSSTS beams through the axis of the reactor and two providing access for the imaging measurements. The path of the Nd:YAG laser was propagated along the y-axis of the system, as shown in Fig. 1, and was offset from the SSSTS beam (shown in red in Fig. 1) path by 7° such that they intercepted at the 10.5mm waist of the SSSTS beam and at the centre of the fluidized bed. A flow controller (Alicat Scientific, MC 20slpm) was used to deliver dry air at a constant volumetric flow rate of 6.5L/min. Dry air was used as an added precaution to avoid the contribution to particle agglomeration that can arise due to humidity. A UV beam splitter (BS) was placed 300mm from the front of the Fibre-optic Head (FOH) of the SSTS laser to split the beam at intensity ratio of 92:8. The low-power beam was directed to a water-cooled power meter (Gentec model HP100A-4KW-HE, labelled as PM_2 in Fig. 1), while the high power beam was passed pass through the working section of the fluidized bed chamber before impinging onto a separate, but similar, water-cooled power meter (labelled as PM_1 in Fig. 1). The power meter readings were recorded at fixed sampling rate of 10Hz. The particle mass loading within the system was estimated by calculating the radiation attenuation by the particles, $\dot{Q}_{att}$. This value was calculated by taking the difference between the two power meter readings at every time-step after correcting for differences in beam power due to the beam splitter, i.e. $\dot{Q}_{att} = \dot{Q}_{in} - \dot{Q}_{out}$, where $\dot{Q}_{in}$ is the power recorded by PM_1 multiplied by 100/92, and $\dot{Q}_{out}$ is the power recorded by PM_2, multiplied by 100/8.

Four K-type thermocouples were also placed within the experimental facility - one protruding into the fluidized bed upstream from the heating zone, one about 50mm downstream from the heating zone within the fluidized bed to provide a measure of the overall rise in the gas-phase temperature, one on the outer surface of the fluidized bed reactor

Optics EXPRESS

and one on the metal enclosure encapsulating the system for safety. The temperatures of all four thermocouples were monitored with an analogue-to-digital converter and recorded to a computer. Table 1 presents the summary of the experimental parameters in the present investigation.

Table 1. Summary of experimental parameter ranges.

Experimental Parameters	
355nm laser fluence	5.27 ± 0.47mJ
Particle diameters	50 – 250 μm
Fluidized bed air flow rate	6.5 L/min
Measurement volume	10.5mm × 10.5mm × 300μm
Spatial resolution	51 pixel/mm
Calibration temperature range	22 - 423°C
SSSTS heat flux	0 – 21.1 MW/m^2

2.3 Temperature calibration

The calibration investigation was performed with a similar experimental arrangement to that described in Section 2.2, except that the fluidized bed in Fig. 1 was replaced by a temperature-controlled oven (MTI Corporation, OTF-1200X-S). A copper plate of 30mm diameter was coated with ZnO:Zn TPs and placed in the oven. The heated plate was then placed within the Nd:YAG laser path such that the excitation laser beam was orthogonal to the plate. The excitation laser beam size and energy was kept constant during calibration. Additionally, a separate K-type thermocouple was attached to the surface of the TP-coated plate to measure in situ the temperature of the TP.

2.4 Image processing

Images were collected through an image splitter, which combines side-by-side onto a single ICCD array image collected through a filter at bandwidth 440 ± 20nm and the other at 392 ± 9nm. Each of the two images records an area of 15mm × 10.5mm and each is collected simultaneously. This avoids the potential for errors associated with different time-delays and/or angular distortion that are typical of using traditional two-camera systems. The resultant spatial resolution for each image was 51 pixels/mm. In-house Matlab codes were then used to divide the original image into two sub-images. The steps performed to obtain particle temperature from the raw images, as illustrated in Fig. 3, are outlined below:

1. Each instantaneous image was thresholded by the average pixel count of the background image to remove electrical noise, as presented in Eq. (1). The background image here refers to the image recorded using the same experimental setup but without the presence of particles. The signal-to-noise ratio (SNR) for the images taken with the 392 ± 9nm filter varied from 13 at Φ = 0 W/m^2 to 5.6 at Φ = 21.1 MW/m^2. Conversely, the SNR for the images taken with the 440 ± 20nm filter was between 5.4 at Φ = 0 W/m^2 and 11 at Φ = 21.1 MW/m^2. This is due to a shift in the phosphorescent emission spectra as the particle temperature increases due to increasing heat flux. It can be seen from Fig. 3 that the final image of temperature yields measurement of significantly fewer particles than do the raw images. This is because data from particles with a non-physical diameter have been rejected. More specifically, particles that are not in the focusing plane appear artificially larger than the actual particle agglomerate size, leading to intensity ratio images that are not reflective of the true particle temperatures. To estimate the true diameter of particle agglomerates, independent images of particles in the fluidized bed were recorded with a NIKON D5500 camera (f/3.1) without excitation at room temperature. It was found that ~80% of the particles comprise agglomerates of diameter in the range 100μm-250μm. Hence particle agglomerates with an imaged diameter > 300μm were assumed to be out of the image plane and were eliminated. Additionally, the

Optics EXPRESS

inferred temperature images of particle agglomerates showed that the measured temperature is significantly greater at the outer edges of some particle agglomerates. This is due to weak signals in these areas, leading to high errors due to a low signal to noise ratio. To account for this, the weighted centroid of each particle agglomerate was found and used to reject the signal from the pixels at the outside of the particles.

2. The two sub-images were super-positioned to overlap each other to within plus/minus 0.1 pixels. This was achieved by utilizing the same image processing method as for the superposition the sub-images with a gridded target, which enables the average offset between the two sub-images to be calculated. Arrays of intensity ratios, I_r, were then calculated by dividing the two sub-images on a pixel-by-pixel basis. A previous investigation of the influence of excitation (355nm) laser fluence on intensity ratio showed that the intensity ratio varied by approximately 25% between laser fluence values of 2.6mJ/cm^2 and 5.17mJ/cm^2. This stems from a slight dependence of phosphorescent emission spectra on the laser fluence. To correct for this, the intensity ratios were normalized by the equivalent intensity ratio obtained at room temperature to correct for this influence following Abram *et.al* [22];

3. Particle temperatures were then inferred from I_r and from the calibration data.

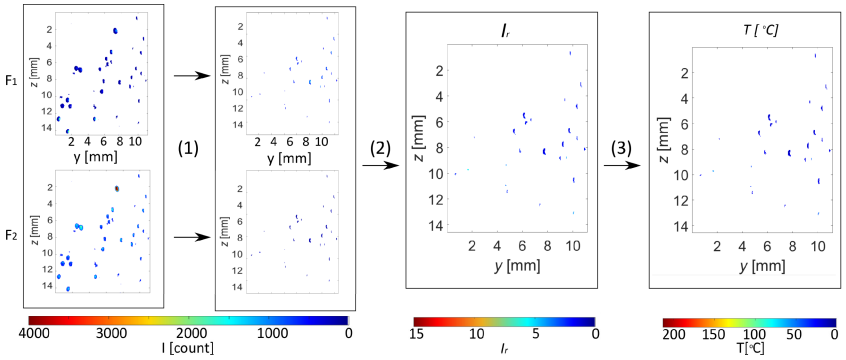

Fig. 3. Image processing procedure of two images obtained from two filters, F_1 (392 ± 9nm) and F_2 (440 ± 20nm): (1) threshold background noise and incoherent signals which, (2) calculate intensity ratio from 2 filtered images, (3) derive temperature from the calibration.

Since particle temperatures may vary in space and time, it is necessary to assess whether the rate of change in temperatures are sufficiently low for local thermodynamic equilibrium to be established. That is, it is necessary to assess whether the temperature of each agglomerate can be determined accurately without considering spatial and/or temporal thermal gradients. This is assessed by comparing the rate of cooling via convection and heating or cooling via radiation relative to the internal transfer via conduction over the particle volume. The Biot number was used to ascertain the degree of thermal equilibrium for the case of convective cooling. Here, the Biot number, *Bi* [23], is defined as:

$$Bi = \frac{h(\forall_p / A_p)}{k_p}, \tag{2}$$

where $A_p = 4\pi r^2$ is the surface area of the particle being heated, $h = \frac{Nuk_g}{D_p}$ is the convective heat transfer coefficient, $Nu = 2 + (0.4 \times Re^{0.5} + 0.06 \times Re^{\frac{2}{3}}) \times Pr^{0.4} \left(\frac{\mu_a}{\mu}\right)^{0.4}$ is the Nusselt

Optics EXPRESS

number, $Re = \frac{\rho V_p D_p}{\mu}$ is the Reynolds number, V_p = 0.6m/s is the slip velocity, $\forall_p$ is the particle volume, k_p is the thermal conductivity of the particle, and k_g is the thermal conductivity of the gas. For cases where Bi « 1, the rate of conductive heating within the particle volume is significantly greater than that of convective cooling, implying that the particle has approached thermal equilibrium. The converse is true for Bi » 1. By analogy, a dimensionless cooling parameter, β_c, was obtained by modifying Eq. (2) to include cooling by convection and radiation, defined as:

$$\beta_c = \frac{\varepsilon\sigma\left(T_1^4 - T_a^4\right)(\forall_p / A_p)F_{12} + h(T_1 - T_a)(\forall_p / A_p)}{k_p(T_1 - T_a)}, \tag{3}$$

where ε = 0.9 is the emissivity, F_{12} = 1 is the view factor of the particle to the surrounding gas and σ=5.67×10^{-8} m^{2}K^{-4} is the Stefan-Boltzmann constant. There, the value of k_p varies with respect to temperature from 27 W/mK at 22°C to 6 W/mK at 700°C [24]. Similarly, to assess equilibrium with regard to radiant heating, we modified Eq. (2) to obtain the heating parameter, β_h, which is the ratio of radiative heat absorption by the particle from the heating laser to the internal heat conduction is defined as:

$$\beta_h = \frac{Q_{rad} F_{13} \alpha}{k \frac{dT}{dD_p}}, \tag{4}$$

where F_{13} = 0.5 is the view factor and α = 0.15 is the absorptivity of ZnO particles. The values of the dimensionless parameters, Bi, β_c and β_h together with Nu and h were evaluated for T_1 = 300°C, T_a = 22°C and radiative flux, Φ, of 21.1 MW/m^2. These are presented in Table 2 for a range of particle diameters. As can be seen, both Bi and β_c « 1, which implies that cooling effects are insignificant. β_h is also « 1. This suggests that the particles approach thermal equilibrium, with any gradients that may be present (e.g. for the largest particles) being small.

Table 2. Characteristic heat transfer parameters estimated for various particle agglomerate sizes assuming T_1 = 300°C, T_a = 22°C and radiative flux, Φ = 21.1 MW/m^2.

Particle diameter, D_p	Re	Nu	h	Bi	β_c	β_h
µm			W/m^{2}K			
50	0.636	2.32	1777	5.7×10^{-4}	5.6×10^{-4}	2.7×10^{-3}
100	1.273	2.46	942.3	5.8×10^{-4}	7.3×10^{-4}	3.5×10^{-3}
200	2.545	2.67	510.1	6.2×10^{-4}	9.2×10^{-4}	7.1×10^{-3}
300	3.718	2.83	360.3	6.5×10^{-4}	1.1×10^{-3}	1.1×10^{-2}

3. Results and discussion

3.1 Temperature calibration

To calibrate the temperature of the ZnO:Zn particle agglomerates as a function of phosphorescence emission, 45 sets of measurements were systematically collected at temperatures ranging from 22°C to 425°C. For each temperature, the TP-coated plate was allowed to reach thermal equilibrium before 100 images were taken. The average intensity ratio was then calculated from the 100 instantaneous measurements for each temperature. The relationship between the intensity ratio and temperature was then used to infer particle temperature from the second set of experiments undertaken within the fluidized bed. The

Optics EXPRESS

accuracy of the calibration was found to be within ± 1% after comparing the intensity ratio of the 100 instantaneous measurements at the same temperature.

3.2 Moving particle temperature measurement

During each measurement, suspended particles were subjected to simultaneous excitation by the Nd:YAG laser and radiative heating by the SSSTS. Measurements of particle temperature were taken with 14 different values of heat flux with the SSSTS laser in the range of 2.4 MW/m^2 ≤ Φ ≤ 21.1 MW/m^2. For each of these measurements, the first 50 (≈30s) and last 100 (≈60s) of the 800 total shots were recorded with the SSSTS deliberately switched off. Figure 4 presents examples of particle images, in which columns A and B are individual particle agglomerate images taken with the FF01-440/40-25 and FF01-392/18-25 filters respectively, while column *C* shows the resultant inferred particle temperature, T_p, based on the calibration curve. Additionally, rows (1) to (5) present heat fluxes for the selected cases of 0 MW/m^2 (i.e. the case with no radiative heating), 3.34 MW/m^2, 6.93 MW/m^2, 12.4 MW/m^2, and 21.1 MW/m^2. As it can be seen, the particle intensity increases with the heat flux for the images in column A (440nm ± 20) and decreases for images in column B (392 ± 9nm). This shows that the emission spectra of the TPs shifts towards longer wavelengths as the heat flux is increased, consistent with the measurements of Särner *et.al* [12].

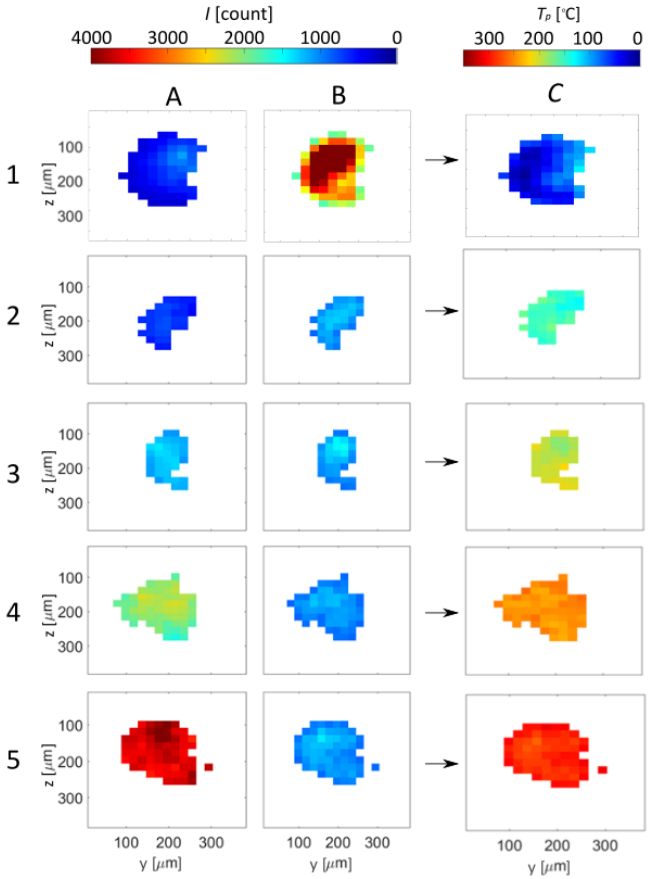

Fig. 4. Typical examples of image trios of particle agglomerates, comprising raw image pairs 440 ± 20nm (column A) and at 392 ± 9nm (column B), together with the resulting temperature, T_p (column C), recorded for five values of radiative heat flux, Φ: (1) 0 MW/m^2, (2) 3.34 MW/m^2, (3) 6.93 MW/m^2, (4) 12.4 MW/m^2, and (5) 21.1 MW/m^2.

Optics EXPRESS

It can also be seen that most of the images of particles in Fig. 4 are non-spherical. This apparent non-sphericity was true for most particles. It is possible that this non-sphericity is genuine and is attributed to the agglomeration process, although a possible contributor is the artefacts that can arise, even for spherical particles, due to their interaction with a light sheet of finite thickness. Figure 5 presents examples of non-spherical images of particles, together with a plausible explanation of the type of shape that could be expected from the position of a spherical particle within a light sheet. In this figure, the direction of the excitation (355nm) laser sheet is from left to right and the camera is facing into the page at a direction orthogonal to the laser sheet. For the case in which the particle is entirely within the laser sheet (a), only half the particle facing the excitation beam is excited, so that the phosphorescence originates only from half of the particle. However, for the case where the particle is partly out of the laser sheet, the particle image can be either half-annular in shape (b) or a truncated circle (c), depending on whether the particle is out of the light sheet in the out-of-plane directions, respectively. This complicates the interpretation, because it is difficult to distinguish between small particles and particles that are simply not fully in the laser sheet. However, this challenge can be reduced in future applications through the use of mono-dispersed (and de-agglomerated) particles, for which the size is known.

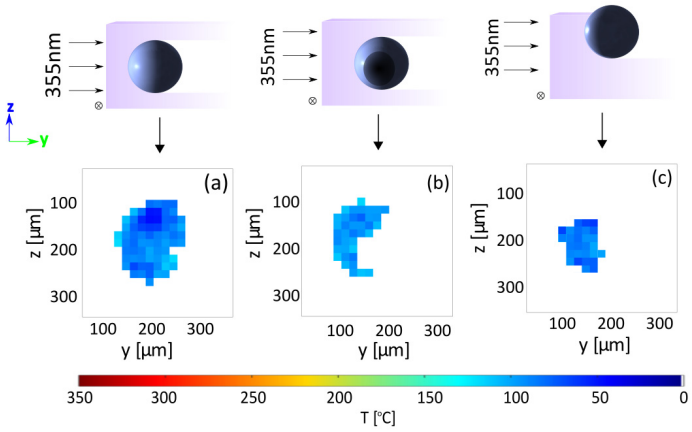

Fig. 5. Examples of particle appearances with respect to their locations in the excitation laser sheet, y.

3.3 Temperature distribution within a particle

Figure 6 presents a histogram of $T_p/T_{p,mean}$, where $T_{p,mean}$ is the mean temperature of each individual particle, so that the ratio is normalized for each particle. The data is presented on a pixel-by-pixel basis calculated from all particles within the series of 650 captured ICCD images for the case in which Φ = 12.4 MW/m^2, together with temperature distribution of 2 individual particle agglomerates within the inset of the figure. It can be seen that the extreme range of measured temperature is ± 6% relative to the modal (i.e. most commonly occurring) temperature while the RMS of the temperature is ± 4%. Given that both β_c and β_h number of the particle agglomerates are <1 [see Table 1], it can be deduced that temperature gradient within any single particle is negligible. This deduction is further supported by observation of the distribution of the scatter in individual particles [Fig. 4], which appears to be random, rather than systematic. Therefore, the T_p variation observed in Fig. 4 can be attributed to noise from the two ICCD images, rather than to any actual temperature variations within the particles. On this basis, the influence of noise can be overcame by averaging from a sufficiently large number of pixels and the resolution of the present images can be deduced to be sufficient for the peak of the measured temperature to be reliably.

Optics EXPRESS

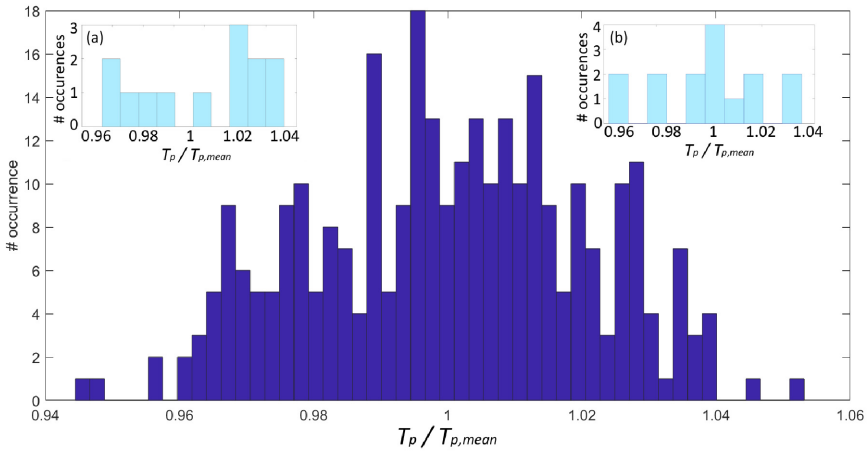

Fig. 6. Lumped probability distribution of the normalised temperatures within each particle, T_p, as calculated from all particles in the 650 images when heated at 12.4 MW/m^2, while the insets present the temperature distributions within individual particles.

3.4 Heated particle temperatures

Figure 7 presents the mean of all particle temperatures, $\overline{T_{p,m}}$, calculated from each series of 650 captured images as a function of radiative heat flux, Φ. The error bars here shows the maximum-minimum range of $\overline{T_{p,m}}$ at any given flux, which is attributed to fluctuations in particle mass loading in the fluidized bed flow between measurement shots. Despite some scatter, it can be seen that $\overline{T_{p,m}}$ scales linearly with Φ.

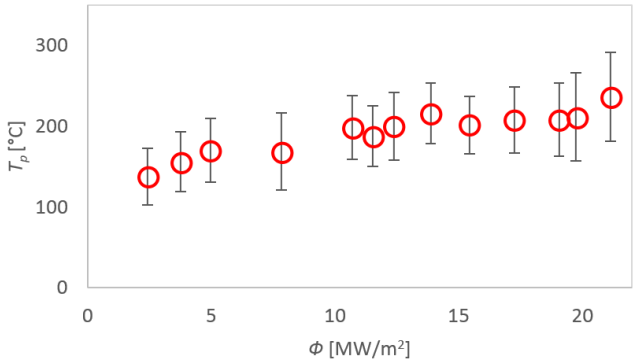

Fig. 7. Mean particle temperature, $\overline{T_{p,m}}$, at various heat flux, Φ.

Figure 8 presents the radial distribution of $\overline{T_{p,m}}$ each calculated from the relevant series of 650 images for which the radiative heat source was switched on, together with their standard deviations. It can be seen that in addition to the primary influence of heat flux on T_p, the distance of the particles from the source of radiation has a secondary influence. That is, particles closest to the heat source have a higher T_p than those further away, consistent with the expected role of attenuation. It can also be seen that particle temperature rises of between 40°C and 280°C were measured for Φ = 2.4 MW/m^2 and 21.1 MW/m^2, respectively. Given that temperature gradients within individual particles were negligible, this large scatter in T_p is attributed to the unsteadiness of particle mass loading within the fluidized bed, consistent with the fluctuations in the measured values by the power meter.

Optics EXPRESS

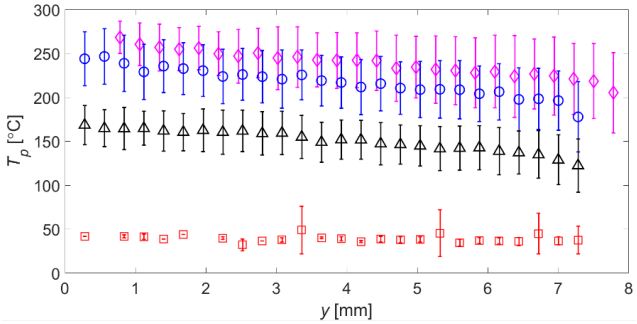

Fig. 8. Particle temperature, T_p, averaged from all particles over 650 images with respect to heating beam direction, y. Error bars represent the minimum-maximum particle temperatures while heat flux was kept constant: square: Φ = 0 MW/m^2; triangle: Φ = 3.34 MW/m^2; circle: Φ = 12.4 MW/m^2; diamond: Φ = 21.1 MW/m^2.

The local heating rate of the particles within the irradiated zone was calculated based on the residence-time, τ, of the particles within the heating zone. Several 2D, long exposure images were taken with the ICCD camera aligned normal to the laser sheet. The distance of each particle was recorded then divided by the 3ms exposure time to obtain an average velocity of 0.21m/s. On this basis, given the path length through the heating zone of 10.5mm, the average residence time was 0.035s, while the maximum value was 0.05s. Dividing the maximum temperature rise, ΔT_{max}, by the τ yields an averaged local heating of 23,000°C/s.

4. Conclusion

A temporally and spatially-resolved, single-shot temperature measurement of individual micron-sized particle agglomerates transported in an unsteady flow has been demonstrated. Measurements were performed for particle agglomerates of diameters 20μm ≤ D_p ≤ 300μm under β_c and $\beta_h < 1$), so that any gradients within the particle can be neglected to first order. This is consistent with the measured variation in pixel-to-pixel temperature being both randomly distributed spatially and within ± 4% for irradiated heat flux, Φ = 12.4 MW/m^2. Hence, this variation can be explained by the noise from the image intensifier of the ICCD camera, so that the average can be expected to provide a good measure of the particle temperature. Additionally, a spatial resolution of 51 pixels/mm was achieved, with the signal-to-noise ratio being approximately 11. This gives confidence that the mean temperature of the particle is reliable.

Mean particle temperatures in the range 100°C ≤ $\overline{T_{p,m}}$ ≤ 300°C were measured for the suspended particles irradiated with heat flux between 2.4 MW/m^2 ≤ Φ ≤ 21.1 MW/m^2. A maximum temperature rise of 350°C was recorded with a heat flux of 21.1 MW/m^2. For these conditions, the corresponding heating rate was estimated to be up to 23,000°C/s, given a maximum residence time of the particles in the heating region of 0.05s. The dependence of particle temperatures with respect to their distance from the heat source, residence time and heat flux was found to be consistent with expected trends, providing further confidence in the reliability of the method.

Funding

Australian Research Council: Discovery grant 150102230; Linkage Grant LE130100127.

Acknowledgment

The authors would also like to thank Mr. Jeffrey Hiorns and Mr. Jason Peak, from the mechanical workshop at the School of Chemical Engineering, for their outstanding technical support.

Chapter 7:

Influences of Buoyancy in a Particle-laden Jet under the Presence of Strong Irradiation

Statement of Authorship

Title of Paper	Influences of buoyancy in a particle-laden jet under the presences of strong irradiation
Publication Status	☐ Published ☐ Accepted for Publication ☑ Submitted for Publication ☐ Unpublished and Unsubmitted work written in manuscript style
Publication Details	K.C.Y. Kueh, T.C.W. Lau, Z.T. Alwahabi, G.J. Nathan, Influences of Buoyancy in a Particle-laden Jet under the Presence of Strong Irradiation

Principal Author

Name of Principal Author (Candidate)	Kimberley C.Y. Kueh		
Contribution to the Paper	Set up experimental arrangements, performed experiment, process and analyse results. Took primary responsibility of writing the paper		
Overall percentage (%)	60		
Certification:	This paper reports on original research I conducted during the period of my Higher Degree by Research candidature and is not subject to any obligations or contractual agreements with a third party that would constrain its inclusion in this thesis. I am the primary author of this paper.		
Signature		Date	23/08/2019

Co-Author Contributions

By signing the Statement of Authorship, each author certifies that:

i. the candidate's stated contribution to the publication is accurate (as detailed above);

ii. permission is granted for the candidate in include the publication in the thesis; and

iii. the sum of all co-author contributions is equal to 100% less the candidate's stated contribution.

Name of Co-Author	Timothy C.W. Lau		
Contribution to the Paper	Assisted in the processing of experimental results and editing of manuscript.		
Signature		Date	28/08/2019

Name of Co-Author	Zeyad T. Alwahabi		
Contribution to the Paper	Supervised the analysis of experimental results and assisted with editing the manuscript.		
Signature			

Name of Co-Author	Graham J. Nathan		
Contribution to the Paper	Supervised the analysis of experimental results and assisted with editing the manuscript.		
Signature		Date	26/8/2019

Influences of Buoyancy in a Particle-laden Jet under the Presence of Strong Irradiation

Kimberley C.Y. Kueh[a,c], Timothy C.W. Lau[a,c], Zeyad T. Alwahabi[b,c], Graham J. Nathan[a,c]

[a] *School of Mechanical Engineering, The University of Adelaide, SA 5005, Australia*
[b] *School of Chemical Engineering, The University of Adelaide, SA 5005, Australia*
[c] *Centre for Energy Technology, The University of Adelaide, SA 5005, Australia*

Abstract

The influence of buoyancy on particle aggregates in a vertical, laminar particle-laden jet flow subjected to strong irradiance was assessed experimentally using laser-induced phosphorescence (LIP) to spatially and temporally-resolve measurements of particle temperature, size and number density. These data were analysed by comparison with the results from a simple first-order analytical model that considers radiative heating, convective cooling, radiative heat loss and heat gain of a single spherical particle. As expected, the heat flux, particle concentration and to a lesser extent, particle diameter all affect particle temperatures. At low heat fluxes ($\dot{Q}_{rad} \leq 6.1$ MW/m^2), particle concentration and temperature were found to be higher in the outer regions of the jet ($r/D \rightarrow 0.5$), consistent with previous investigations. However, at higher heat fluxes ($\dot{Q}_{rad} \geq 20.6$ MW/m^2), two distinct regions of high particle temperatures were observed upstream from the heating region (one at the jet axis, and one at the jet edge) for heat flux. Furthermore, in both cases, the results show that smaller particles migrated away from regions of high local temperature. These observations are attributed to the combined effect of thermophoresis and buoyancy.

1. Introduction

The process of heat transfer within particle-laden flows remains poorly understood despite many investigations, due to the complexity of simultaneously-occurring mechanisms such as fluid-particle interactions, inter-particle collisions, buoyancy, particle clustering, light scattering and shadowing within the flow (Baker et al., 2017; Frankel et al., 2016; Lau et al., 2019; Monchaux et al., 2012; Zamansky et al., 2014, 2016). This lack of detailed understanding limits the reliability of models typically used in the design process to optimise the performances of processes involving particle-laden flows. As an example, solar thermal particle receivers have been identified as having strong potential among emerging concentrated solar thermal (CST) technologies to achieve much higher temperatures than commercially available systems due to their lower overall costs and highly efficient heat transfer from direct concentrated solar irradiation (Grena, 2009). However, one limitation on the rate of development of these new generation technologies is sub-optimal heat transfer within the receiver (Ordóñez et al., 2014). Hence, it is important to develop a more

comprehensive understanding of the fundamental processes that occur within these systems, including the effect of flow dynamics on heat transfer.

Particle-laden flows are known to be complex, with the extent to which they couple with the turbulence increasing with increasing particle volume loading, ϕ (Elghobashi, 2006). This is especially true for flows within the four-way coupling regime ($\phi > 10^{-3}$), where inter-particle and fluid-particle interactions both play important roles. A further complicating phenomenon that occurs in particle-laden flows is thermophoresis, which causes particles to migrate either towards or away from regions of higher local temperatures, depending on particle size (Han and Mungal, 2000; Montassier et al., 1991; Tsai et al., 2004). Studies by Tsai et al. (2004) showed that thermophoresis affects particles of diameter 0.4μm at temperature differences as low as 68°C. Thermophoresis is typically observed by one of two methods, the measurement of the velocity of a charged particle as it moves from rest under the influence of gravity, thermal, and electrostatic forces, or by measurement of the motion of particles within a narrow channel that generates thermal gradients (Talbot et al., 1980). However, these measurements have not included spatially resolved data for the particle temperatures. Hence, there is a need for direct measurements of particle temperatures within particle-laden jets that are directly heated by radiation.

Another phenomena that has been observed, but remains poorly understood, is that of self-generated turbulence in particle-laden flows under the presence of strong irradiance (Rahmani et al., 2018; Zamansky et al., 2014). Strong thermal gradients have also been observed to generate preferential particle concentration, i.e. non-uniformity in the local particle distributions (Zamansky et al., 2014). The direct numerical simulations (DNS) by Frankel et al. (2016) found that when heated at low irradiation, particles shed plumes of buoyant gas that reduces the mean settling velocity, thereby reducing turbulence. This was qualitatively observed under the two-way coupling region ($\phi = 10^{-5}$), where 40μm diameter particles were heated with a heat flux of 2MW/m^2, and the expected temperature of the particle phase compared to the fluid, T_p/T_0 was 2.21. However, as the irradiation is increased, buoyancy-driven vortices that enhance turbulence becomes dominant instead (Frankel et al., 2016; Zamansky et al., 2014). This phenomenon is relevant for the understanding in non-isothermal systems such as the heating of falling particles through an aperture in solar particle receivers. However, no direct experimental observations of the role of buoyancy in strongly irradiated flows is available. Hence, new experimental measurements are needed of these phenomena in a radiatively-heated particle-laden flow with high heating rates.

Most previous investigations of the temperature in particle-laden flows has been performed in pre-heated jets (Abram et al., 2013; Fond et al., 2012; Jovicic et al., 2015; Lavieille et al., 2004), in which the solid and gas phases are assumed to be in thermal equilibrium. These investigations inferred the particle temperature from measurements of the gas temperature (e.g. using a thermocouple) and fundamental heat transfer equations. However, such methods are highly idealised, and do not represent realistic heat transfer within a particle-laden flow field. These models ignore the unsteady and non-homogeneous heat transfer processes between the particles and the carrier fluid, particularly in radiatively heated conditions that are relevant to many industrial processes. Other previous measurements in heated

particle-laden flows have employed velocimetry together with temperature measurements of the gas phase to deduce the cooling effects as a jet flow exits from the pipe. However, no in-situ measurements are available of the parameters that control the heat transfer process of radiatively-heated particles within a jet, downstream from the pipe exit. Hence there is a need for new assessments with direct and spatially-resolved measurement of particle temperature. One such method that can provide this is laser-induced phosphorescence (LIP), which has recently been demonstrated to provide spatially and temporally-resolved measurements of particle temperature within a particle-laden flow in a fluidised bed (Kueh et al., 2017). This method presents an opportunity to meet the need for such data.

Another recent development in experimental methods provides new opportunities to achieve the high heating rates that are needed for the particle temperature to differ significantly from the fluid, while also avoiding strong interference to optical diagnostic methods. This development is the Solid-State Solar Thermal Simulator, a well-defined radiative heat source capable of delivering heat flux of up to 36.6MW/m^2 (Alwahabi et al., 2016) at heating rates of up to 23,000°C/s (Kueh et al., 2018). The Fibre-Optic Head feature of the SSSTS, which includes a three-lens system to collimate the beam, enables the generation of a true point-source that avoids the "hot-spots" of traditional radiative heat sources such as xenon and deuterium lamps. It operates at a peak wavelength of 910nm, which is absorbed strongly by the solid phase but only very weakly by the carrier gas phase. This unique characteristic of the SSSTS means that particles can be the sole heat source to the gas through conduction at the boundary layer and convection due to the slip velocity between the two phases. Another advantage of the SSSTS operating at this wavelength is that it is well away from operational wavelengths required by the LIP technique, allowing more accurate particle temperature measurements. As such, the SSSTS was selected to be used in the present investigation.

For the reasons described above, the aim of the present investigation is to provide new insight into the heat transfer within a particle-laden jet flow under well-characterised heating with high flux radiation through first-of-a-kind spatially and temporally resolved measurements. In particular, we aim to experimentally investigate the relationship between incident heat flux and particle temperature distributions within a jet flow under strong irradiation in the two-way coupling regime, where effects of buoyancy have been predicted to be significant.

2. Experimental arrangement

The experiment was conducted on a laminar particle-laden jet issuing from a long, round pipe, as shown in Figure 1. The pipe diameter was D =12.8mm, while the pipe length-to-diameter ratio was L/D = 39.06. This is sufficiently long to result in a fully-developed laminar pipe flow at the pipe exit for the single-phase case, although the required length for fully-developed two-phase flow is not yet well understood. The pipe was oriented vertically downwards within a vertical wind tunnel with a 300mm×300mm cross section. A combination of two screens and a honeycomb layer were placed directly below the wind tunnel inlet to generate a nominally uniform co-flow with negligible boundary effects within the imaging section. The volumetric mass flow rate of air was maintained at 13L/min (equivalent to bulk velocity, U_b = 1.7m/s at the pipe exit) using a mass flow controller (Alicat Scientific, MC 20 SLPM). The resultant

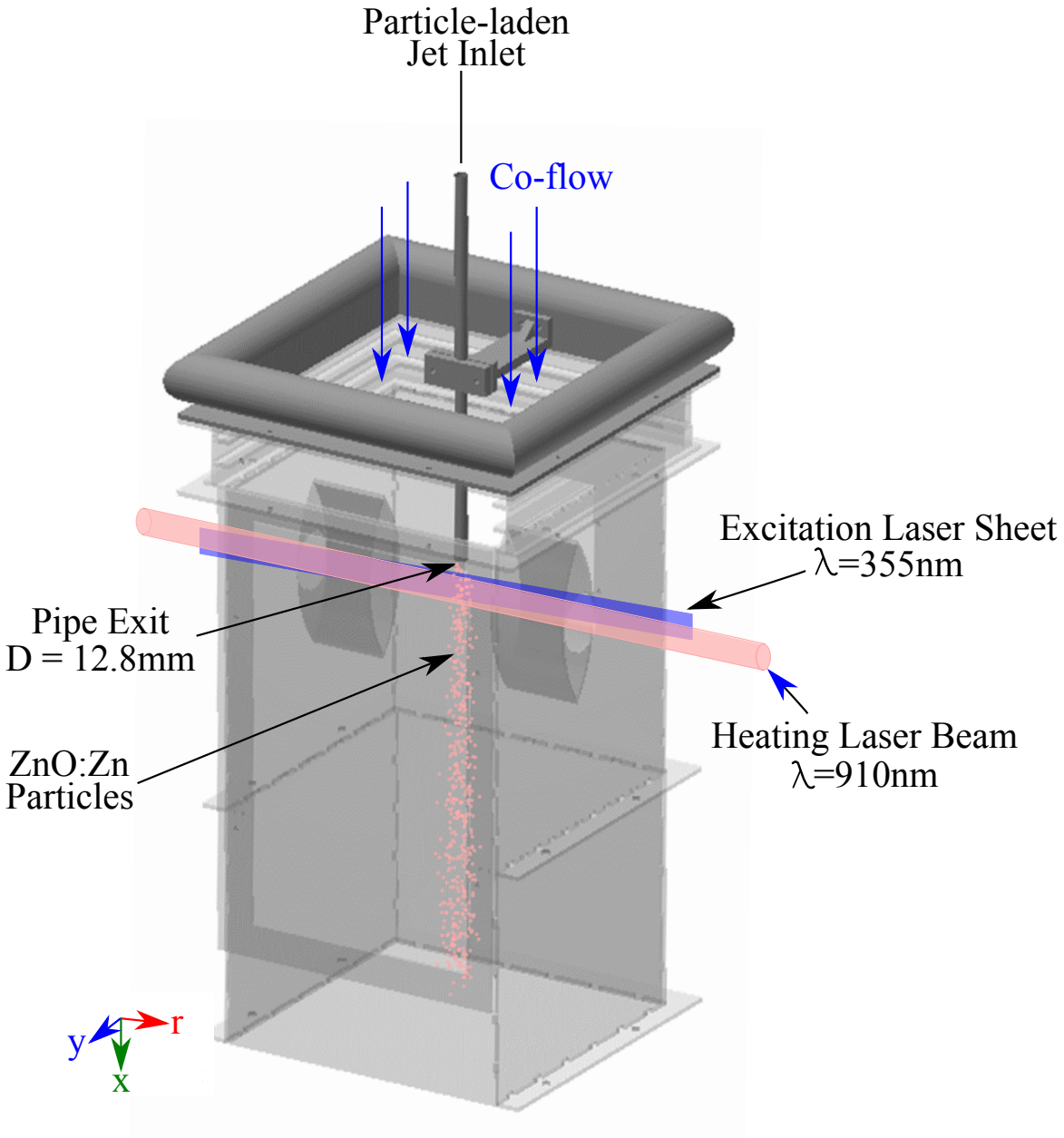

Figure 1: ZnO:Zn particles (red dots) seeded through a 12.8mm diameter round pipe in a 300mm×300mm wind tunnel. The blue laser path indicates the 355nm Nd:YAG laser excitation, while the red indicates the 910nm SSSTS heating beam.

Reynolds number, based on the pipe diameter, was $Re_D = \rho_a U_b D/\mu_a = 1{,}500$, where ρ_a and μ_a are the fluid density and dynamic viscosity, respectively, at room (ambient) temperature.

The particle-laden flow consisted of air and ZnO:Zn thermophosphors (TPs) seeded from a fluidised bed feeder. This TP was chosen due to its high phosphorescence emission signal and temperature sensitivity at operating temperatures below 625°C (Kueh et al., 2017). It was found during the course of the present investigation that the sole use of ZnO:Zn TPs led to significant particle agglomeration, consistent with the findings of Abram et al. (2013). As such, a pressure-controlled fluidised bed feeder as shown in Figure 2 was used in the present investigation to minimise the aggregation. It can be seen that the feeder has two outlets, one at the top to convey air and some fine particles, and one at the centre of the bed, comprising a tube with a 1mm hole to convey fluidised particles and air. A primary air flow of 12L/min was fed from the bottom of the fluidised bed feeder to maintain the fluidisation, while a secondary air flow of 1L/min was fed through the secondary tube. Particles were entrained through the 1mm hole into the secondary air stream, while a relatively small fraction (by orders of magnitude) of smaller particles were also transported through the bypass stream (colored in red in Figure 2). The resultant flow was therefore found to consist of two particle size ranges, particle agglomerates with an effective diameter of $d_p \geq 50\mu$m, and a small fraction (by volume) of smaller particles, $d_p \leq 20\mu$m.

The third harmonic of a pulsed Nd:YAG laser (Quantel Q-smart 850) operated at a wavelength of at λ = 355nm and an energy per pulse of 6.24$\pm$0.41mJ (shown in blue in Figure 1) was used to excite the TP particles. The geometry of the laser beam was manipulated with three cylindrical lenses positioned in series to form a 0.3mm (thickness)$\times$18mm (height) laser sheet. The top of the laser sheet was aligned directly below the pipe exit. The resultant phosphorescent emissions from the excited ZnO:Zn TPs were recorded with an ICCD camera (PI-Max/PI-Max2, Princeton Instruments) fitted with an image splitter (Opto-Split II, Cairns Research), through a 40mm spacer and an f/2.8 Tamron lens. The image splitter, which has an in-built dichroic mirror that divides the imaging area into two equal 18.2mm $\times$ 9.6mm images, was fitted with two high transmission (> 93%) interference filters at 392$\pm$9nm (FF01-392/18-25, Semrock) and 440$\pm$20nm (FF01-440/40-25, Semrock). These filters were chosen for their sensitivity to ZnO:Zn phosphorescent emissions at temperatures below 625°C. A detailed analysis of thermophosphor spectral response, filter selection, and measurement accuracy is provided by Kueh et al. (2017). Images of the flow were recorded within the region corresponding to $-0.06 \lesssim r/D \lesssim 0.72$ and $0 \lesssim x/D \lesssim 1.57$, where r and x are the radial and axial co-ordinates, respectively.

Particles were heated using a Solid-State Solar Thermal Simulator (SSSTS) operating with a 10.5mm beam diameter (shown in red in Figure 1) and at a wavelength of λ =910nm. The SSSTS beam was aligned at a 7° angle to the Nd:YAG laser path and placed approximately 6.5mm below the pipe exit, such that the region heated by radiation corresponded to $0.1 \lesssim x/D \lesssim 0.9$. A water-cooled power meter (Gentec model HP100A-4KW- HE) acted as SSSTS beam dump, while also providing in-situ laser power measurements at a sample frequency of 10Hz. Temperatures of the ZnO:Zn particle aggregates and their respective positions were investigated at 13 different heat fluxes in the range

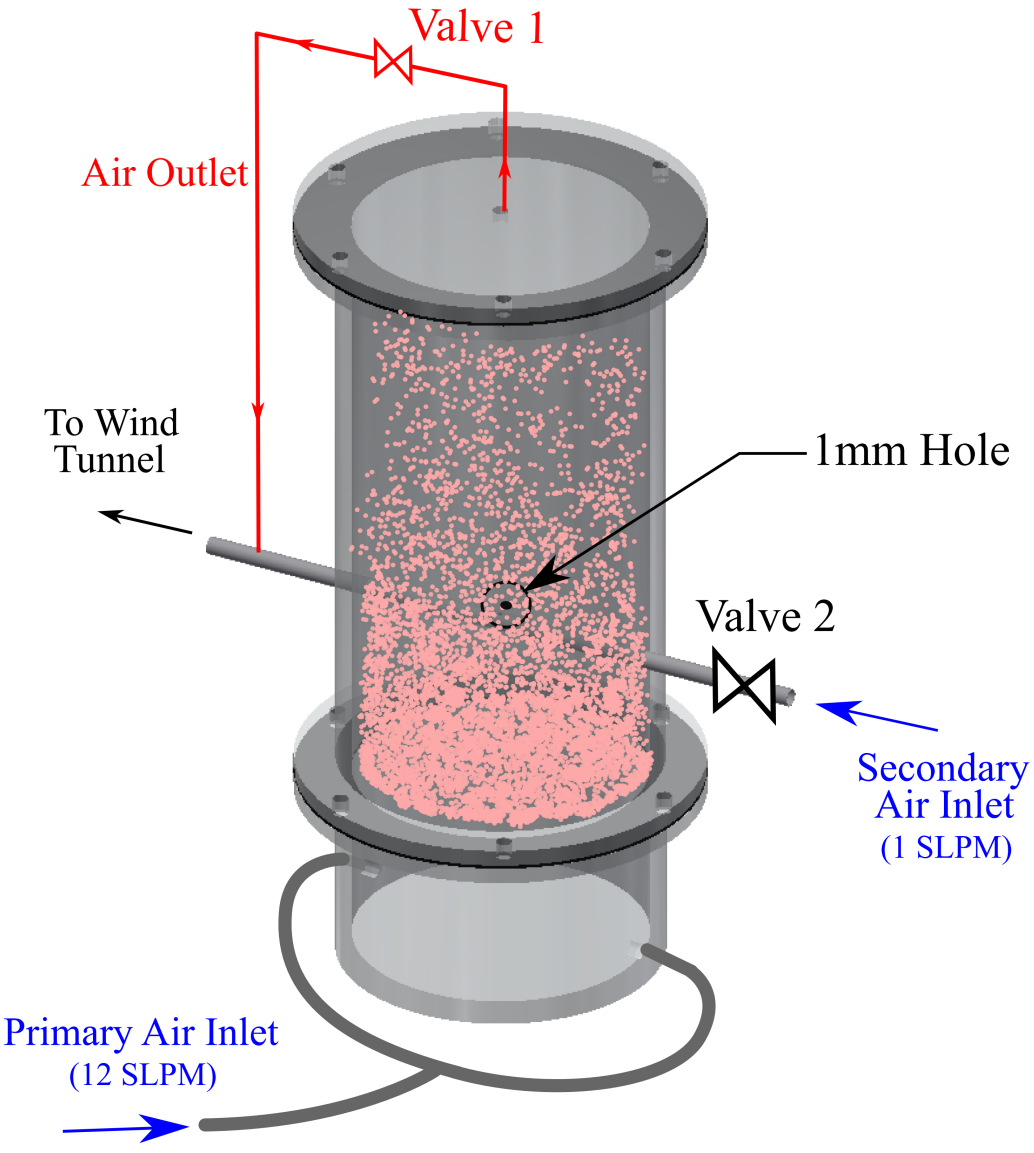

Figure 2: Schematic diagram of the fluidised bed feeder. Two valves were used to control the pressure in the feeder and particle mass loading in the system.

2.1MW/m^2 $\leq \dot{Q}_{rad} \leq$ 35.5MW/m^2. For each flux, 4000 single-shot images were collected over several days to ensure repeatability.

To relate phosphorescent emissions to temperature, a calibration experiment was performed with the same experimental arrangement, with the exception that a TP-coated plate in a temperature-controlled oven was placed in the optical probe region instead of the particle-laden jet. A 30mm diameter copper plate was coated with the ZnO:Zn TPs and placed in the oven. The Nd:YAG laser beam was then directed orthogonal to the plate to excite the coated particles. A detailed description of the calibration experimental setup and the image processing methodology is presented by Kueh et al. (2018).

An example of the image processing procedure is presented in Figure 3, where (a) and (b) correspond to the raw images taken from two filters at I_1 = 440±20nm and I_2 = 392±9nm. The raw images were each thresholded for signals below 1000 counts, and super-positioned to overlap each other within ± 0.1 pixels. Arrays of intensity ratio, I_1/I_2, were then calculated by dividing the two thresholded images, as seen in Figure 3(c). It can be seen that there are fewer particle aggregates in this image than those found in the raw images. This is because particles with low signal to noise ratio have been excluded from this assessment. That is, only particles with sufficiently strong signals were used to calculate particle temperature. From Figure 3(c), particle aggregate temperatures were then inferred from the calibration data, as seen in Figure 3(d).

2.1. Heat transfer model

A simple first-order heat transfer model of a single spherical particle subjected to radiative heating at high fluxes was used to estimate particle temperature, T_p, under conditions similar to that of the experimental arrangement. The heat transfer modes taken into account were the radiative heating of the particle, $\dot{Q}_{rad,heat} = \alpha(\pi/4)\,d_p^2\dot{Q}_{rad}$, convective cooling between the particle and surrounding flow, $\dot{Q}_{conv} = h\,\pi\,d_p^2\,(T_p - T_a)$, and particle re-radiation to the surroundings, $\dot{Q}_{rad,cool} = \varepsilon\,\sigma\,\pi\,d_p^2(T_p^4 - T_a^4)$, where $\alpha = 0.15$ is the absorptivity of the particle (Schunk, 2008), $h = Nu\,d_p/k_{film}$ is the convective heat transfer coefficient, Nu is the Nusselt number, k_{film} is the thermal conductivity of the fluid evaluated at the film temperature ($T_{film} = 0.5(T_a + T_p)$), T_a is the ambient temperature, $\varepsilon = 0.69$ it the particle emissivity and $\sigma = 5.67 \times 10^{-8}$W/(m^{2}K^4) is the Stefan-Boltzmann constant. The Nusselt number was calculated based on the empirical equation $Nu = 2 + (0.4Re_p^{1/2} + 0.06Re_p^{2/3})\,Pr^{0.4}\,(\mu_a/\mu_{film})^{0.4}$, where $Re_p = \rho_{film}\left|U_{slip}\right| d_p/\mu_{film}$ is the particle Reynolds number, ρ_{film} and μ_{film} are the fluid density and dynamic viscosity evaluated at the film temperature, respectively, U_{slip} is the slip velocity, and Pr is the Prandtl number of the fluid. The slip velocity was estimated to be $U_{slip} = 0.2U_g$ (Lau and Nathan, 2016), while the gas velocity was assumed to follow the velocity profile of a laminar pipe flow, i.e. $U_g/U_b = 2\left[1 - (2r/D)^2\right]$. The particle temperature was then numerically calculated using the equation

$$\dot{m}_p C_p \frac{\partial T_p}{\partial t} = \dot{Q}_{rad,heat} - \dot{Q}_{conv} - \dot{Q}_{rad,cool} \tag{1}$$

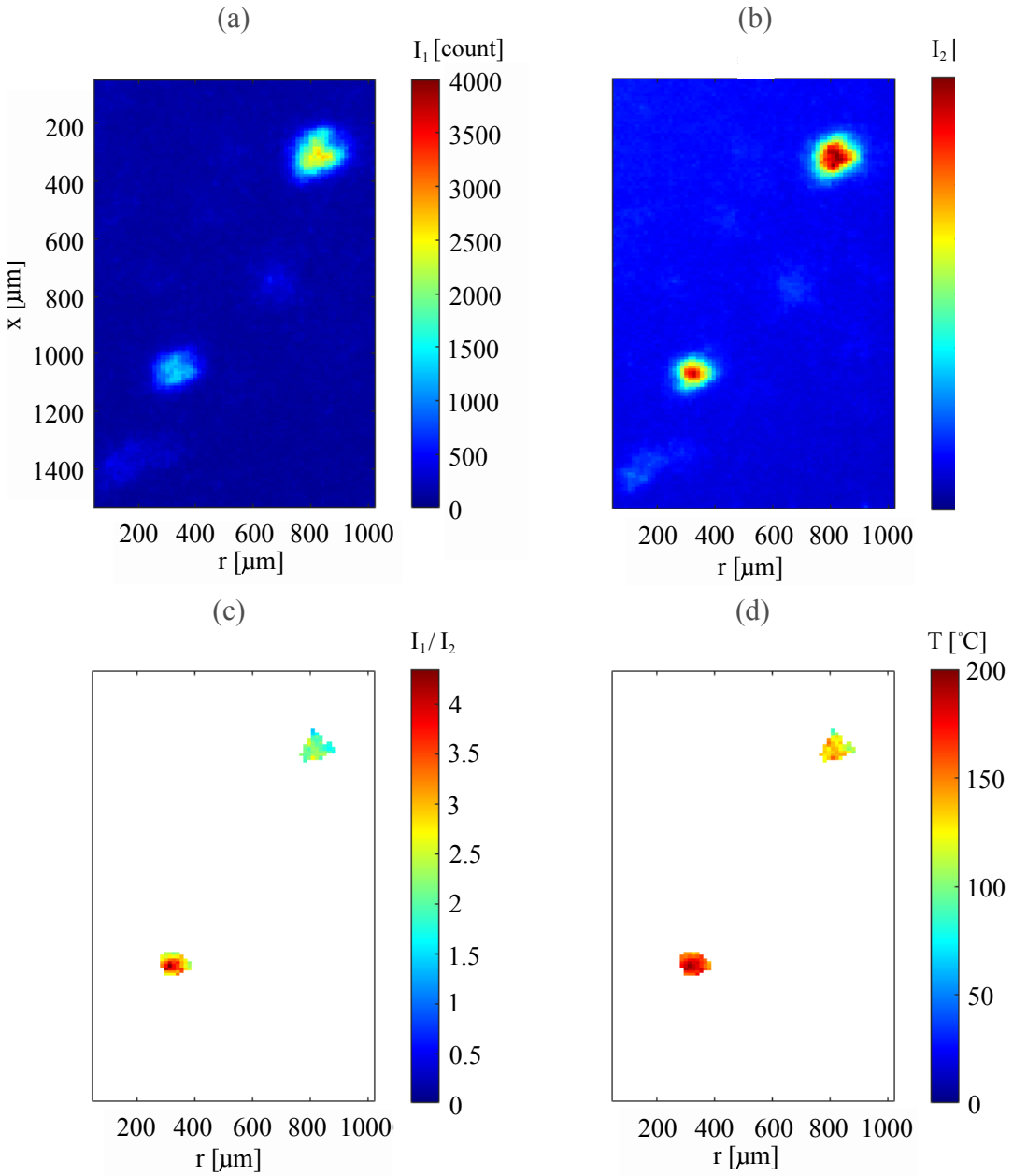

Figure 3: Image processing procedure: (a) I_1 taken at 440±20nm; (b) I_2 taken at 392±9nm; (c) the super-position of two images after thresholding data below 1000 counts; (d) particle temperatures inferred from I_1/I_2 and calibration data.

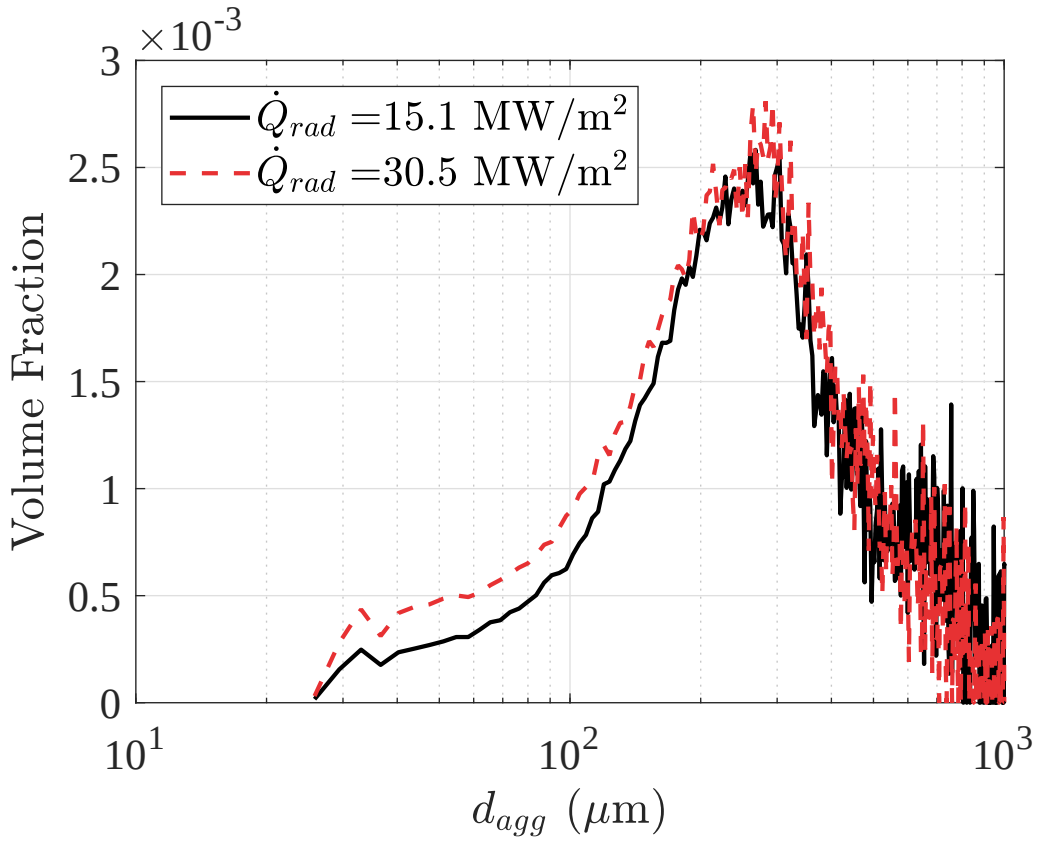

Figure 4: Particle aggregation size distribution obtained from resolving pixel numbers during image processing for the cases of $\dot{Q}_{rad} = 15.1$MW/m^2 and $\dot{Q}_{rad} = 30.5$MW/m^2.

where $\dot{m}_p$ is the particle mass flow rate and

$$C_p = 12.22\left(53.999 + 7.851\times10^{-4}T_p - 5.868\times10^{5}T_p^{-2} - 127.5T_p^{-0.5} + 1.9376\times10^{-6}T_p^{2}\right)\text{J/gK}$$

is the particle specific heat capacity (Madelung et al., 1999). Equation 1 was solved for a time step of 1ms, with the particle velocity evaluated at a position of $r/D = 0.36$, i.e., corresponding to the experimentally measured average particle radial position under isothermal conditions. The heat flux and particle diameter used in the analytical model were selected to match the experimental measurements.

3. Results

Figure 4 presents the size distribution of the particle aggregates within the jet flow for the cases corresponding to radiative fluxes, $\dot{Q}_{rad} = 15.1$MW/m^2 and $\dot{Q}_{rad} = 30.5$MW/m^2. It can be seen that the particle size distribution is similar for both heat fluxes. This indicates that these heat fluxes do not affect particle size, i.e., the radiation at these heat fluxes do not promote aggregation or fracturing of the aggregates. For both cases, the modal value for particle

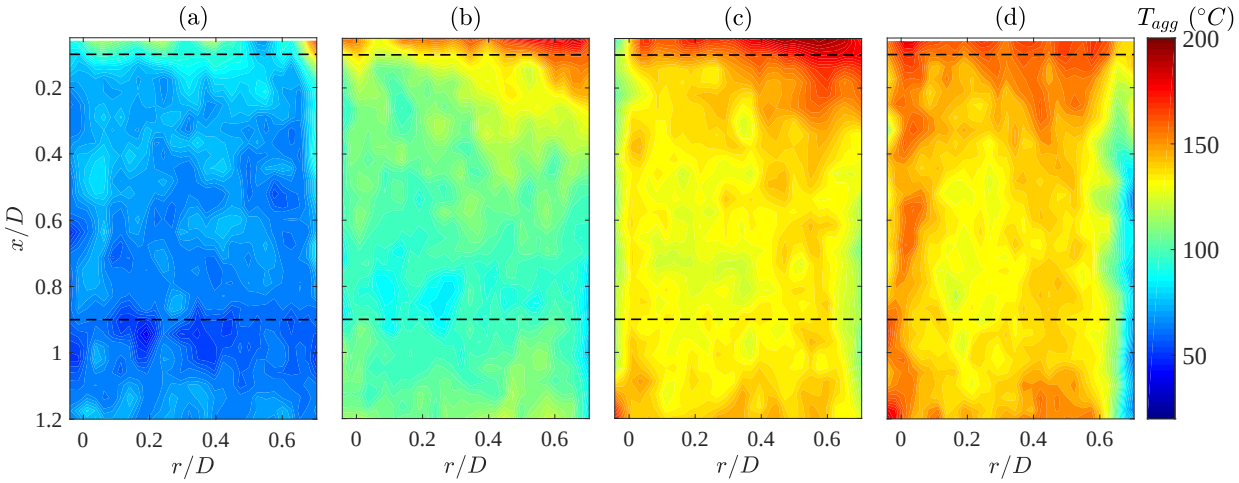

Figure 5: Mean particle temperature fields at 4 different radiative fluxes: (a) $\dot{Q}_{rad} = 6.2\text{MW/m}^2$, (b) $\dot{Q}_{rad} = 15.1\text{MW/m}^2$(c) $\dot{Q}_{rad} = 23.5\text{MW/m}^2$, (d) $\dot{Q}_{rad} = 30.5\text{MW/m}^2$. Black dotted lines indicate the start and end of the heating region.

aggregate diameter, $d_{agg} \approx 240\mu\text{m}$. This value is used as the nominal particle diameter in all remaining analyses, including the heat transfer model.

Figure 5 presents images of the distributions of mean (time-averaged) particle temperatures within the particle-laden jet for 4 different radiative fluxes, $\dot{Q}_{rad} = 6.2\text{MW/m}^2$, 15.1MW/m^2 23.5MW/m^2 and 30.5MW/m^2. It can be seen that the mean particle aggregate temperature increases with heat flux, as expected. However, for all cases of $\dot{Q}_{rad} > 0$, the measured increase in $\overline{T}_{agg}$ does not correlate with the spatial position of the radiatively-heated region, which is shown with the black dashed lines. That is, hot particles are found throughout the image, including within the region upstream from the heating region. The potential causes for hot particles being found upstream from the heated zone is inter-particle radiation and large-scale recirculation of hot particles from downstream of the heating region back upstream through the effects of buoyancy. For the higher values of heat flux, a radial influence of the radiation on particle temperatures is also evident, with two regions of local maxima of $\overline{T}_{agg}$ aligned approximately in the streamwise direction occurring at the jet centre, $r/D \approx 0$, and jet edge, $r/D \approx 0.45$. This can be observed from Figure 5(c) where $\dot{Q}_{rad} = 23.5\text{MW/m}^2$, and becomes more prominent in Figure 5(d) as $\dot{Q}_{rad}$ is increased to 30.5MW/m^2.

Figure 6 presents the experimentally measured mean particle aggregate temperature, $\overline{T}_{agg}$, averaged over the heating region as a function of the heating flux, $\dot{Q}_{rad}$. Also shown are the results from the analytical model (Equation 1) for a 240μm diameter particle agglomerate. It should be noted that the "error-bars" in the figure shows the maximum-minimum range of T_{agg} measured over 4000 single-shot measurements and is not indicative of the accuracy of the measurement. From this figure, it can be seen that the measured $\overline{T}_{agg}$ increases approximately linearly with heat flux for $\dot{Q}_{rad} \lesssim 20.6\text{MW/m}^2$. Within this range, the measured temperature increases with $\dot{Q}_{rad}$ at a rate that is approximately equal to the rate calculated with the analytical model. However, as $\dot{Q}_{rad}$ is increased above 20.6MW/m^2, the measured

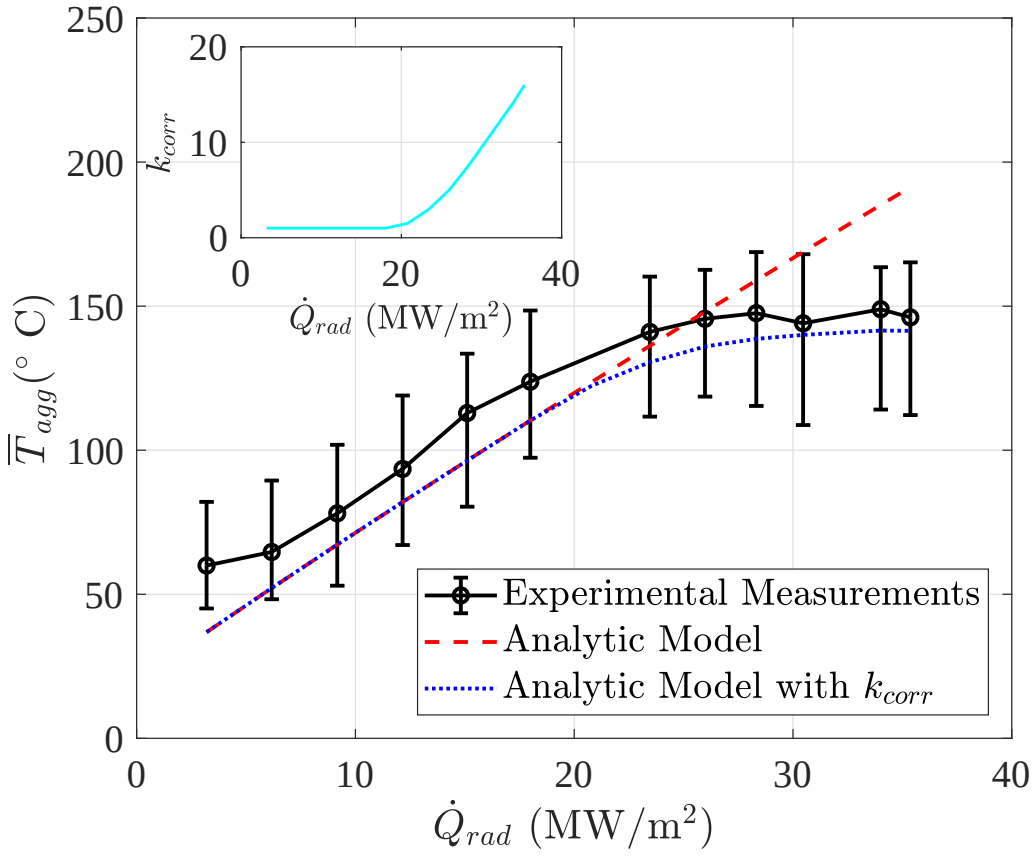

Figure 6: Mean temperature of all particle aggregates in all images, $\overline{T}_{agg}$, as a function of radiative heat flux. The red dashed line and the blue dotted line shows the theoretical behaviour of particle temperature of a 240µm diameter particle agglomerate calculated from the analytical model using Equation 1 without and with the usage of a correction factor, k_{corr}, to modify the effective convective heat transfer coefficient. The inset shows the calculated values of k_{corr} as a function of $\dot{Q}_{rad}$.

value of $\overline{T}_{agg}$ plateaus at approximately 150°C, in contrast to the predictions of the analytical model, which predicts a continuous linear increase within the examined radiative fluxes. This indicates that phenomena other than those accounted for in the analytical model are generated for heat fluxes above approximately 20MW/m^2.

The lower than expected particle temperatures may be due to a combination of increased particle cooling and/or lower particle heating, with the convective heat transfer mode being the most likely for the former because the radiative heat losses from the particles at these temperatures is relatively low. A higher than expected particle cooling rates may be due to the polydisperse size distribution of the particles, which has been theorised to more effectively transfer heat to the surrounding gas compared to monodispersed particles due different sized particles having different preferential concentration at various regions of the flow (Rahmani et al., 2018). This has been deduced to lead to increased heat losses from the particles, a more uniform heating of the gas phase, together with a more uniform gas phase temperature. However, this trend is likely to be independent of heat flux, so does not explain the critical threshold of

radiation flux that augments cooling.

In contrast, the role of buoyancy can provide a plausible explanation for the departure. The deduction that buoyancy is significant also provides a plausible qualitative explanation for the observation that hot particles are present upstream from the heating zone, whose upstream edge is located at $x/D = 0.2$ (Figure 5), as any buoyant force must act vertically upward to generate "lift" in the upstream direction. Buoyancy can be expected to augment the convective cooling on a particle by two potential mechanisms. Firstly, any buoyancy-induced lift will increase the local slip velocity, since buoyancy is in the opposite direction of the bulk flow. A second potential mechanism by which buoyancy can increase convective cooling is via the local generation of turbulence around the particle by the high flux radiation, as has been hypothesised from a DNS assessment by Rahmani et al. (2018). Since both of these effects are highly non-linear, we begin by assessing the magnitude of their combined influence on a lumped effective convective heat transfer coefficient, $h_{eff} = h k_{corr}$, where k_{corr} is the lumped correction factor, which is a function of $\dot{Q}_{rad}$. The values of k_{corr} as a function of $\dot{Q}_{rad}$, determined numerically, is presented in the inset to figure 6. This function is the series of values required to correct Equation 1 to more closely match the measured particle temperature, as shown by the blue dotted line in Figure 6. As can be seen, a value of k_{corr} that increases from 1 to approximately 16 as $\dot{Q}_{rad}$ increases from 20MW/m^2 to 35.5MW/m^2 results calculated values from the analytic model that more closely matches the overall trend of the experimental results. This implies that the combined effects of radiation-induced buoyancy and turbulence generation on particle-fluid heat transfer becomes significant at sufficiently high radiative heat fluxes.

Nevertheless, the magnitude of correction required, particularly at high heat flux where k_{corr} can exceed 10, suggests that increased particle to fluid convective heat loss is unlikely to be the only cause for the discrepancy between the modelled and measured results. Another reason for the discrepancy is a decreased particle residence time within the heating region of the flow. This could be caused by increased large scale motion within the flow, presumably through the effects of buoyancy and increased turbulence, such that particles are displaced away from the heating beam. This increased large-scale mixing is also expected to increase uniformity of the temperature distributions, consistent with the results presented in figure 5. Additionally, as the gas-phase velocity profile is expected to approximate a laminar pipe flow near the exit, a reduction in particle residence time could be caused by migration of particles from the jet edge, where the gas velocity is expected to be low, towards the jet axis, where the gas velocity is expected to be high. This is plausible because even at the highest heat flux examined here, $\dot{Q}_{rad} = 35.5$MW/m^2, a reduction of particle residence time within the heating region of $\approx$30% is sufficient to account for the difference between the experimental and calculated results. These results further highlight the significance of the effects of high flux radiation on the flow.

Figure 7 presents the joint probability distribution (weighted by aggregate volume fraction) of the relationship between particle aggregate diameter, d_{agg}, temperature, $\overline{T}_{agg}$, at two different fluxes, $\dot{Q}_{rad} = 15.1$MW/m^2 and 30.5MW/m^2 . Also plotted is the relationship between d_{agg} and $\overline{T}_{agg}$, as calculated using the analytical model (without use of the correction factor, k_{corr}) at these fluxes. The results show that the trends in the joint-PDFs do not vary significantly between the two heat flux values, consistent with the results presented in Figure 4. Larger particle aggregates were

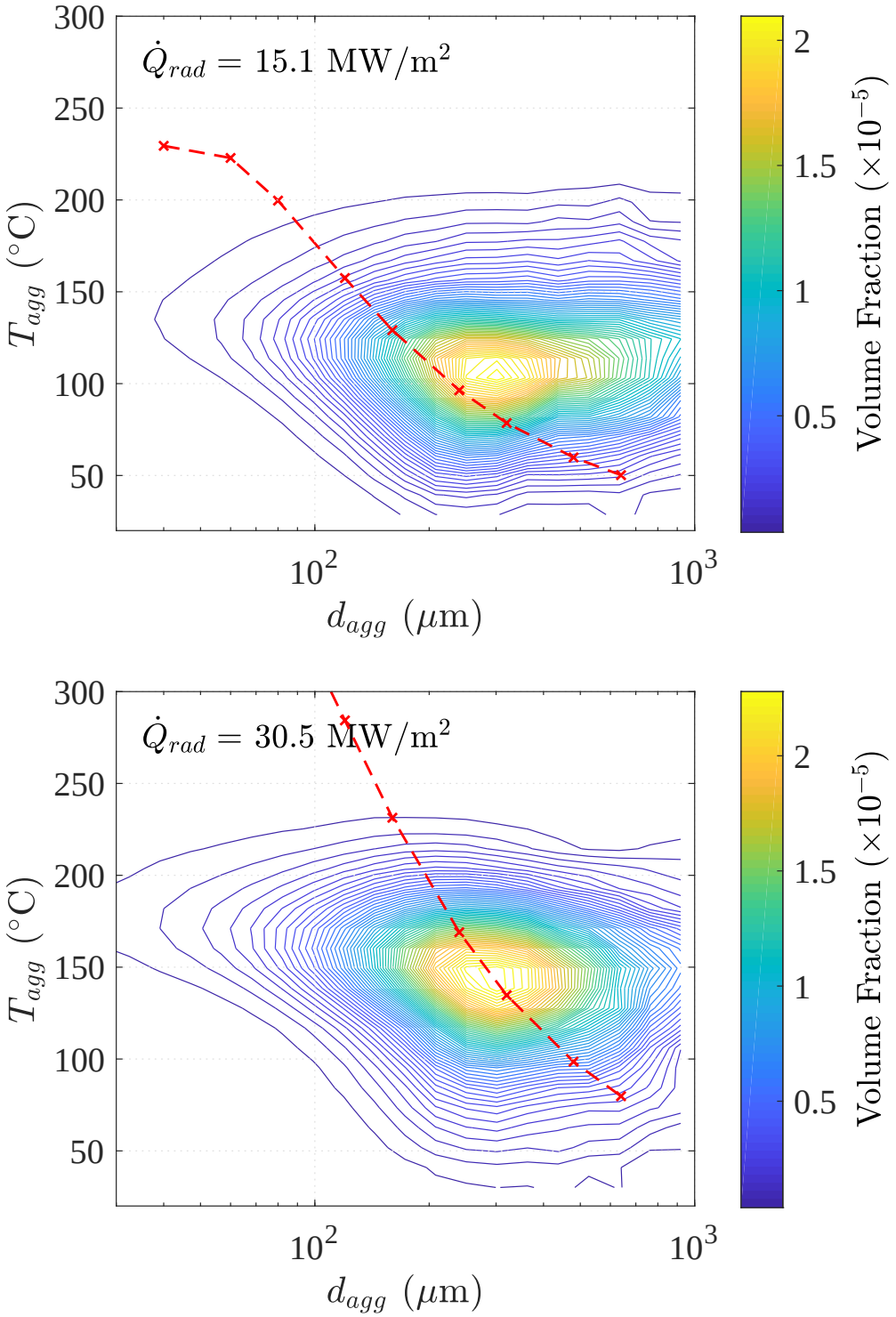

Figure 7: Joint probability density functions of particle aggregate diameter, d_{agg}, and aggregate temperature, $\overline{T}_{agg}$, for two radiative heat fluxes, $\dot{Q}_{rad} = 15.1$MW/m^2 and 30.5MW/m^2 . The red dotted line shows the results calculated from the analytical model (without use of the correction factor, k_{corr}).

found to typically have slightly lower temperatures than smaller aggregates, consistent with the trends predicted with the analytical model. However, the measurements reveal a significantly weaker dependence of $\overline{T}_{agg}$ on d_{agg} than that predicted with the analytical model. This is further evidence for the importance of radiation-induced increase to the convective cooling and large-scale mixing, which the analytical model does not take into account. As smaller particles are more likely to be influenced by the gas-phase flow, this effect may be more pronounced for the smaller particles. Furthermore, the analytic model assumes that the particles have a single, constant axial velocity, which was evaluated on the basis that the particles are, on average, preferentially distributed towards the jet edge (see section 2.1). However, this does not accurately represent the real flow, which has particles distributed across the jet, with particles closer to the jet axis having a higher axial velocity, and hence lower residence time within the heating region, than particles closer to the jet edge. Hence, the significantly lower than expected particle temperatures for smaller particles shown here may indicate that smaller particles tend to be distributed closer to the jet axis.

Figure 8 presents the radial distributions of (a) particle aggregate temperature, $\overline{T}_{agg}$, (b) number density relative to the bulk value, Θ/Θ_b , and (c) particle aggregate diameter, d_{agg}, for 4 values of $\dot{Q}_{rad}$. From Figure 8(a), a clear increase in $\overline{T}_{agg}$ with $\dot{Q}_{rad}$ can be seen for all cases with $\dot{Q}_{rad} \leq 23.5\text{MW/m}^2$. However, $\overline{T}_{agg}$ does not increase between $23.5\text{MW/m}^2 \leq \dot{Q}_{rad} \leq 30.5\text{MW/m}^2$ despite the increasing heat flux, consistent with Figure 6. Additionally, a local maxima in $\overline{T}_{agg}$ occurs close to jet edge, $r/D \approx 0.5$, for all values of $\dot{Q}_{rad}$. This can be partially explained by the radial distribution of particle number density, shown in Figure 8(b), which also shows a local maxima in Θ/Θ_b at $r/D \approx 0.5$. This trend in radial distribution of particle number density measured for the low heat flux case is consistent with the isothermal measurements by Lau and Nathan (2014), giving further confidence to the measurements. A possible explanation for preferential concentration of particles towards the jet edge is the effect of continuity, together with the expectation that the particle velocity profile should approximate a laminar pipe flow velocity profile. That is, particle concentration should increase in regions where the axial velocities are low. In any case, the results show strong correlations between particle number density and particle temperature. This correlation is attributed to particle-to-particle heat transfer, either direction via inter-particle radiation, or indirectly through convective heating of the local gas. In both mechanisms, heat transfer increases with particle number density.

The results presented in Figure 8(b) also show that the particle number density at $r/D \approx 0.5$ decreases as $\dot{Q}_{rad}$ is increased from 6.2MW/m^2 to 23.5MW/m^2, while the particle number density at $r/D \approx 0$ increases. This increase in particle number density close to the jet axis also correlated an additional local maxima in $\overline{T}_{agg}$ at $r/D \approx 0$ (Figure 8(a)). The presence of a local maxima of Θ/Θ_b at $r/D \approx 0$ indicates a possible particle migration from the jet edge towards the jet axis. This can be partially attributed to thermophoresis, an effect known to cause small particles to migrate towards regions of lower temperatures where large temperature gradients are present (Tsai et al., 2004). It should be noted that since the particles in the flow are poly-dispersed, this phenomenon likely only affects the smaller particles. This is supported by the measured radial distribution of particle diameter, presented in Figure 8(c), which shows that smaller particles are preferentially distributed towards $r/D \to 0$. Furthermore, this sub-figure also shows an

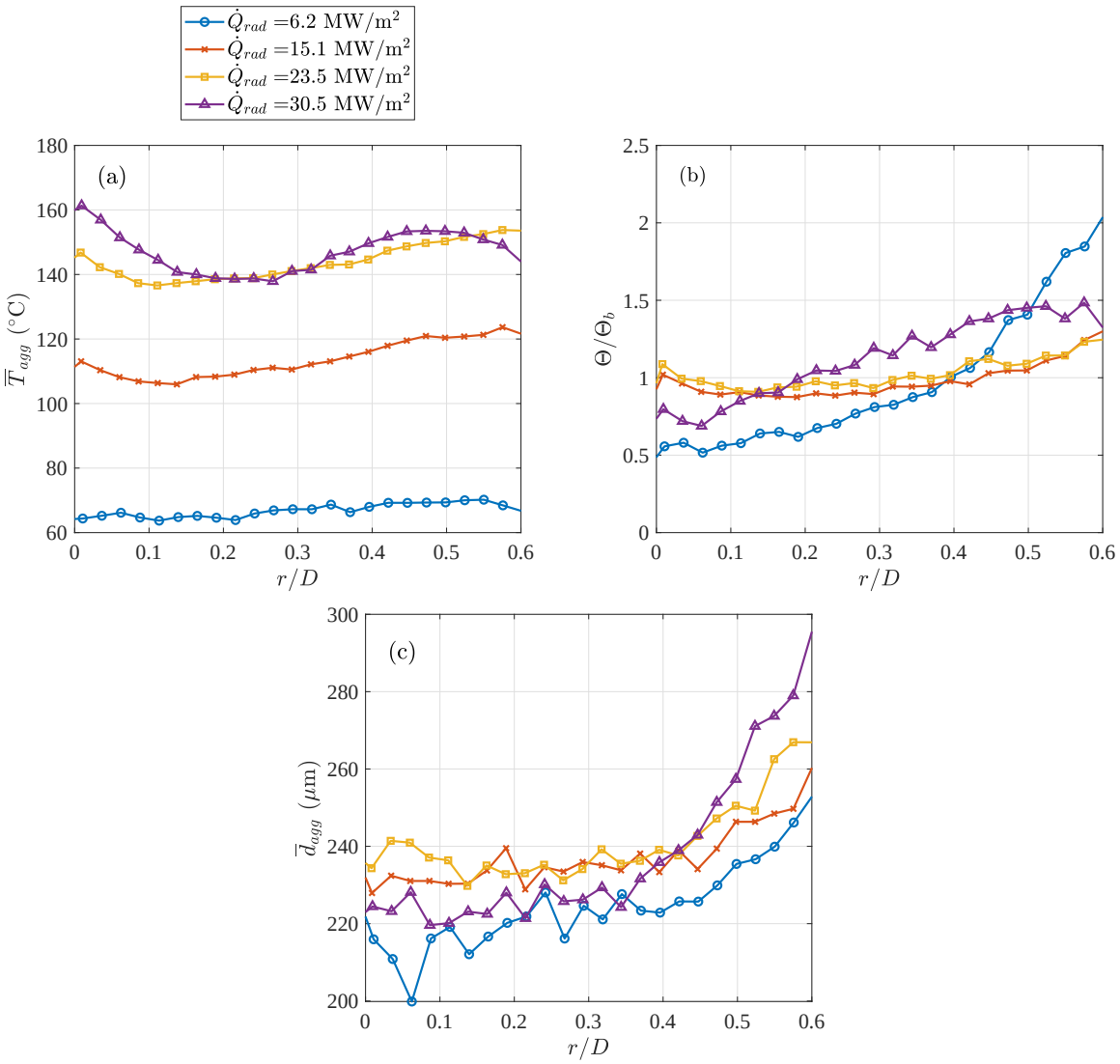

Figure 8: Radial distributions of (a) particle aggregate temperature, $\overline{T}_{agg}$, (b) number density relative to the bulk value, Θ/Θ_b , and (c) particle aggregate diameter, d_{agg}, at 4 values of $\dot{Q}_{rad}$. The radial distributions were obtained from the ensemble encompassing all axial positions within the measurement region. Note that all 3 sub-figures share the same legend.

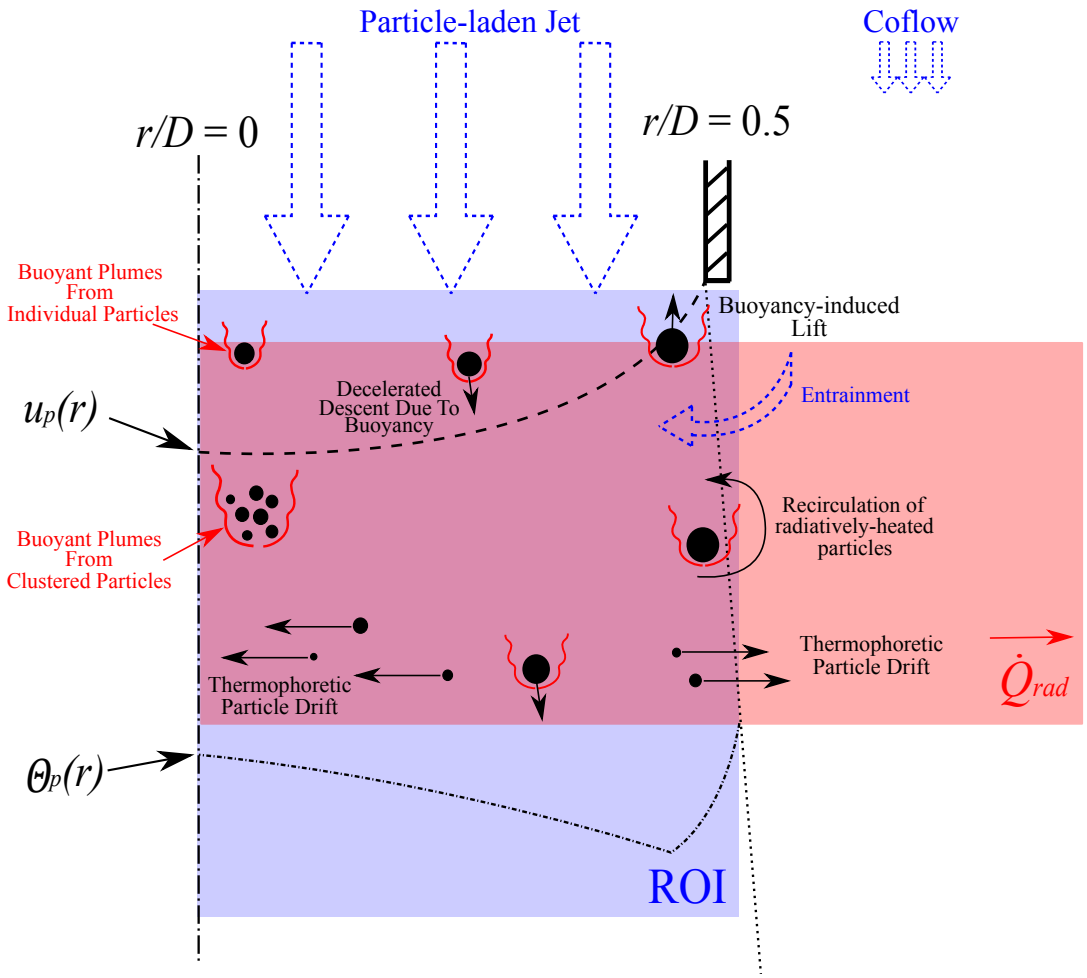

Figure 9: Illustration of the proposed driving mechanisms in a radiatively-heated particle-laden jet flow.

increase in the average particle diameter, $\overline{d}_{agg}$ at $r/D \approx 0.5$ with increasing $\dot{Q}_{rad}$. This is consistent with an increase in small particle migration away from the higher temperature region near to the jet edge due to thermophoresis. Further support of this can be found from Figure 9(a), where the local maxima in $\overline{T}_{agg}$ is found closer to $r/D \approx 0.4$ instead of $r/D \approx 0.5$ as are the case for the lower flux cases as the heat flux is further increased to $\dot{Q}_{rad} = 30.5\text{MW/m}^2$. In addition to small particle migration, the high temperature found along the jet centreline can also be attributed to its position as the furthest radial location from the ambient environment. That is, the particles that are the most insulated from the cold ambient environment are expected to retain their heat more readily than particles closer to the co-flow.

4. Discussion

Figure 9 presents a cartoon of the mechanisms that have been deduced to be induced by the strong radiative heat fluxes within the current particle-laden jet flow. It identifies radiation-induced buoyancy and turbulence generation as the

mechanisms deduced to increase large scale recirculation and mixing of the flow and particles. This effect is expected to be particularly significant in regions of low fluid axial velocity, i.e., at $r/D \rightarrow 0.5$, where buoyant forces are strong enough to overcome jet velocities and gravitational accelerations to cause upward particle drifts. These particles may be lifted to the zone above and upstream from the heating region, and may eventually return to the original direction of flow when sufficiently cooled, possibly inducing an additional recirculation within the flow. Additional evidence for the role of buoyancy in convecting hot particles upstream can be found in the observation that particles were found to be deposited on outside of the pipe upstream from the heating region, after, and only after, radiative heating with high fluxes ($\dot{Q}_{rad} \gtrsim 12.2$ MW/m^2). In addition, flow visualisation of the co-flow reconfirmed that no flow recirculation is present in the co-flow around the jet under isothermal conditions. Towards the jet axis, i.e. $r/D \rightarrow 0$, the buoyant forces are expected to increase slip velocity, slowing down the particle descent while increasing local turbulence and convective heat transfer. Additionally, regions were observed with high concentration of high particle temperatures. This suggests a possible regional influence of buoyancy-induced lift to a cluster of hot particles, with heat transferred by convection to region of warm gas. This is qualitatively consistent with the DNS results presented by Frankel et al. (2016). Taken together, the overall effect of the increased mixing, turbulence, large-scale recirculation is a more uniform distribution of temperature, and lower peak particle temperatures.

Additionally, the present measurements also provide support for thermophoresis, which in the present case, is expected to result in smaller particles migrating away from the region near the jet edge where the particle temperatures were found to be the highest. These potentially hot particles can be expected to migrate towards the jet axis, or outside of the jet where they may be recirculated back into the jet further upstream. Furthermore, even though the Reynolds number of the particle-laden flow was 1500, making it laminar within the pipe, the jet itself may transition to turbulence downstream. In such case, turbophoretic drifts in the radial direction may occur. Nevertheless, further research is required to confirm these complex mechanisms.

5. Conclusions

Detailed measurements of the particle temperature distribution in a radiatively heated particle-laden jet have revealed that complex mechanisms of radiation-induced buoyancy and turbulence become significant at sufficiently high radiation fluxes. While the measurements show that for radiative heat fluxes below $\dot{Q}_{rad} \lesssim 20.6$MW/m^2, particle aggregate temperatures, $\overline{T}_{agg}$, increase approximately linearly with heat flux consistent with the trends from an analytical model, for $\dot{Q}_{rad} \gtrsim 20.6$MW/m^2, the trends of $\overline{T}_{agg}$ depart significantly from expectation. It was deduced that for these higher heat fluxes, the convective heat transfer increases, while the particle residence time within the heating region decreases, due to the combined effects of radiation-induced buoyancy and turbulence. Buoyancy was also deduced to result in increased large-scale mixing and recirculation of the flow, such that individual particles or clusters of particles in regions of low average axial velocity can be lifted upstream of the flow, leading to additional complex flow mechanisms. This, in turn, leads to a more uniform temperature distribution within the flow, consistent with the

measurement of particles with high $\overline{T}_{agg}$ upstream of the heating region. Additional evidence for the deduced role of buoyancy is the observation that particles attach to the outside of the pipe when, and only when, the fluxes are sufficiently high.

It was also found that, for low heat flux cases ($\dot{Q}_{rad} \leq$6.2 MW/m^2), particle number density is higher in the outer regions of the jet ($r/D \rightarrow 0.5$), consistent with previous investigations. However, as heat flux is increased, the particle number density at the jet edge is seen to decrease, while simultaneously increasing at the jet centre, seemingly affecting smaller particles more than the larger ones. This trend is consistent with the influence of thermophoresis, a phenomenon in which smaller particles migrate to regions of lower temperatures in the presence of large temperature gradients, which in this case is directed either towards the jet axis ($r/D \rightarrow 0$), or outside of the jet. In addition, the distribution of particles was found to have a direct impact on particle aggregate temperatures, such that regions of high particle number density correlated with regions of high particle temperature, which suggests that inter-particle re-radiation is significant in this experiment. This results in the flow having two distinct regions of locally high particle temperature that are aligned approximately in the streamwise direction, one near the jet axis ($r/D \approx 0$) and one near the jet edge ($r/D \approx 0.5$).

These phenomena do not appear to have been observed before, making them worthy of further investigation.

Acknowledgments

We gratefully acknowledge support from the Australian Research Council through its Discovery grant 150102230 and Linkage Grant LE130100127. The financial support from the Institute of Minerals and Energy Resources (IMER) and the Faculty of Engineering, Computer & Mathematical Science (ECMS) at The University of Adelaide is also acknowledged.

References

Abram, C., Fond, B., Heyes, A.L., Beyrau, F., 2013. High-speed planar thermometry and velocimetry using thermographic phosphor particles. Applied Physics B: Lasers and Optics 111, 155–160.

Alwahabi, Z.T., Kueh, K.C.Y., Nathan, G.J., Cannon, S., 2016. Novel solid-state solar thermal simulator supplying 30,000 suns by fibre optical probe. Optics Express 24, A1444–A1453.

Baker, L., Frankel, A., Mani, A., Coletti, F., 2017. Coherent clusters of inertial particles in homogeneous turbulence. Journal of Fluid Mechanics 833, 364–398. doi:10.1017/jfm.2017.700.

Elghobashi, S., 2006. An updated classification map of particle-laden turbulent flows, in: Proc. of the IUTAM Symp. on Computational Multiphase Flow.

Fond, B., Abram, C., Heyes, A.L., Kempf, A.M., Beyrau, F., 2012. Simultaneous temperature, mixture fraction and velocity imaging in turbulent flows using thermographic phosphor tracer particles. Optics Express 20, 22118–22133.

Frankel, A., Pouransari, H., Coletti, F., Mani, A., 2016. Settling of heated particles in homogeneous turbulence. Journal of Fluid Mechanics 792, 869–893.

Grena, R., 2009. Thermal simulation of a single particle in a falling-particle solar receiver. Solar Energy 83, 1186–1199.

Han, D., Mungal, M.G., 2000. Simultaneous measurement of velocity and CH layer distribution in turbulent non-premixed flames. Proceedings of the Combustion Institute 28, 261–267.

Jovicic, G., Zigan, L., Will, S., Leipertz, A., 2015. Phosphor thermometry in turbulent hot gas flows applying Dy:YAG and Dy:Er:YAG particles. Measurement Science and Technology 26.

Kueh, K.C.Y., Lau, T.C.W., Nathan, G.J., Alwahabi, Z.T., 2018. Non-intrusive temperature measurement of particles in a fluidised bed heated by well-characterised radiation. International Journal of Multiphase Flow 100, 186–195.

Kueh, K.C.Y., Lau, T.C.W., Nathan, G.J., Alwahabi, Z.Y., 2017. Single-shot planar temperature imaging of radiatively heated fluidized particles. Optics Express 28, 28764–28775.

Lau, T.C.W., Frank, J.H., Nathan, G.J., 2019. Resolving the three-dimensional structure of particles that are aerodynamically clustered by a turbulent flow. Physics of Fluids 31, 071702. doi:10.1063/1.5110323.

Lau, T.C.W., Nathan, G.J., 2014. The influence of Stokes number on the velocity and concentration distributions in particle-laden jets. J. Fluid Mech. 757, 432–457.

Lau, T.C.W., Nathan, G.J., 2016. The effect of Stokes number on particle velocity and concentration distributions in a well-characterised, turbulent, co-flowing two-phase jet. J. Fluid Mech. 809, 72–110.

Lavieille, P., Delconte, A., Blondel, D., Lebouche, M., Lemoine, F., 2004. Non-intrusive temperature measurements using three-color laser-induced fluorescence. Experiments in Fluids 37, 706–716.

Madelung, O., Rössler, U., Schulz, M., 1999. Zinc oxide (ZnO) Debye temperature, heat capacity, density, melting point, vapor pressure, hardness, in: II-VI and I-VII Compounds: Semimagnetic Compounds. Springer-Verlag, pp. 1–5.

Monchaux, R., Bourgoin, M., Cartellier, A., 2012. Analyzing preferential concentration and clustering of inertial particles in turbulence. International Journal of Multiphase Flow 40, 1–18.

Montassier, N., Boulaud, D., Renoux, A., 1991. Experimental study of thermophoretic particle deposition in laminar tube flow. Journal of Aerosol Science 22, 677–687.

Ordóñez, F., Caliot, C., Bataille, F., Lauriat, G., 2014. Optimization of the optical particle properties for a high temperature solar particle receiver. Solar Energy 99, 299–311. doi:10.1016/j.solener.2013.11.014.

Rahmani, M., Geraci, G., Iaccarino, G., Mani, A., 2018. Effects of particle polydispersity on radiative heat transfer in particle-laden turbulent flows. International Journal of Multiphase Flow 104, 42–59. doi:10.1016/j.ijmultiphaseflow.2018.03.011.

Schunk, L.O., 2008. Solar thermal dissociation of Zinc Oxide Reaction Kinetics, Reactor Design, Experimentation, and Modeling. Ph.D. thesis. ETH Zurich.

Talbot, L., Cheng, R.K., Schefer, R.W., Willis, D.R., 1980. Thermophoresis of particles in a heated boundary layer. Journal of Fluid Mechanics 101, 737–758. doi:10.1017/s0022112080001905.

Tsai, C.J., Lin, J.S., Aggarwal, S.G., Chen, D.R., 2004. Thermophoretic deposition of particles in laminar and turbulent tube flows. Aerosol Science and Technology 38, 131–139. doi:10.1080/02786820490251358.

Zamansky, R., Coletti, F., Massot, M., Mani, A., 2014. Radiation induces turbulence in particle-laden fluids. Physics of Fluids 26, 071701. doi:10.1063/1.4890296.

Zamansky, R., Coletti, F., Massot, M., Mani, A., 2016. Turbulent thermal convection driven by heated inertial particles. Journal of Fluid Mechanics 809, 390–437. doi:10.1017/jfm.2016.630.

Chapter 8:

Conclusion and Recommendations for Future Work

8. Conclusion and Recommendation for Future Work

The present dissertation reports the development of non-intrusive, spatially and temporally-resolved particle temperature measurement techniques applicable in turbulent particle-laden flows subjected to high irradiation. Two techniques were developed as part of the scope of the present candidature, both of which were based on the laser-induced phosphorescent (LIP) technique. The techniques utilise the temperature-dependent properties of ZnO:Zn thermophosphors (TPs), where phosphorescent emission signals from the TP after excitation were used to infer the particle temperatures. The first of the techniques developed was a temporally-resolved, non-intrusive, area-averaged particle temperature measurement method. Particles were transported with dry air within an optically-accessible fluidised bed and heated with a well-defined source of high-flux radiation from a 3kW solid-state solar thermal simulator radiation to achieve heating rates in order 23,000 °C/s. Confidence in the method was obtained by verifying internal consistency between the energy absorbed by the particles, the temperature rise of the gas phase, which was measured with thermocouples, and taking into account variability of the particle mass loading in the system. The second technique developed was a single-shot, planar temperature imaging technique with a spatial resolution of 51mm/pixel. Particle temperatures were derived from arrays of intensity ratio calculated by dividing two images, each with an area of 15mm × 10.5mm, on a pixel-by-pixel basis. The normalized temperature distribution within an individual particle agglomerate was found to be up to ± 4%, which was attributed to ICCD sensor noise so that the mean temperature is well resolved. The scope of the current research also includes characterising the performance of the recently-developed Solid-State Solar Thermal Simulator (SSSTS), where information from the characterisation campaign were used to incorporate the SSSTS into all experiments of the present thesis.

Additionally, new understanding about the effect of radiative heating on the distributions of particle temperature, size and concentration (number density) in a laminar, radiatively-heated particle-laden jet was obtained as part of the dissertation. The investigation was performed in a laminar particle-laden jet flow and compared against a simplified first-order heat transfer model. Figure 8-1 presents the proposed driving mechanisms in a radiatively-heated particle-laden jet flow, where some of the key findings of this investigation include:

- At low heat fluxes ($\dot{Q}_{rad} \lesssim 20.6$ MW/m^2), particle aggregate temperatures, $\bar{T}_{agg}$, increase approximately linearly with heat flux consistent with the trends from an analytical model;
- At higher heat fluxes ($\dot{Q}_{rad} \gtrsim 20.6$ MW/m^2), the measured $\bar{T}_{agg}$ trend departs from the analytical model, plateauing at approximately 150°C. This is attributed to the combined influences of increased convective cooling through the effects of buoyancy and radiation-induced turbulence together with decreased particle residence time within the heating region due to increased large-scale mixing;
- $\bar{T}_{agg}$ is directly affected by the local particle volume fraction, such that they are correlated, suggesting that inter-particle re-radiation is significant in this experiment;
- Preferential concentration of particles towards the jet edge for $\dot{Q}_{rad} \lesssim 6.2$ MW/m^2 was found in the present study, consistent with previous investigations;
- As heat flux is increased $\dot{Q}_{rad} \gtrsim 6.2$ MW/m^2, the particle number density at the jet edge is seen to decrease, while simultaneously increasing at the jet centre, seemingly affecting smaller particles more than the larger ones. This trend is consistent with the influence of thermophoresis;
- For heat fluxes, $\dot{Q}_{rad} \gtrsim 6.2$ MW/m^2, complex phenomenon of buoyancy-induced large-scale recirculation within the weak co-flow leads to hot particles being detected upstream of the heating zone. Regions of high particle temperature occur in two distinct regions that are aligned approximately in the streamwise direction – one towards the jet axis and the other toward the jet edge. This observation suggests that the combination of buoyancy and thermophoresis has a significant influence on the flow field under these conditions.

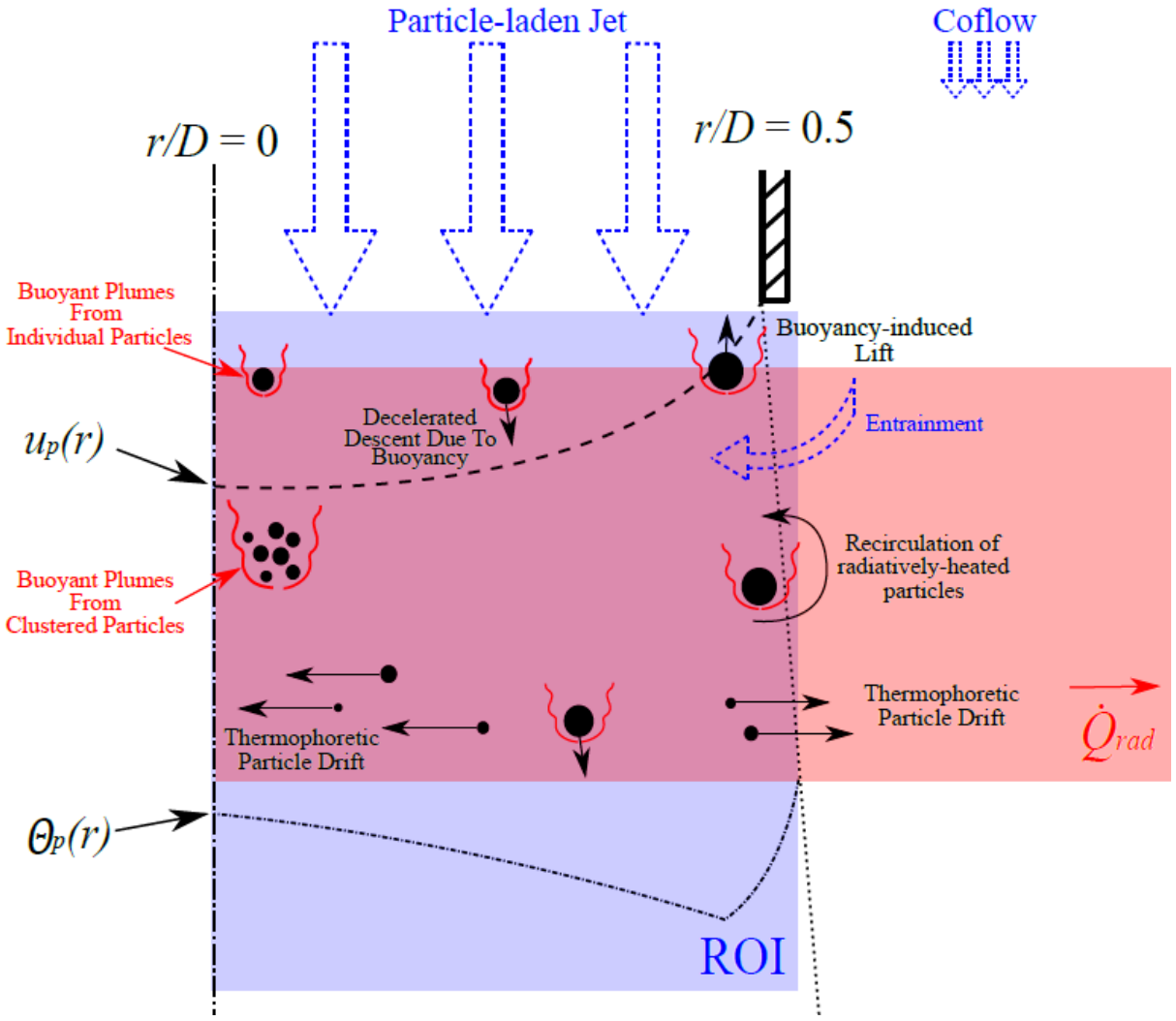

Figure 8-1: Illustration of the proposed driving mechanisms in a radiatively-heated particle-laden jet flow.

In conclusion, the results obtained in this thesis have met the aim of aiding in the advancements of heat and mass transfer in particle-laden flows by developing a non-intrusive, direct temperature measurement of particles applicable in turbulent particle-laden which is spatially and temporally resolved. It also provides insights on the influence of radiative heating on complex, naturally occurring phenomenon such as thermophoresis and buoyancy on particle-laden flows.

It is recommended that future work in particle-laden flows incorporates simultaneous measurements of particle temperature, gas temperature, and flow velocimetry to obtain a more complete understanding of the influence of high irradiation on such flows. The outcome of such study would inform the exact trajectory of particles under the influence of buoyancy and thermophoresis when heated, which this dissertation lacks. Future thermometry developed should also consider multiple scattering, particularly in cases where laser beam is close to the measurement region. Additionally, it would provide knowledge of the extent of particle-gas temperature disparity needed for such phenomena to occur. It is also recommended that for studies with a downward-facing jet flow, the imaging region be expanded to enable monitoring above the pipe-exit as particle depositions were observed on the outside of the pipe when fluxes were sufficiently high. Another recommendation is to vary the Stokes number at which the investigations were performed, particularly within the range where Stokes number has a strong influence on particle clustering. This will provide useful information on the effect of particle clustering on the temperature distributions within the flow.

References

ABRAM, C., FOND, B., HEYES, A. L. & BEYRAU, F. 2013. High-speed planar thermometry and velocimetry using thermographic phosphor particles. *Applied Physics B: Lasers and Optics,* 111**,** 155-160.

AGARWAL, P. K. 1991. Transport phenomena in multi-particle systems—IV. Heat transfer to a large freely moving particle in gas fluidized bed of smaller particles. *Chemical Engineering Science,* 46**,** 1115-1127.

ALDÉN, M., OMRANE, A., RICHTER, M. & SARNER, G. 2011. Thermographic phosphors for thermometry: A survey of combustion applications. *Progress in Energy and Combustion Science,* 37**,** 422-461.

ALWAHABI, Z. T., KUEH, K. C. Y., NATHAN, G. J. & CANNON, S. 2016. Novel solid-state solar thermal simulator supplying 30,000 suns by a fibre optical probe. *Optics Express,* 24**,** A1444-A1453.

ANOOP, K. B., SUNDARARAJAN, T. & DAS, S. K. 2009. Effect of particle size on the convective heat transfer in nanofluid in the developing region. *International Journal of Heat and Mass Transfer,* 52**,** 2189-2195.

ARCEN, B., TANIÈRE, A. & KHALIJ, M. 2012. Heat transfer in a turbulent particle-laden channel flow. *International Journal of Heat and Mass Transfer,* 55**,** 6519-6529.

BAKER, L., FRANKEL, A. MANI, A, COLETTI, F. 2017. Coherent clusters of inertial particles in homogeneous turbulence. *Journal of Fluid Mechanics,* 833, 364-398.

BALACHANDAR, S. & EATON, J. K. 2010. Turbulent Dispersed Multiphase Flow. *Annual Review of Fluid Mechanics,* 42**,** 111-133.

BANKO, A. J., KIM, J. H., VILLAFANE, L. & EATON, J. K. Temperature Statistics in a Radiatively Heated Particle-laden Turbulent Square Duct Flow. 11th International Symposium on Turbulence and Shear Flow Phenomena (TSFP11), 2019 Southampton, UK.

BASU, P. 1990. Heat transfer in high temperature fast fluidized beds. *Chemical Engineering Science,* 45**,** 3123-3136.

BIYIKLI, S. 2015. Predicting Freeboard Heat Transfer by Using Empirical Correlations in High Temperature Fluidized Beds (23). *International Journal of Green Energy,* 12**,** 303-308.

BIZARRI, G. & MOINE, B. 2005. On phosphor degradation mechanism: thermal treatment effects. *Journal of Luminescence,* 113**,** 199-213.

BRAIBANTI, M., VIGOLO, D. & PIAZZA, R. 2008. Does Thermophoretic Mobility Depend on Particle Size? *Physical Review Letters,* 100**,** 108303.

BRÜBACH, J., DREIZLER, A. & JANICKA, J. 2007. Gas compositional and pressure effects on thermographic phosphor thermometry. *Measurement Science and Technology,* 18**,** 764-770.

BRÜBACH, J., PFLITSCH, C., DREIZLER, A. & ATAKAN, B. 2013. On surface temperature measurements with thermographic phosphors: A review. *Progress in Energy and Combustion Science,* 39**,** 37-60.

BRUBACH, J., ZETTERBERG, J., OMRANE, A., LI, Z. S., ALDÉN, M. & DREIZLER, A. 2006. Determination of surface normal temperature gradients using thermographic phosphors and filtered Rayleigh scattering. *Applied Physics B: Lasers and Optics,* 84**,** 537-541.

CHAROGIANNIS, A. & BEYRAU, F. 2013. Laser induced phosphorescence imaging for the investigation of evaporating liquid flows. *Experiments in Fluids,* 54**,** 1-15.

CHEN, H., CHEN, Y., HSIEH, H.-T. & SIEGEL, N. 2006. Computational Fluid Dynamics Modeling of Gas-Particle Flow Within a Solid-Particle Solar Receiver. *Journal of Solar Energy Engineering,* 129**,** 160-170.

COLLIER, A. P., HAYHURST, A. N., RICHARDSON, J. L. & SCOTT, S. A. 2004. The heat transfer coefficient between a particle and a bed (packed or fluidised) of much larger particles. *Chemical Engineering Science,* 59**,** 4613-4620.

COZZANI, V., PETARCA, L., PINTUS, S. & TOGNOTTI, L. 1995. Ignition and combustion of single, levitated char particles. *Combustion and Flame,* 103**,** 181-193.

DENHOLM, P., WAN, Y.-H., HUMMON, M. & MEHOS, M. 2013. An Analysis of Concentrating Solar Power with Thermal Energy Storage in a California 33% Renewable Scenario. *In:* NREL (ed.). Colorado.

DUHR, S. & BRAUN, D. 2006. Thermophoretic Depletion Follows Boltzmann Distribution. *Physical Review Letters,* 96**,** 168301.

ELGHOBASHI, S. 1994. On predicting particle-laden turbulent flows. *Applied Scientific Research (The Hague),* 52**,** 309-329.

ELGHOBASHI, S. An Updated Classification Map of Particle-Laden Turbulent Flows. *In:* BALACHANDAR, S. & PROSPERETTI, A., eds. IUTAM Symposium on Computational Approaches to Multiphase Flow, 2006// 2006 Dordrecht. Springer Netherlands, 3-10.

ELPERIN, T., KLEEORIN, N., L'VOV, V. S., ROGACHEVSKII, I. & SOKOLOFF, D. 2002. Clustering instability of the spatial distribution of inertial particles in turbulent flows. *Physical Review E,* 66**,** 036302.

FAN, J., ZHAO, H. & CEN, K. 1996. Particle concentration and size measurements in two-phase turbulent coaxial jets. *Chemical Engineering Communications,* 156**,** 115-129.

FEIST, J. P., HEYES, A. L. & SEEFELDT, S. 2003. Oxygen quenching of phosphorescence from thermographic phosphors. *Measurement Science and Technology,* 14**,** N17-N20.

FERRANTE, A. & ELGHOBASHI, S. 2003. On the physical mechanisms of two-way coupling in particle-laden isotropic turbulence. *Physics of Fluids,* 15**,** 315-329.

FESSLER, J. R., KULICK, J. D. & EATON, J. K. 1994. Preferential concentration of heavy particles in a turbulent channel flow. *Physics of Fluids,* 6**,** 3742-3749.

FINCKE, J. R., JEFFERY, C. L. & SPJUT, R. E. 1988. MEASUREMENT OF THE EMISSIVITY OF SMALL PARTICLES AT ELEVATED-TEMPERATURES. *Optical Engineering,* 27**,** 684-690.

FINCKE, J. R., SWANK, W. D., JEFFERY, C. L. & MANCUSO, C. A. 1993. Simultaneous measurement of particle size, velocity and temperature. *Measurement Science and Technology,* 4**,** 559-565.

FLETCHER, T. H. 1989. Time-Resolved Temperature Measurements of Individual Coal Particles During Devolatilization. *Combustion Science and Technology,* 63**,** 89-105.

FOND, B., ABRAM, C., HEYES, A. L., KEMPF, A. M. & BEYRAU, F. 2012. Simultaneous temperature,mixture fraction and velocity imaging in turbulent flows using thermographic phosphor tracer particles. *Optics Express,* 20**,** 22118-22133.

FOSS, W. R. & JAMES DAVIS, E. 1996. TRANSIENT LASER HEATING OF SINGLE SOLID MICROSPHERES. *Chemical Engineering Communications,* 152-153**,** 113-138.

FRANKEL, A., POURANSARI, H., COLETTI, F. & MANI, A. 2016. Settling of heated particles in homogeneous turbulence. *Journal of Fluid Mechanics,* 792**,** 869-893.

GIL, A., MEDRANO, M., MARTORELL, I., LÁZARO, A., DOLADO, P., ZALBA, B. & CABEZA, L. F. 2010. State of the art on high temperature thermal energy storage for power generation. Part 1—Concepts, materials and modellization. *Renewable and Sustainable Energy Reviews,* 14**,** 31-55.

GOTO, S. & VASSILICOS, J. 2006. Self-similar clustering of inertial particles and zero-acceleration points in fully developed two-dimensional turbulence. *Physics of Fluids,* 18**,** 115103.

GOTO, S. & VASSILICOS, J. 2008. Sweep-stick mechanism of heavy particle clustering in fluid turbulence. *Physical review letters,* 100**,** 054503.

GRENA, R. 2009. Thermal simulation of a single particle in a falling-particle solar receiver. *Solar Energy,* 83**,** 1186-1199.

GUALTIERI, P., PICANO, F., SARDINA, G. & CASCIOLA, C. M. 2013. Clustering and turbulence modulation in particle-laden shear flows. *Journal of Fluid Mechanics,* 715**,** 134-162.

HAN, D. & MUNGAL, M. G. 2000. Simultaneous measurement of velocity and CH layer distribution in turbulent non-premixed flames. *Proceedings of the Combustion Institute,* 28**,** 261-267.

HASEGAWA, R., SAKATA, I., YANAGIHARA, H., JOHANSSON, B., OMRANE, A. & ALDÉN, M. 2007. Two-dimensional gas-phase temperature measurements using phosphor thermometry. *Applied Physics B: Lasers and Optics,* 88**,** 291-296.

HE, C. & AHMADI, G. 1998. Particle Deposition with Thermophoresis in Laminar and Turbulent Duct Flows. *Aerosol Science and Technology,* 29**,** 525-546.

HEYES, A. L., SEEFELDT, S. & FEIST, J. P. Two-colour phosphor thermometry for surface temperature measurement. Colour and Design in the Natural and Man-Made Worlds, 2006. Elsevier Ltd, 257-265.

HO, C. K. & IVERSON, B. D. 2014. Review of high-temperature central receiver designs for concentrating solar power. *Renewable and Sustainable Energy Reviews,* 29**,** 835-846.

IRENA 2018. Renewable Power Generation Costs in 2017. *International Renewawble Energy Agency*.

JENKINS, T. P., WU, F. & TURNER, K. I. On the development of flow thermometry imaging for high temperatures using thermographic phosphors. 50th AIAA Aerospace Sciences Meeting Including the New Horizons Forum and Aerospace Exposition, January 9, 2012 - January 12, 2012, 2012 Nashville, TN, United states. American Institute of Aeronautics and Astronautics Inc.

JOVICIC, G., ZIGAN, L., WILL, S. & LEIPERTZ, A. 2015. Phosphor thermometry in turbulent hot gas flows applying Dy:YAG and Dy:Er:YAG particles. *Measurement Science and Technology,* 26.

KATOSHEVSKI, D., ZHAO, B., ZISKIND, G. & BAR-ZIV, E. 2001. Experimental study of the drag force acting on a heated particle. *Journal of Aerosol Science,* 32**,** 73-86.

KOHSE-HÖINGHAUS, K., BARLOW, R. S., ALDÉN, M. & WOLFRUM, J. 2005. Combustion at the focus: laser diagnostics and control. *Proceedings of the Combustion Institute,* 30**,** 89-123.

KOIZUMI, H., UMEMURA, Y., HANDO, S. & SUZUKI, K. 2010. Heat transfer performance and the transition to chaos of mixed convection around an isothermally heated sphere placed in a uniform, downwardly directed flow. *International Journal of Heat and Mass Transfer,* 53**,** 2602-2614.

KOSINSKI, P., BALAKIN, B. V., MIDDHA, P. & HOFFMANN, A. C. 2014. Collisions between particles in multiphase flows: Focus on contact mechanics and heat conduction. *International Journal of Heat and Mass Transfer,* 70**,** 674-687.

KUEH, K. C. Y., LAU, T. C. W., NATHAN, G. J. & ALWAHABI, Z. T. 2017. Single-shot planar temperature imaging of radiatively heated fluidized particles. *Optics Express,* 25**,** 28764-28775.

KUEH, K. C. Y., LAU, T. C. W., NATHAN, G. J. & ALWAHABI, Z. T. 2018. Non-intrusive temperature measurement of particles in a fluidised bed heated by well-characterised radiation. *International Journal of Multiphase Flow,* 100**,** 186-195.

KURAVI, S., TRAHAN, J., GOSWAMI, D. Y., RAHMAN, M. M. & STEFANAKOS, E. K. 2013. Thermal energy storage technologies and systems for concentrating solar power plants. *Progress in Energy and Combustion Science,* 39**,** 285-319.

LAU, T. C. W. & NATHAN, G. J. 2014. Influence of Stokes number on the velocity and concentration distributions in particle-laden jets. *Journal of Fluid Mechanics,* 757**,** 432-457.

LAU, T. C. W. & NATHAN, G. J. 2016. The effect of Stokes number on particle velocity and concentration distributions in a well-characterised, turbulent, co-flowing two-phase jet. *Journal of Fluid Mechanics,* 809**,** 72-110.

LAU, T. C. W. & NATHAN, G. J. 2017. A method for identifying and characterising particle clusters in a two-phase turbulent jet. *International Journal of Multiphase Flow,* 88**,** 191-204.

LAU, T. C. W. & FRANKEL, J. H., NATHAN, G. J. 2019. Resolving the three-dimensional structure of particles that are aerodynamically clustered by a turbulent flow. *Physics of Fluids*, 31, 071702. doi: 10.1063/1.5110323.

LAWRENCE, M., ZHAO, H. & GANIPPA, L. 2013. Gas phase thermometry of hot turbulent jets using laser induced phosphorescence. *Optics Express,* 21**,** 12260-12281.

LIN, J. 1999. Temperature analysis of the powder streams in coaxial laser cladding. Optics & Laser Technology, 31, 565-570.

LINDEN, J., TAKADA, N., JOHANSSON, B., RICHTER, M. & ALDÉN, M. 2009. Investigation of potential laser-induced heating effects when using thermographic phosphors for gas-phase thermometry. *Applied Physics B: Lasers and Optics,* 96**,** 237-240.

LIU, W., ZHANG, J., ZHOU, M. & WANG, Y. 2012. The thermal and irradiation degradation mechanisms of Eu 2+,Mn2+ co-doped BaMgAl10O17 phosphor. *Science China: Physics, Mechanics and Astronomy,* 55**,** 1757-1762.

LONGMIRE, E. K. & EATON, J. K. 1992. Structure of a particle-laden round jet. *Journal of Fluid Mechanics,* 236**,** 217-257.

LÜBBEN, J. F., MUND, C., SCHRADER, B. & ZELLNER, R. 1999. Uncertainties in temperature measurements of optically levitated single aerosol particles by Raman spectroscopy. *Journal of Molecular Structure,* 480–481**,** 311-316.

LUNGU, M., WANG, J. D. & YANG, Y. R. 2015. Numerical simulations of flow structure and heat transfer in a central jet bubbling fluidized bed. *Powder Technology,* 269**,** 139-152.

MADELUNG, O., RÖSSLER, U., SCHULZ, M. 1999. Zinc oxide (ZnO) Debye temperature, heat capacity, density, melting point, vapor pressure, hardness. *In:* MADELUNG, O., RÖSSLER, U. & SCHULZ, M. (eds.) *II-VI and I-VII Compounds; Semimagnetic Compounds.* Berlin, Heidelberg: Springer Berlin Heidelberg.

MANN, M., JAINSKI, C., EULER, M., BOHM, B. & DREIZLER, A. 2014. Transient flame-wall interactions: Experimental analysis using spectroscopic temperature and CO concentration measurements. *Combustion and Flame,* 161**,** 2371-2386.

MINCUZZI, G., SCHULZ-RUHTENBERG, M., VESCE, L., REALE, A., DI CARLO, A., GILLNER, A. & BROWN, T. M. 2014. Laser processing of TiO2 films for dye solar cells: a thermal, sintering, throughput and embodied energy investigation. *Progress in Photovoltaics: Research and Applications,* 22**,** 308-317.

MOGRABI, E., ZISKIND, G., KATOSHEVSKI, D. & BAR-ZIV, E. 2002. Experimental study of the forces associated with mixed convection from a heated sphere at small Reynolds

and Grashof numbers. Part II: Assisting and opposing flows. *International Journal of Heat and Mass Transfer,* 45**,** 2423-2430.
MOKHTARIFAR, N., SAFFARAVAL, F., SAFFAR-AVVAL, M., MANSOORI, Z. & SIAMIE, A. 2015. Experimental Modeling of Gas-Solid Heat Transfer in a Pipe with Various Inclination Angles. *Heat Transfer Engineering,* 36**,** 113-122.
MONAZAM, E. R. & MALONEY, D. J. 1992. Temperature transients associated with pulsed heating of single particles. *Journal of Applied Physics,* 71**,** 2552-2559.
MONAZAM, E. R., MALONEY, D. J. & LAWSON, L. O. 1989. Measurements of heat capacities, temperatures, and absorptivities of single particles in an electrodynamic balance. *Review of Scientific Instruments,* 60**,** 3460-3465.
MONCHAUX, R., BOURGOIN, M. & CARTELLIER, A. 2012. Analyzing preferential concentration and clustering of inertial particles in turbulence. *International Journal of Multiphase Flow,* 40**,** 1-18.
MONTASSIER, N., BOULAUD, D. & RENOUX, A. 1991. Experimental study of thermophoretic particle deposition in laminar tube flow. *Journal of Aerosol Science,* 22**,** 677-687.
MÜLLER, R., HAEBERLING, P. & PALUMBO, R. D. 2006. Further advances toward the development of a direct heating solar thermal chemical reactor for the thermal dissociation of ZnO(s). *Solar Energy,* 80**,** 500-511.
OMRANE, A., PETERSSON, P., ALDÉN, M. & LINNE, M. A. 2008. Simultaneous 2D flow velocity and gas temperature measurements using thermographic phosphors. *Applied Physics B: Lasers and Optics,* 92**,** 99-102.
ORDONEZ, F., CALIOT, C., BATAILLE, F. & LAURIAT, G. 2014. Optimization of the optical particle properties for a high temperature solar particle receiver. *Solar Energy,* 99**,** 299-311.
PARMAR, M. S. & HAYHURST, A. N. 2002. The heat transfer coefficient for a freely moving sphere in a bubbling fluidised bed. *Chemical Engineering Science,* 57**,** 3485-3494.
PETRASCH, J., CORAY, P., MEIER, A., BRACK, M., HÄBERLING, P., WUILLEMIN, D. & STEINFELD, A. 2006. A Novel 50kW 11,000 suns High-Flux Solar Simulator Based on an Array of Xenon Arc Lamps. *Journal of Solar Energy Engineering,* 129**,** 405-411.
PUSTOVALOV, V. K. 2005. Theoretical study of heating of spherical nanoparticle in media by short laser pulses. *Chemical Physics,* 308**,** 103-108.
RABENSTEIN, F. & LEIPERTZ, A. 1997. Two-dimensional temperature determination in the exhaust region of a laminar flat-flame burner with linear Raman scattering. *Applied Optics,* 36**,** 6989-6996.
RAHMANI, M., GERACI, G., IACCARINO, G. & MANI, A. 2018. Effects of particle polydispersity on radiative heat transfer in particle-laden turbulent flows. *International Journal of Multiphase Flow,* 104**,** 42-59.
RASSAT, S. D. & DAVIS, E. J. 1994. Temperature Measurement of Single Levitated Microparticles Using Stokes/Anti-Stokes Raman Intensity Ratios. *Applied Spectroscopy,* 48**,** 1498-1505.
ROUSON, D. W. I. & EATON, J. K. 2001. On the preferential concentration of solid particles in turbulent channel flow. *Journal of Fluid Mechanics,* 428**,** 149-169.
SARNER, G., RICHTER, M. & ALDÉN, M. 2008. Investigations of blue emitting phosphors for thermometry. *Measurement Science and Technology,* 19.
SCHUNK, L. O. 2008. *Solar thermal dissociation of Zinc Oxide Reaction Kinetics, Reactor Design, Experimentation, and Modeling.* Doctor of Sciences Doctoral Thesis, ETH Zürich.

SCOTT, S. A., DAVIDSON, J. F., DENNIS, J. S. & HAYHURST, A. N. 2004. Heat Transfer to a Single Sphere Immersed in Beds of Particles Supplied by Gas at Rates above and below Minimum Fluidization. *Industrial & Engineering Chemistry Research,* 43**,** 5632-5644.

SEYFRIED, H., SARNER, G., OMRANE, A., RICHTER, M., SCHMIDT, H. & ALDEN, M. 2005. Optical diagnostics for characterisation of a full-size fighter-jet afterburner. *ASME Turbo Expo 2005: Power for land, sea, and air.* Reno, Nevada, USA.

SPJUT, R. E., SAROFIM, A. F. & LONGWELL, J. P. 1985. Laser heating and particle temperature measurement in an electrodynamic balance. *Langmuir,* 1**,** 355-360.

SQUIRES, K. D. & EATON, J. K. 1991. Preferential concentration of particles by turbulence. *Physics of Fluids A: Fluid Dynamics,* 3**,** 1169-1178.

STEINFELD, A. & PALUMBO, R. 2001. Solar thermochemical process technology. *Encyclopedia of Physical Science & Technology,* 15**,** 237-256.

STEINFELD, A. & SCHUBNELL, M. 1993. Optimum aperture size and operating temperature of a solar cavity-receiver. *Solar Energy,* 50**,** 19-25.

TALBOT, L., CHENG, R. K., SCHEFER, R. W. & WILLIS, D. R. 1980. Thermophoresis of particles in a heated boundary layer. *Journal of Fluid Mechanics,* 101**,** 737-758.

TANG, X., XU, S. & WANG, X. 2013. Thermal probing in single microparticle and microfiber induced near-field laser focusing. *Optics Express,* 21**,** 14303-14315.

TRIBELSKY, M. I., MIROSHNICHENKO, A. E., KIVSHAR, Y. S., LUK'YANCHUK, B. S. & KHOKHLOV, A. R. 2011. Laser Pulse Heating of Spherical Metal Particles. *Physical Review X,* 1**,** 1-9.

TRIPATHI, A., VAUGHN, C. L., MASWADEH, W. & MEUZELAAR, H. L. C. 2002. Measurement and modeling of individual carbonaceous particle temperature profiles during fast CO2 laser heating: Part 2. Coals. *Thermochimica Acta,* 388**,** 199-213.

TSAI, C.-J., LIN, J.-S., AGGARWAL, S. G. & CHEN, D.-R. 2004. Thermophoretic Deposition of Particles in Laminar and Turbulent Tube Flows. *Aerosol Science and Technology,* 38**,** 131-139.

VAN EYK, P. J., ASHMAN, P. J., NATHAN, G. J. 2016. Effect of high flux solar irradiation on the gasification of coal in a hybrid entrained-flow reactor. *Energy Fuels,* 20, 5138-5147.

WITKOWSKI, D. & ROTHAMER, D. A. 2019. Scattering referenced aerosol phosphor thermometry. *Measurement Science and Technology,* 30**,** 044003.

YU, M., SARNER, G., LUIJTEN, C. C. M., RICHTER, M., ALDÉN, M., BAERT, R. S. G. & DE GOEY, L. P. H. 2010. Survivability of thermographic phosphors (YAG:Dy) in a combustion environment. *Measurement Science and Technology,* 21.

Z'GRAGGEN, A., HAUETER, P., TROMMER, D., ROMERO, M., DE JESUS, J. C. & STEINFELD, A. 2006. Hydrogen production by steam-gasification of petroleum coke using concentrated solar power-II Reactor design, testing, and modeling. *International Journal of Hydrogen Energy,* 31**,** 797-811.

ZAMANSKY, R., COLETTI, F., MASSOT, M. & MANI, A. 2012. Buoyancy-driven turbulent flow in particleladen fluid subject to radiation. *Annual Research Briefs, Center for Turbulence Research, Stanford University***,** 217-228.

ZAMANSKY, R., COLETTI, F., MASSOT, M. & MANI, A. 2014. Radiation induces turbulence in particle-laden fluids. *Physics of Fluids,* 26**,** 071701.

ZHAO, B. & BAR-ZIV, E. 2002. Further development of temperature determination for a heated micron-sized particle from forced convection. *Journal of Aerosol Science,* 33**,** 165-180.

ZHAO, B., KATOSHEVSKL, D. & BAR-ZIV, E. 1999. Temperature determination of single micrometre-sized particles from forced/free convection and photophoresis. *Measurement Science & Technology,* 10**,** 1222-1232.

ZHENG, F. 2002. Thermophoresis of spherical and non-spherical particles: a review of theories and experiments. *Adv Colloid Interface Sci,* 97**,** 255-78.

ZISKIND, G., ZHAO, B., KATOSHEVSKI, D. & BAR-ZIV, E. 2001. Experimental study of the forces associated with mixed convection from a heated sphere at small Reynolds and Grashof numbers. Part I: cross-flow. *International Journal of Heat and Mass Transfer,* 44**,** 4381-4389.